Eindhoven University of Technology

MASTER

Creating a numerical model for burning metal fuels in industrial size burners

Krens, J.J.J.

Award date:
2019

TU/e EINDHOVEN UNIVERSITY OF TECHNOLOGY

Department of Mechanical Engineering
Power & Flow

Creating a numerical model for burning metal fuels in industrial size burners

Graduation Project

J.J.J. Krens
0677239

Supervisors:

Prof.dr. L.P.H. (Philip) de Goey

Dr.ir. J.A. (Jeroen) van Oijen

Dr. Ing. habil. M. (Martin) Schiemann

Final

Tilburg, August 2019

Abstract

The impact of greenhouse gas emissions on climate change is causing significant concern for both governments and the international community. This concern is driving the development for an economy that is less dependent on carbon-emitting activities. The utilization of energy resources is one of the primary sources of greenhouse gas emissions. Therefore, to achieve this "low-carbon society" our energy systems must make a transition from fossil-fuel sources to zero-carbon or renewable energy sources. Based upon the mass and volumetric energy densities, there are only a few chemical energy carriers that can compete with fossil-fuels. One of these options is metal or metal powders. This is a highly promising zero-carbon fuel option. Metal is such a promising option because it can react energetically with oxygen and form stable reaction products, which can be collected and recycled relatively easy.

The main focus of this graduation project is developing a model which can simulate the behaviour of metal fuels when combusted on an industrial scale. To do so, an existing particle model is analyzed, improved and tested. The model is validated, and the possibilities of scaling are investigated.

This is done by creating and comparing a computational version of a real-life setup, a Low-Swirl Burner at the Eindhoven University of Technology in which methane, iron or both can be combusted with air. Methane-air Low-Swirl Burners have already been investigated extensively, and from these cases, the first validation of the computational approach is performed. After this validation, several simulations are performed on the burner at the Eindhoven University of Technology: starting with pure methane-air. Different amounts of iron particles are added gradually until a complete shift is made towards an iron-air flame. The modelling is done in ANSYS Fluent, which lends itself perfectly for the simulation of methane combustion. For the combustion of iron, a user-defined function is introduced, which, by using custom laws for discrete phase modelling, defines the combustion of iron particles.

Following this approach, validation of the methane model is performed. First steps are taken to validate the iron model, and further steps to properly validate the model are proposed. Conclusions are drawn about the particle size, iron mass flow and oxygen concentrations. Geometric properties of the experimental setup are also investigated, and limits of this geometry are identified. The possibilities of scaling are touched upon, and a roadmap for the further development of a numerical simulation of metal fuels is proposed.

The current model is not perfect, but it shows great potential. Although there are still many challenges that lie ahead, this study can serve as a base for further development of a metal combustion model. The model needs to be improved, validated correctly and scaled up significantly .This model can be used to help *Metal Fuels* towards the next level, on its route to becoming a significant component in meeting the global energy demand, without producing greenhouse gasses.

Preface

I've read somewhere that the preface of a thesis or graduation report can be in- formal. I have no clue if this is correct, but I like the idea of one page to speak freely and informally about this project, so I choose to do so. If you are reading this, and don't agree with the first sentence, feel free to skip this chapter, I'm basically thanking people anyway. And do not worry, there are still 77 formal pages left which you can dive into! (appendices excluded, but a lot of figures, graphs and tables included).

I would like to start by thanking Philip de Goey, who stimulated me to finish my Master study. At the beginning of 2017, I was seriously considering quitting my Master Mechanical Engineering and focusing on my professional career, which was going well and was a lot easier for me than studying. My first meeting with Philip, on the 29th of May 2017, made me come back to the decision to quit and the decision was made to finish my Master study. After this meeting, a lot of meetings have followed First, during my internship, afterwards during my graduation project. Every meeting made me think, and kept me on my toes. Thanks Philip for your supervision in the last two years and for introducing me to the topic of metal fuels. May we meet again.

Martin Schiemann has provided me with his model, which is very important in this graduation report. Not only did you share your model with no strings attached, but you also answered a lot of questions and provided a lot of feedback on my work. Thank you for your time, especially for the moment that is still to come, when you attend my defense of this project during your holidays. The last member of my committee I want to thank is Jeroen van Oijen. I will not only remember you for your know- ledge in the field of numerical modelling but especially for the way you always wear a smile when discussing anything. For me, combined with your feedback, this made the whole project easier.

Of course, thanks to my parents, Rik and Kristl, although I doubt if they will ever read this line (or any other line of this report). Your support, both financially and emotionally, played a significant role by enabling me to do all the things I like to do. I also want to thank my aunt, Marijke, for helping me with the grammar and spelling of this document (Disclosure: if you are reading the version marked as concept, her notes haven't been processed yet). Big thanks to everyone at the University involved with metal fuels as well. The risk of forgetting someone is too big, so I'm not writing down names. If you helped me or gave me advice and you're reading this: thanks a lot!

Last but not least, I want to thank my ~~girlfriend~~ fiancée Rymme, for supporting me in every way possible. When this project is finished, I will try to be more present and available, although I cannot promise anything.

Let me finish by saying that I'm happy that my study time is almost over. Not only because I like doing other things more, or that more time will be available for challenges that await me, but also because in the end, I'm really happy to finish my Master study. The result of this graduation project is something to be proud of. In the future, I will still be following the developments of metal fuels closely, because there is a business model in there somewhere, that I'm confident about.

Jip

Contents

List of Figures

List of Tables

List of Symbols

The next list describes several symbols that will be later used within the body of the document

Mathematical Symbols

Δ change, in a certain quantity

M metal identifier

n Natural numbers

x numbering constant

y numbering constant

Other Symbols

(F/A) fuel-to-air ratio

$\dot{m}$ mass flow

ϵ_p particle emissivity

ϕ equivalence ratio

ρ Density

σ_p stoichiometric concentration

θ radiation temperature

A_p particle surface area

c_p heat capacity of the particle

c_p specific heat

d_{guide} burner guide diameter

d_p particle diameter

h convective heat transfer coefficient

H_{vap} heat of vaporization-dissociation

m_p mass of particle

M_{Fe} mass of iron

M_{N_2} mass of nitrogen

M_{O_2} mass of oxygen

P power

Q heat content

Q_R heat of reaction

t time

$T_p(t)$ particle temperature

T_b boiling temperature

T_{vap} vaporization temperature

T_{vol} volatilization temperature

u energy density

U_∞ reference flow velocity

U_{in} radius centre plate

U_o width vanes

V Constant Volume

R_h length from center until expansion;

R length from vane until expansion;

Physics Constants

σ Stefan-Boltzmann constant

g Gravitational Constant

Chapter 1

Introduction

The effects of greenhouse gas emissions on climate change is causing major concern for both governments and the international community. This concern is driving development for an economy that is less dependent on carbon emitting activities. The utilization of energy resources is one of the main sources of greenhouse gas emissions. Therefore, to achieve this "low-carbon society" our energy systems must transition from fossil-fuel sources to zero-carbon and/or renewable energy sources [29].

Setting aside the concern for the climate, a transition is also needed to cope with the finite fossil-fuels. This transition is needed to offset the constraints on fossil-fuels that are associated with future economic growth [26]. A widely discussed alternative is biofuels [6]. However, estimates indicate that bioenergy alone cannot completely facilitate the transition from fossil-fuels due to the low effective energies and power densities that are associated with photosynthesis [17].

Another challenge when replacing fossil-fuels is the storage capabilities of the fuel. Even when energy is produced from clean energy sources, they cannot be stored or transported as easily as fossil-fuels. For that reason a clean and sustainable energy carrier is needed that can be both stored and transported easily. At the moment batteries and hydrogen are the most frequently proposed energy carriers for a low carbon society [29, 17, 18].

Burning fossil-fuels in high-power-density internal combustion engines is an essential component of today's society. So it's essential that any alternative can compete with fossil-fuels regarding energy and power densities. Most suggested alternatives however, are far inferior to fossil-fuel powered internal combustion engines. Society needs energy carrier alternatives that will be able to replace or supplement the dominant fossil-fuels [31].

1.1 Alternatives for Fossil-Fuels

Based upon the mass and volumetric energy densities, there are only a few chemical energy carriers that can compete with fossil-fuels. One of these options is metal or metal powders. This is a highly promising zero-carbon fuel option. Metal is such a promising option because it can react energetically with oxygen and form stable reaction products, which can be collected and recycled relatively easy [33, 4].

Metals have a high energy density, which makes them a good, attractive option as a fuel. Many metal fuels even have higher volumtric energy densities than fossil fuels when burned with air. This can be seen in Figure 1.1 Both aluminum and magnesium are studied extensively and have been considered as clean energy carriers [33, 36, 37]. Iron has been considered as both an inexpensive and clean energy carrier [4, 28].

Silicon, magnesium, aluminium and iron are all metals with high energy density and specific energy and are abundantly present. These properties make metals good candidates to be used as a fuel (metal fuel). Metal fuels have energy densities that are superior to biomass, coal and compressed gas, which are all shipped globally for the energy trade [10].
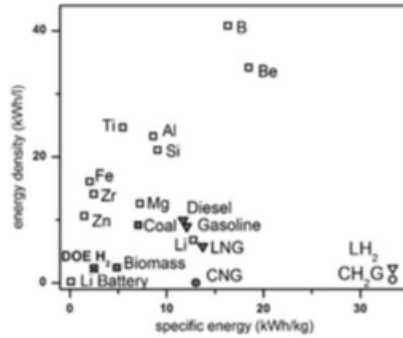
Figure 1.1: The volumetric and gravimetric energy density for various metal fuels compared to batteries, bio-derived fuels and fossil fuels. From: [6], page 370

1.2 Metal Fuels

The ability to effectively and efficiently store energy is what makes metal fuels so interesting for the energy sector. This sector is very dependent on supply and demand, so storing energy could be a real game changer. There is a big difference in demand between for example winter and summer. In the winter period the energy demand is usually much higher than in the summer period. During a period of high demand, renewable energy sources provide far too little energy to satisfy this demand. The other way around, in periods of low demand renewable sources can provide a surplus of energy, but this cannot be stored [3].

The difference between this high and low demand could be (partly) compensated by storing excess energy in periods of low demand and access this stored energy in periods of high demand. Metal fuels would be ideal for this type of storage. Next to the advantage of being able to use more renewable energy, energy is generally much cheaper in periods of low demand. [1] This could be a major advantage when looking into the price of metal fuels as a fuel for a power plant.

This difference between supply and demand is visualized in figure 1.2, as a function of the solar power in Morocco versus the power demand in the Netherlands. This is just an example to clarify the possible difference in demand. Solar power is a good example to make this comparison, because this largely depends on seasons.
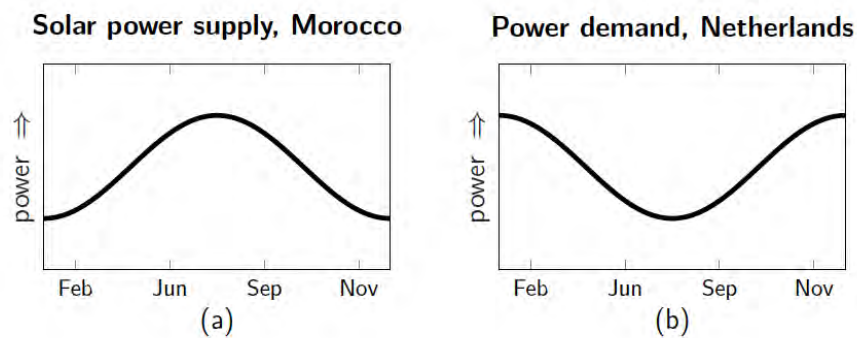
Figure 1.2: Solar power intensity trend as function of time in Morocco (a) and electricity demand trend in the Netherlands (b) From: [8], page 17

Next to the advantage of being able to harvest energy on a yearly scale, there is also the ability to counter peak demand on the energy market. This demand can vary not only over days, but is

even monitored over 15 minute periods [2]. During this peak demand, there are periods in which renewable energy cannot immediately supply the demand, for example, on a very hot, windless day, where everyone turns on their air-conditioners. During this period the need arrises to directly increase the energy production. It is impossible to create more solar or wind power on demand, but it is possible to burn more metal fuels. So an other advantage of metal fuels is that it can be used to ensure power grid stability.

1.3 Metal Fuels in a Conventional Power Plant

Prior to this graduation project, an internship has been done studying the techno-economic challenges on the supply side of metal fuels at a power plant [24]. The goal of the internship was to make a reasonable assumption on whether it is possible to (partly) integrate metal fuels in an existing conventional coal powered power plant.

The investigated metal fuel cycle is a cycle with zero associated carbon dioxide emissions. The cycle consists of 4 major parts: generation of renewable energy, regeneration, transport and combustion. A schematic overview can be seen in figure 1.3. The version of the cycle in this report is one where the completed cycle is located in a small geographical area, greatly reducing transport costs.
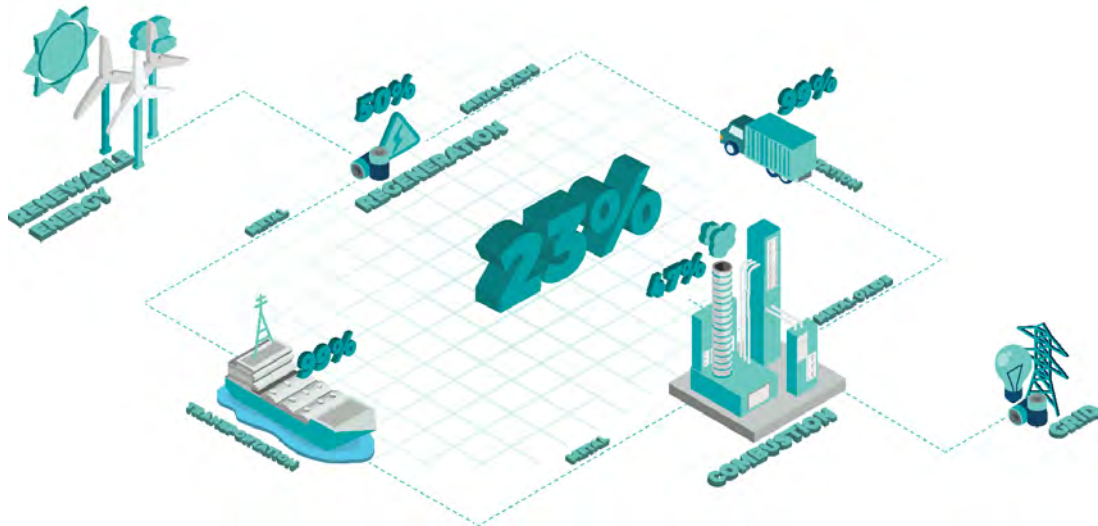
Figure 1.3: Schematic representation of the metal fuel cycle for a conventional power plant with the efficiency for every part of the process. The 23 is the amount of electricity that is supplied to the grid compared to the amount generated by renewable energy. From: [24]

When looking at the current available technologies, it seems realistic that metal fuels can be burned in convention coal powered power plants. When looking at available flame speeds and burning velocity combined with the energy densities of metal fuels they indicate that metal fuels can be burned in power devices at nearly equivalent power densities to modern systems fuelled by fossil fuels.

1.4 Lighthouse project

At the moment of writing, there is ongoing project investigating the possibility of burning metal fuels in industrial size burners. After a proof-of-principle [23] by TEAM SOLID, a student team of the Eindhoven University of Technology, the next step is to develop a 100 kW system fuelled

by metal fuels. When successful, the goal is to scale the system to a 1 MW system. In this range the system will enter the region where it is scalable to the size of an actual power plant, although this is a very big step and still a long way away.

Chapter 2

Preliminaries

2.1 Description

The main focus of this graduation project will be creating a model that can simulate the behaviour of metal fuels when they are burned in a conventional coal powered power plant. Because all current existing models that can model the combustion of metal particles are very rudimental, combined with the time scope of this study, the full size of a power plant will in all probability not be reached. Nevertheless, steps are taken, or proposed, to achieve such a model.

The model that will be created will be a (1,2 or 3D) mathematical model. This model will be optimised for mass and heat transfer for burning metal fuel and might give directions on how to operate metal fuels. The fuel can consist of different compositions: the burned metal can differ (iron, aluminium, silicon etc.) and it can be pure (100% metal fuel) or a mixture (metal fuel-coal, metal fuel-bio mass, etc.). The model will be solved numerically and will be validated by comparing the results with known and/or experimental data.

2.2 Main Question

Creating a numerical model for burning metal fuels in industrial size burners

2.3 Sub Questions

- Main model architecture

  - What are the existing models for burning metal fuels? (1D, CFD, Spence?)
  - Can these existing models be used/altered or is it better to build a model from scratch?
  - What are the boundary conditions for the model?

- Other questions

  - What are the similarities and differences between a 1.1 *GW* power plant and a 0.1-1 *MW* burner?

Chapter 3

Modelling Metal Combustion

Multiple options have been considered for modelling the combustion of metals. Possibilities are described first in this chapter, after which the decision on the final model is made and substantiated. This model is then described in detail.

3.1 Different Metal Combustion Models

3.1.1 CHEM1D

One of the considered models is the model developed by Thijs Hazenberg (TU/e) during his master Thesis [15]. This model uses a Eulerian description to solve a continuous gas phase and a Lagrangian description to solve the dispersed phase. This numerical method is explained by using the CHEM1D software [34]. While promising, this model is still far from a complete model. The author himself concluded that the model is the first step to future research. Also, because the model is currently only calculating one dimensional flows, it is not yet applicable to industrial burners.

3.1.2 Furnace Model

Another option is using a furnace style model. These models are used in commercial software like Spence. A furnace style model is a layered model with a segmental approach. This method assumes all layers are perfectly stirred and is one-dimensional: this means that the flow is moving in one direction and that only transport is possible from layer n to layer $n+1$. A description of the model can be seen in figure 3.1.
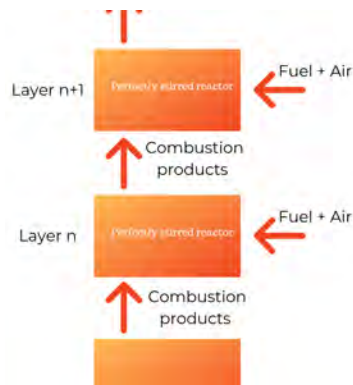
Figure 3.1: Schematic description of furnace model with segmental approach.

Because of the simplicity, these models are beneficial for large scale reactors, for example, a *GW* coal-fired power station. Currently, there are furnace models for fossil fuels and alternative fuels like biomass, but no models for the combustion of metals are available. Because not all combustion parameters for metal combustion are known, it is rather challenging to create a furnace model. Therefore a correct particle model should be developed first, which then could be used to develop such a furnace model to model larger setups.

3.2 Detailed Euler-Lagrangian Approach

The last considered alternative is using a CFD solver, for example the commercial software package Ansys Fluent®. Fluent software contains broad physical modelling capabilities needed to model flow, turbulence, heat transfer and reactions for industrial applications. In the standard features of the code, there is no model for the combustion of metal particles, but Fluent can use user-defined functions, or UDFs, which are functions that can be dynamically loaded within the Ansys Fluent solver. With these user-defined functions boundary conditions, material properties and source terms can be defined. It is also possible to specify custom model parameters like a Discrete Phase Model.

Such an User-Defined Function for the combustion of iron particles has been created by Schiemann et al. of the Ruhr-University Bochum [27]. This UDF models the combustion of a single iron particle based on diffusion-limited conversion. Although rudimental to date, this model is considered to be an advanced metal combustion model. Combined with the authors' experience with Ansys Fluent the decision is made to use the model from Schiemann et al. as a starting point. The model will be applied to low swirl burners, and improved and validated where possible and/or necessary.

3.2.1 User-Defined Function

The decision is made to create a numerical simulation by using Ansys Fluent, which means a User-Defined function will be needed because there is presently no model in Fluent that correctly models the region of interest of this study, metal combustion. But what exactly is such a UDF? Shortly summarized a UDF is:

- Adds functionality or modelling capabilities which are absent;

- A function that can be dynamically loaded with the Ansys Fluent solver;

- Is written in the C programming language.

In this case the UDF is used to customize material properties, reaction rates and source terms. For iron particles these data are not available in Fluent, so it has to be defined. After the definition of these custom parameters they are included in an enhanced version of the existing discrete phase model.

In Fluent the UDFs can either be interpreted or compiled [16]. A compiled UDF is built the same way the executables of Fluent itself are built. Interpreted UDFs are interpreted from source files in a single-step process. This process occurs at runtime. When deciding which type to use, the advice is to use interpreted UDFs for small, straightforward functions and compiled UDFs for complex, CPU demanding functions (for example a UDF that is called upon every cell every iteration). In this case, the decision is made to use a compiled UDF.

3.2.2 Mesh Terminology

The UDF will access data from the Fluent solver; therefore, one should understand the storage of these data into the mesh before writing and using a UDF. Fluent uses a pretty straightforward way

of defining a mesh; the mesh is broken up into control volumes (CV). These CV are characterized by a set of nodes, the center of the CV, and the neighboring faces. A simple version of such a mesh can be seen in figure 3.2
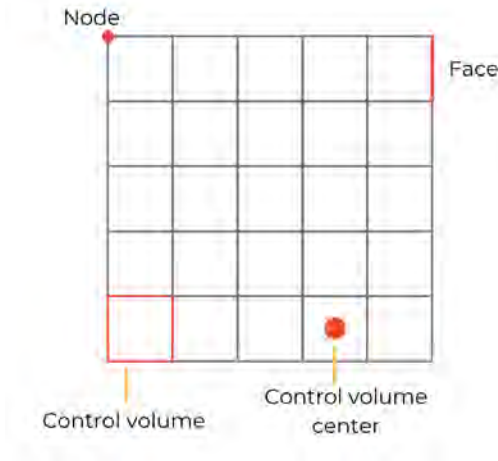
Figure 3.2: Simple two-dimensional mesh

Fluent uses threads to store information about a boundary or control volume zone. CV threads are a grouping of control volumes, and face threads are similarly groupings of faces. These thread data structures are used to access information about the boundary or CV zones. Typically, control volumes and faces are grouped into a zone that is a physical representation of the model. This can represent for example an inlet, outlet or wall. A domain is used to store the data of a collection of nodes, face threads and control volume threads in a mesh.

3.2.3 UDF solution process

User-Defined Functions are called upon in the solution process at predetermined times. The UDF used is solved by using the Pressure-Based Coupled solver, which is advised when simulating high-density cases or cases with complicated physical conditions. The solution process for this solver starts by initializing the solution outside the solution iteration loop. This initialization sequence begins by initializing the equations by using user entered or default values. After this, the initialization in the UDFs is called upon. This initialization defined in the UDF overwrites al previous set initialization values. In the UDF used for metal combustion, the following values are initialized:

- Particle temperature, T_p,

- Particle mass, m_p,

- Particle diameter, d_p,

The solution iteration loop first checks the UDF for any adjustments to the standard variable that are not passed as arguments (for example flow variables as velocities and pressure). After this, the coupled governing equations for continuity and momentum are solved. The energy, species and other transport equations are then subsequently solved. The remainder of the solution consists of updating the properties and checking for convergence. A schematic overview of the solution procedure can be seen in figure 3.3.
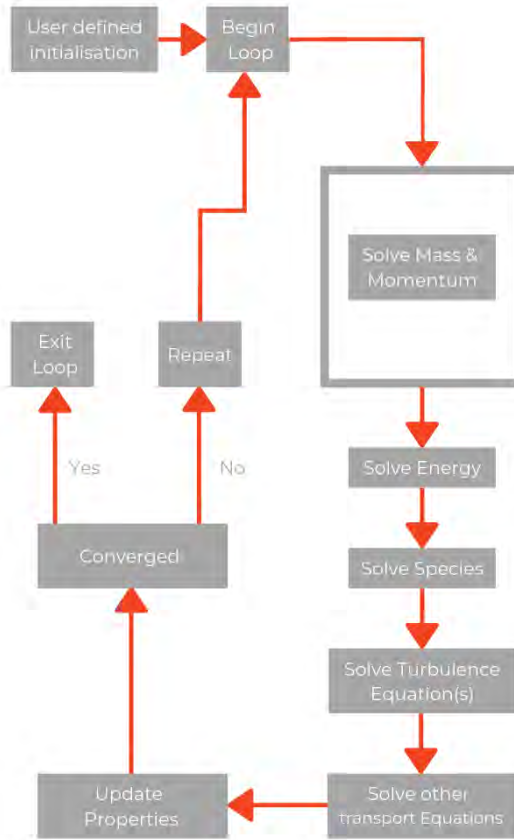
Figure 3.3: Schematic overview of the solution procedure a pressure-based coupled solver.

3.3 Thermodynamics of Metal Combustion

The combustion of metal particles with oxygen is unique because the adiabatic flame temperature is a specific known value: the vaporization-dissociation, or volatilization temperature, of the metal oxide [12]. This is due to the physical fact that the heat of vaporization-dissociation to form a metal-oxide is greater than the available heat for raising the condensed state of the metal-oxide above its boiling point:

$$\Delta H_{vap-diss} > Q_R - \left(H^{\circ}_{T,vol} - H^{\circ}_{298} \right) = \Delta H_{avail} \tag{3.1}$$

where:

- $\Delta H_{vap-diss}$ is the heat of vaporization-dissociation of the metal oxide [11],

- Q_R is the heat of reaction of the metal at the reference

     temperature $298[K]$,

- $\left(H^{\circ}_{T,vol} - H^{\circ}_{298} \right)$ is the enthalpy required to raise the product oxide to its

     volatilization temperature.

To burn a condensed-phase fuel in the vapor phase, it is necessary that the flame temperature is higher than the fuel saturation temperature. As a result, the fuel will vaporize and will become diffuse. Metals, contrary to hydrocarbon fuels, have very high saturation temperatures. This means that for a metal to be able to burn as a vapor, the oxide volatilization temperature must exceed the metal boiling point. This particular effect is known as Glassman's criterion. By comparing the values for T_{vol} and T_b from table 3.1, it can be seen that iron will burn in the vapor phase in oxygen:

Table 3.1: Various properties of iron oxide

Metallic Compound	T_{vol} [K]	ΔH_{vol} [kJ/mol]	$\left(H^\circ_{T,vol} - H^\circ_{298}\right) + \Delta H_{vol}$ [kJ/mol]	$\Delta H^\circ_{f,298}$ [kJ/mol]	T_b [K]
FeO	3400	610	830	-272	3133

Values from the JANAF Tables [30].

By using computational fluid dynamics and the parameters found in the thermodynamic tables [30], it is possible to calculate metal-oxygen flame temperatures. For metal oxides it is proven to be difficult to define an equilibrium thermodynamic boiling point [**?**]. Instead, the term vaporization-decomposition temperature is more suitable to describe the "boiling" point of a metallic oxide. This temperature describes the point at which the volatilization of metallic oxides occurs, and can be defined as: "volatilization temperature, exhibiting characteristics of a transition temperature or boiling point"

The adiabatic combustion temperature for metal-oxygen combustion is mainly dependent on the metal oxide volatilization characteristics, and the combustion temperature is limited to the boiling point of the oxide [35]. The ability to calculate combustion temperatures has introduced the "limiting temperature" concept [12]. This concept states that the enthalpy of combustion of reactants at stoichiometric ambient conditions $(298K)$ alone is not sufficient to volatilize all the condensed-phase metallic oxides. In other words, the metallic oxide undergoes a phase change.

3.3.1 Metal-Oxide reactions

The general, stoichiometric, metal-oxygen reaction is:

$$xM\left(s\right) + yO_2\left(g\right) \rightarrow M_xO_{2y}\left(s\right) \tag{3.2}$$
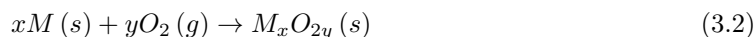
Where x represents the atoms of the solid metal M which reacts with y moles of gas-phase oxygen to produce one mole of a solid metal-oxide, M_xO_{2y}. For the oxidation of iron this reaction becomes:

$$4Fe\left(s\right) + 3O_2\left(g\right) \rightarrow 2Fe_2O_3\left(s\right) + 413 \text{ [kJ/Mol]} \tag{3.3}$$
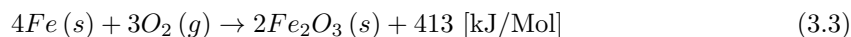
During the combustion of iron, however, there are other iron oxide compositions present. These compositions can be found in the equilibrium position of a stoichiometric iron-air mixture and depend on the temperature [27]. To take into account these compositions, the following reactions are considered as well:

$$2Fe\left(s\right) + O_2\left(g\right) \rightarrow 2FeO\left(s\right) \tag{3.4}$$

$$3Fe\left(s\right) + 2O_2\left(g\right) \rightarrow Fe_3O_4\left(s\right) \tag{3.5}$$
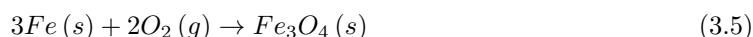
3.3.2   Iron particle model

As described in section 5.3, the combustion of metal can be described by using a temperature limited approach: the combustion behavior depends on the different temperatures of the metal and metal oxides. At these different temperatures, the metal and metal-oxides undergo different phase changes. If the temperature exceeds the melting point, the metal starts vaporizing. The rate of this vaporization depends on the specific vapor pressure. When this vapor pressure is low at the adiabatic flame temperature, the combustion will occur at the surface of the droplet. If this is the case, there are two possibilities for the combustion mode. The first occurs when the boiling point of the reaction product is below the adiabatic flame temperature; then it will evaporate and form aerosols. The second happens when the combustion takes place below the oxides boiling point. In this case, little to no aerosols are formed. The assumption is made that for iron particles at the micrometer scale the second combustion mode occurs.

The transition into a model which can be used in the Euler-Lagrangian framework is made by using the thermo-physical restrictions defined above, the material properties and fundamental combustion physics. The result is a temperature-limited model which takes the characteristic temperatures for decomposition and phase changes into account. In this model, several steps are taken to describe the heat release and mass conversion in time.

3.4   Computational Model

By using the assumptions in this chapter, a model is made that follows a set of different steps to model the combustion of iron. In this section these different steps are described.

3.4.1   Heating of particles

Iron oxidizes at any temperature, the question is how fast the reaction will go. The temperature dependency of the chemical reaction rate is generally modelled by using the Arrhenius equation. Because not all required parameters are known and the real, correct mechanisms are still a point of discussion, a different, simplified approach is chosen: using the ignition temperature. This step is based upon the inert heating of cold particles until the point at which these particles reach a pre-defined ignition temperature. To determine this pre-defined ignition point, thermogravimetric analysis (TGA) mass gain experiments are executed [27]. During these experiments, the mass gain of iron powder in air, which is exposed to non-isothermal TGA conditions, is measured in two different TGA apparatus. The temperature condition in these TGA's was $dT/dt = 5K/min$.

Two iron powders are used, with a different mass, 50 and 130 mg, respectively. The results of these TGA-experiments can be seen in figure 3.4. From this figure, it can be seen that there is a steep mass gain of the iron in the temperature range between 650 and 800 K. Therefore, the ignition temperature point is chosen to be defined at 700 K.
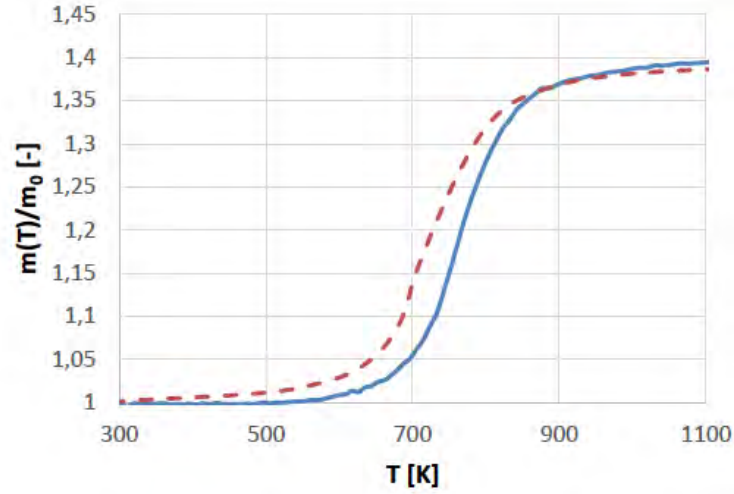
Figure 3.4: TGA mass gain curves for two iron powders: 50 mg (red-dashed) & 130 mg (blue). From: [27].

3.4.2 Thermal runaway

When the temperature reaches the ignition temperature point, the next step in the model starts. This step begins with thermal runaway; the particle temperature increases until the particle reaches the boundary diffusion limit [25]. Because of the absence of detailed chemical kinetics for the oxidation of iron in this temperature region, some assumptions have to be made during this step. The chemical reaction considered in this step is the formation of magnetite:

$$3Fe(s) + 2O_2(g) \rightarrow Fe_3O_4(s) + 374 \text{ [kJ/mol]} \tag{3.6}$$
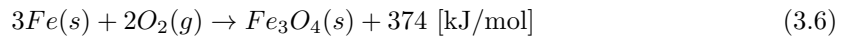
The formation of FeO is neglected during this step because it is rare to be present in a solid iron oxide sample. When iron oxidizes and the molar ratios of iron and oxygen are equal ($Fe/O = 1$), the mixture will probably be one consisting of Fe and Fe_3O_4[32]. Fe_3O_4 sticks to the particle during the oxidation, while O_2 is consumed simultaneously. The rate at which this oxygen is consumed, the transfer rate, is calculated from the mass transfer limit in the particle boundary layer. This boundary layer consists of a gas film around the particle.

The particle temperature increases while heat exchange is calculated considering convection and radiation. The oxidation rate is calculated by the following formula:

$$\dot{n}_{O_2} = 2\pi d_p \frac{D_{O_2}}{RT_\infty} p_{O_2,\infty} \tag{3.7}$$

where:

- $\dot{n}_{O_2}$ is the oxygen consumption rate,

- d_p is the particle diameter,

- T_∞ is the temperature in the boundary layer ,

- p_{O_2}, ∞ is the partial pressure of oxygen in the free gas stream.

The film temperature is an approximation of the temperature of the convection boundary layer, and is calculated by using the particle temperature (T_p) and the free stream or gas temperature (T_g):

$$T_{film} = \frac{T_p + T_g}{2} \tag{3.8}$$

Based on the heat release of the particle, the particle temperature can be calculated by using the following formula:

$$\alpha A_p \left(T_\infty - T_p\right) + \varepsilon_p A_p \sigma \left(T_w^4 - T_p^4\right) + \frac{dm_p}{dt}\Delta h_r^i = m_p c_p \frac{dT_p}{dt} \tag{3.9}$$

The emissivity of the iron oxides is taken from experiments [13]. During this experiment, thermal radiation measurements were carried out on magnetite and hematite in the temperature range between 773 and 1273 K. The results can be seen in figure 3.5. Ideally, the value would adapt depending on the temperature and particle composition, however, this is not included in the model yet. Currently a stationary value for the emissivity is chosen: $\varepsilon_p = 0.75$.
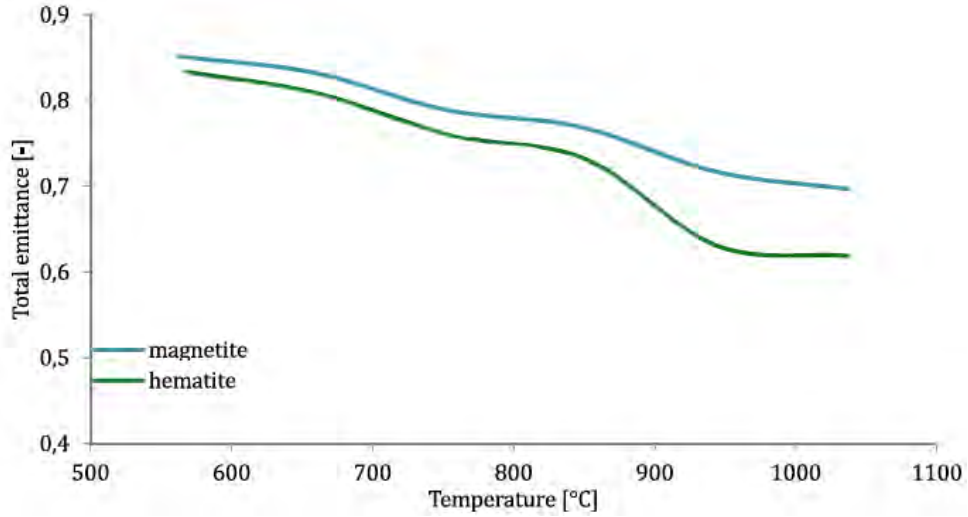
Figure 3.5: Comparison between the total emittance of hematite (green) and magnetite (blue) From: [13]

The heat of reaction for the phase changes is taken from the NIST-JANAF Thermochemical Tables [30], at the melting point at 1 bar:

$$[\Delta_{fus}H^\circ]_{Fe} = 13.807 \left[\frac{kJ}{mol}\right]$$

$$[\Delta_{fus}H^\circ]_{Fe_3O_4} = 138.16 \left[\frac{kJ}{mol}\right]$$

3.4.3 Melting of Fe

When the particle temperature reaches the melting temperature of Fe, 1809 K[30], the Fe that is still present in the particle starts melting. During this melting phase, the particle temperature remains constant. Besides melting, the reaction from Fe to Fe_3O_4 continues during this step.

3.4.4 Ongoing reaction

When Fe is completely liquified, the reaction keeps on going which increases the particle temperature until the melting temperature of Fe_3O_4 is reached.

3.4.5 Melting Fe_3O_4

The melting point of Fe_3O_4 is defined at a particle temperature of 1860 K[30]. The same happens as in the melting of Fe step: particle temperature remains constant while the Fe_3O_4 melts. The reaction is still ongoing.

3.4.6 Decomposition

When the complete particle is liquified, the particle temperature starts to rise again due to the ongoing reaction. The temperature keeps increasing until the decomposition temperature of Fe_3O_4, 2358 K[30], is reached. This temperature point is set as the upper limit in the model. The reasoning behind this clear upper limit is that the only higher oxidation state, namely Fe_2O_3, does not exist at these temperatures. At this decomposition temperature, the reaction rate is controlled by the temperature boundary (which is determined by convective and radiative heat loss) or by the diffusion limit of oxygen.

The diffusion limit reinforces the decision of the upper limit, because in high-density particle mixtures, like the simulated burner, the combustion temperature will be limited by this diffusion limit. It is therefore unlikely that the particle temperature can exceed the decomposition temperature much.

3.4.7 Fe_3O_4

When all Fe is converted into Fe_3O_4, the reaction will obviously stop. At this point, the particle starts to cool down, without any chemical reaction. The complete particle consists of pure, liquid Fe_3O_4.

3.4.8 Solidification of Fe_3O_4

The particle temperature of the liquid Fe_3O_4 keeps on dropping until the melting temperature of Fe_3O_4 is reached again. At this point, the solidification of Fe_3O_4 starts and continues until the entire particle consist of solid Fe_3O_4. During the solidification, heat is released by convection and radiation. In the model, the convection is coupled only to the gas phase. The radiation is coupled with the gas phase, walls and the other particles.

3.4.9 Cooling

After the complete solidification of Fe_3O_4, the particle keeps cooling down until it reaches the decomposition temperature of Fe_2O_3. This temperature is defined at 1735 K[30]. When this temperature is reached, the next step begins.

3.4.10 Second reaction

After the decomposition temperature is reached, a new reaction starts; the transition from magnetite into hematite:

$$4Fe_3O_4\,(s) + O_2\,(g) \rightarrow 6Fe_2O_3\,(s) \tag{3.10}$$
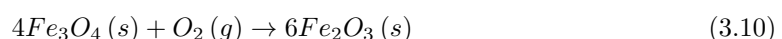
The reaction rate is limited by either the decomposition temperature, or the diffusion limit of oxygen. In the case of a temperature limit, the particle temperature remains constant during the reaction. Otherwise, in case of the diffusion limit the particle temperature drops.

3.4.11   Converting and cooling

After all the Fe_3O_4 is converted into Fe_2O_3 the reaction stops. The only thing that happens after this point is the cooling of the solid hematite particle towards the gas temperature.

3.5   Steps in the Model

The complete model has been described, and can be seen as a model with eleven steps. To create a short overview, al the steps are shortly described in table 3.2:

Table 3.2: Overview of all the steps in the computational model

Step	Name	Description
1	**Inert heating**	Particle heats up
2	**Thermal Runaway**	Ignition temperature of 700 K is reached, ignition starts
3	**Melting of Fe**	Fe starts melting at 1809 K
4	**Ongoing reaction**	Fe is completely liquid, keeps reacting into Fe_3O_4
5	**Melting of Fe_3O_4**	Fe_3O_4 starts melting at 1860 K
6	**Decomposition**	Particle is completely liquid and reaches the decomposition temperature of 2358 K
7	**End of reaction 1**	The first reaction stops when all Fe is consumed.
8	**Solidification of Fe_3O_4**	Temperature drops until the melting temperature of Fe_3O_4 is reached again (1860 K) and the particle solidifies
9	**Cooling**	Cooling stops when the decomposition temperature of Fe_2O_3 is reached.
10	**Reaction 2**	The second reaction starts. Fe_3O_4 converts to Fe_2O_3
11	**Conversion & cooling**	The complete particle is Fe_2O_3, the reaction stops. and the particle cools down to gas temperature

3.6   Drop Tube Simulation

To validate the computational model, simulations on a single particle in a drop tube furnace are performed, which is a standard experiment for single particles. The advantage of such a simulation is that due to the geometry of a drop tube, a laminar, one dimensional flow field exists. In this case a two-dimensional drop tube is simulated, because the first simulations of the low-swirl burner will also be executed in 2D. The dimensions of the drop tube in the simulation are rectangular, with a height of 2000 mm and a width of 25 mm. The particle diameter of the iron particle is 50

μm and the gas temperature within the drop tube is set at 933 K.

This results in the following particle temperature profile, where all the steps in model (defined in table 3.2) can be seen. To clarify, a second figure is created, figure 3.7, where all the specific steps from table 3.2 are marked.
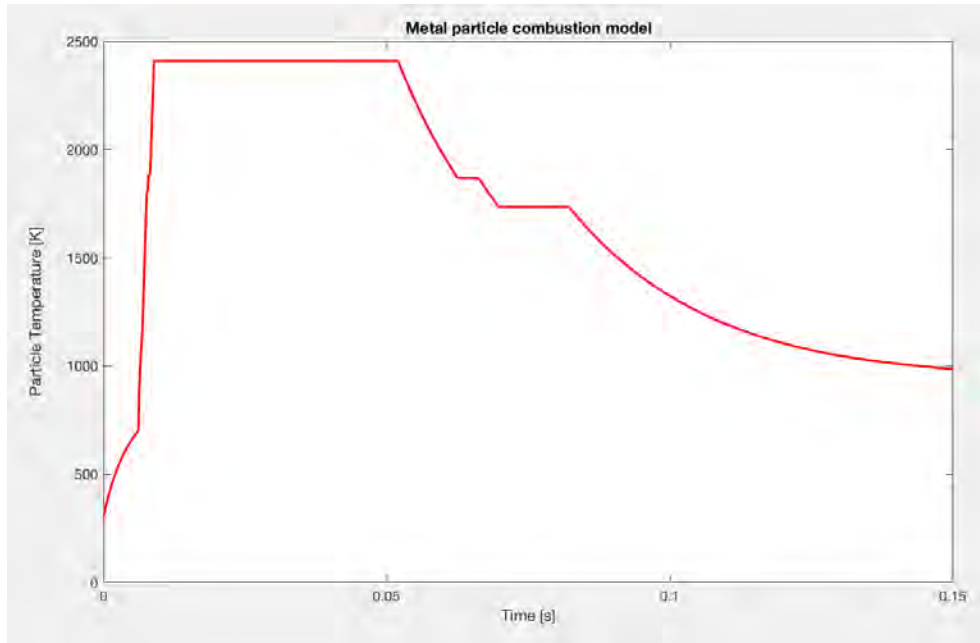
Figure 3.6: Particle temperature of an iron particle (50 μm), simulated in a two dimensional drop tube.
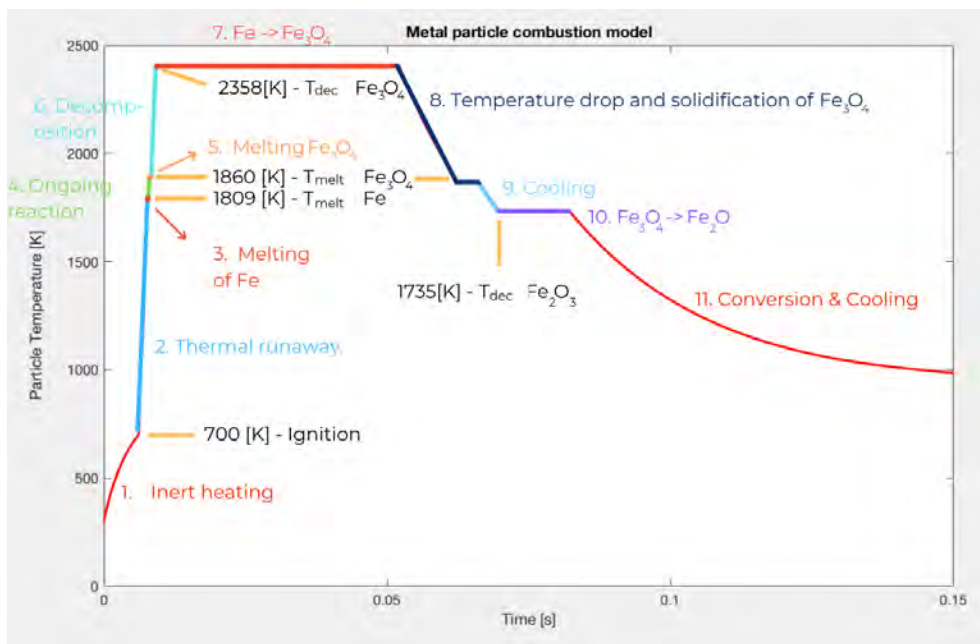
Figure 3.7: Figure 3.6, with all the steps from table 3.2 marked.

The most important variables that are defined in the computational model can be found in table 3.3. All other important variables that are used are imported from Ansys Fluent.

Table 3.3: Most important variables defined in the computational model

Material	Molar Mass [g/mol]	Density [kg/m³]	Melting Temperature [K]	Decomposition Temperature [K]	Forming Enthalpy @298.15[K] [kJ/mol]	Reaction Heat [kJ/mol]
Fe_3O_4	231.53	5000	1870	2358	-1120.894	138.16
Fe_2O_3	159.69	5240	-	1735	-825.503	-
Fe	55.845	7874	1809	-	0	13.807
O_2	16.0	-	-	-	0	-

Other Variables	Value
Ignition Temperature	700 $[K]$
Emittance	0.75$[-]$
Gas Constant	8.31451 $[J/mol*K]$

Chapter 4

Validation of Low Swirl Burner in Fluent

Before the computational model is used in a more complex geometry and environment like a Low Swirl Burner (LSB), a simpler case available from literature is modeled in Fluent. This results in the simulation which is based upon the thesis (Ph.D.) of David Beerer of University of California, Irvine [5].

4.1 LSB Beerer

4.1.1 Experimental setup

The experiments on this LSB are performed on a Low Swirl Burner in a pressure vessel which is made optically accessible. The setup is located at the University California Irvine Combustion Laboratory (UCICL). The geometry of the LSB consists of a 30 cm long premixing chamber with a diameter of 31.75 mm and the main combustion chamber with a diameter of 150 mm and a length of 230 mm. The geometry of the experimental setup can be seen in figure 4.1 and 4.2.

Figure 4.1: Cross section of pressure vessel and burner arrangement from thesis Beerer. From: [5].

Figure 4.2: Low-swirl methane flame in the premixed and main combustion chamber. From: [5].

The principle of a LSB is using a Low-Swirl Injector (LSI), which produces a divergent turbulent flow field, to create a stabilized detached or lifted flame that is propagating freely along the flow field. In this case, the LSI is statically placed inside the premixing chamber. The LSI is a circular device, consisting of two channels. The inner channel is a perforated plate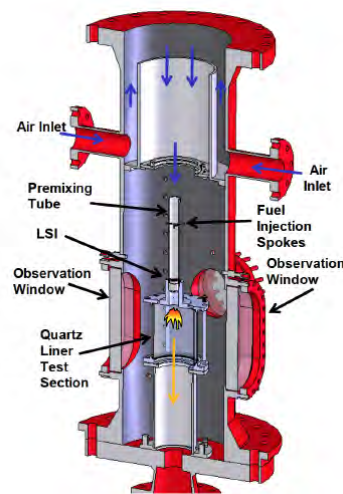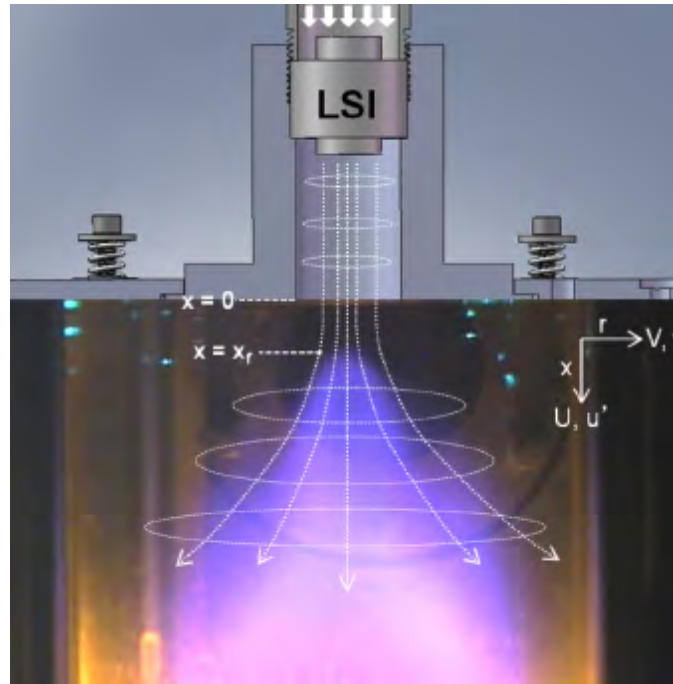; the outer channel consists of multiple swirl vanes. The reactants pass the LSI as a premixed flow. The inner channel creates a non-swirling inner region. It does, however, creates turbulence, the level of this turbulence is determined by the hole pattern and hole size of the plate. The outer channel creates a swirling outer region. This swirling motion of the outer region causes the flow to expand radially outward. This expansion also induces radial divergence on the inner channel.

This divergence causes the mean axial velocity along the centerline of the flow field to decrease. Decreasing this velocity is a critical ingredient in stabilizing the flame; the flame will propagate along the centerline with characteristic speed $S_{T,LD}$, until it reaches the point on the centerline where the local velocity U is equal in size, but opposite in direction. This causes the velocities to balance and creates a stationary, lifted flame. Contrary to High Swirl Burners, the LSI does not create a swirl significant enough to create vortex breakdown or a recirculation zone within the vicinity of the flame [22]. Therefore, a flow created by a LSI results in simpler aerodynamics. Because of the simplicity of the flow field, a LSI created flow lends itself perfectly for computational simulations. An extra advantage of using a LSI is the lifted flame, which avoids complex interactions with the walls and heating of the injection nozzle.

The LSI used during the experiments of Beerer is a scaled version of a LSI created by Robert Cheng [22]. This is convenient, because the LSI used in the LSB at the Eindhoven University of Technology is based upon the same LSI. The LSI used in Beerer's study can be seen in figure 4.3. The outer channel, has a radius (R_o) of 19 mm, the inner channel has a radius (R_i) of 13 mm. In the outer channel 16 aerofoil shaped swirl vanes are positioned. These vanes have a discharge angle of 37° relative to the flow direction. The perforated plate in the inner channel has 25 holes with a diameter of 2.6 mm, arranged in a concentric pattern.

Figure 4.3: Low Swirl Injector, back view (left) and front view (right). From: [5]

4.1.2 Experimental parameters

The most important parameters from the experiment can be found in table 4.1:

Table 4.1: Conditions of the experiment. From: [5]

Fuel	Pressure	Mass Flow	Bulk Velocity	Temperature reactants	ϕ	Adiabatic Flame	CH_4	Heat Release
	[atm]	[g/s]	[m/s]	[K]	[-]	[K]	[%]	[kW]
CH_4	4.1	185.6	50.5	418	0.715	1943	100	387

4.1.3 Translation to Fluent

Because the first simulations of the LSB will be done in a two-dimensional environment, some assumptions need to be made to convert the design of the LSI in a correct two-dimensional representation; it is not possible to correctly model a three-dimensional vane in a two-dimensional environment. The first decision that is made is to model the LSI by using two mass flow inlets; one representing the inner channel, the other one representing the outer channel. Here the first obstacle rises: determining the mass flow for each separate inlet. To do this, Bernoulli's energy conservation equation is used:

$$\dot{m} = A_{eff}\sqrt{2\rho\Delta P_{LSI}} \tag{4.1}$$

where:

- ρ is the density of air,

- ΔP_{LSI} is the pressure loss over the LSI,

- A_{eff} is the effective area.

$\Delta P_{LSI} = 13.1kPa$ [5] and the effective area, A_{eff} can be determined by using:

$$A_{eff} = C_{loss}A_{geo} \tag{4.2}$$

where:

- C_{loss} is the loss coefficient,

- A_{geo} is the geometric area.

Because the Bernoulli approach is an estimate to determine initial simulation values, the decision it made to choose unity for the loss coefficient, which results in a updated version of equation 4.1:

$$\dot{m} = A_{geo}\sqrt{2\rho\Delta P_{LSI}} \tag{4.3}$$

For the inner channel, the geometric area is defined by the number of holes (N_{holes}), multiplied by the area of a single hole (A_{hole}):

$$A_{inner} = N_{holes}A_{hole} \tag{4.4}$$

For the outer channel, the geometric area is defined by the total area of the channel (A_{out}), from which the area of the vanes is subtracted. The area of the vanes is calculated by multiplying the number of vanes (N_{vanes}) with the cross-sectional area of a single vane (A_{vane}). This results in the following equation for the geometric area:

$$A_{outer} = A_{out} - N_{vanes}A_{vane} \tag{4.5}$$

Using equation 4.3, the mass flow trough the two channels can be calculated:

$$\dot{m}_{inner} = A_{inner}\sqrt{2\rho\Delta P_{LSI}} = 0.0432\text{kg/s}$$

$$\tag{4.6}$$

$$\dot{m}_{outer} = A_{outer}\sqrt{2\rho\Delta P_{LSI}} = 0.1329\text{kg/s}$$

The resulting total, calculated mass flow from equation 4.6 is 176.1 g/s. The calculated flow is smaller than the mass flow measured during the experiment (185.6 g/s), but the difference is considered small enough to be negligible. With the calculated flows, the mass fractions of the inner and outer channel can be calculated:

$$F_{inner} = \frac{\dot{m}_{inner}}{\dot{m}_{inner} + \dot{m}_{outer}} = 0.245 \tag{4.7}$$

Which means that the outer mass fraction (F_{outer}) is equal to $1 - F_{inner} = 0.755$. As a conclusion, the mass flow split between the inner and outer channel is set at 1:3 (inner:outer). In the outer channel, the vanes divert the flow outwards, with an angle of $37°$ away from the center line. The turbulence parameters at the inflow can be calculated: a turbulent length scale and a turbulent intensity. The turbulent length scale, l_t, is defined for both channels; the inner channel l_t is equal to the diameter of the holes (2.6 mm), for the outer channel the inner channel diameter is subtracted from the outer channel diameter ($7mm$). The turbulent intensity is calculated at the centerline using the average velocity in the combustion chamber, taken from the experiment: u'/U_0.

All the important parameters used in Fluent for the two inlets can be seen in table 4.2:

Table 4.2: Parameters used for Fluent simulations

Parameter	Abreviation	Inner Channel	Outer Channel	Units
Mass Flow Split	–	24.5	75.5	[%]
Total Mass Flow	$\dot{m}$	43.2	132.9	[g/s]
Equivalence Ratio	ϕ	0.715	0.715	[–]
Axial Velocity	U	27.8	63.6	[m/s]
Tangential Velocity	W	0	44.6	[m/s]
Radial Velocity	V	0	0	[m/s]
Turbulent Length Scale	l_t	2.6	7	[mm]
Turbulent Intensity	u'/U^0	5	5	[%]
Vane Angle	α_{vane}	-	37	[°]
Diameter	D	26	38	[mm]

4.1.4 Settings in Fluent

Before simulating the combustion in the LSB, the non-reacting- or cold flow is simulated first. Because non-reacting flows do not include chemistry, a lot less computational power is needed. The solution will also converge earlier. Therefore it is easier to simulate the cold flow, analyzing the results and correct setup parameters to improve the solution. The determined parameters of the cold flow will be used as a starting point for the reacting- or hot flow.

The result of the most important determined simulation parameters can be found in table 4.3:

Table 4.3: Modelling conditions.

General	
Time	Steady
Dimension	2D
Symmetry	Axisymmetry
Materials	
Mixture	Methane Air 2-Step
Fluid	Air
Density	Ideal Gas
Solution methods	
Scheme	SIMPLE
Discretisation	Second Order Upwind
Solver	Pressure-Velocity Coupling
Models	
Energy	On
o f Turbulence	$\kappa - \epsilon$ model, Enhanced Wall Treatment
Species Transport	Volumetric Eddy-Dissipation
Boundary Conditions	
Inlet	Mass-flow-Inlet
Outlet	Pressure-outlet
Walls	Constant Heat Flux, No Slip
Geometry	
Length of domain	290 [mm]
Width of domain	75 [mm]
Minimum element size	10^{-4}[m]
Maximum element size	10^{-3}[m]
Number of mesh elements	46,752

4.2 Non-Reacting Simulations

For the non-reacting simulations, the data of the non-reacting experiment are used and compared. From the experiments, velocity profiles are available; the axial velocity is measured in the radial direction and at the centerline. To mimic these velocities, the geometry of the experiment has to be translated into Fluent first. The computational domain to consider can be seen in figure 4.4. A close-up from the inlet region is given in figure 4.5:

Figure 4.4: Sketch of the computational design
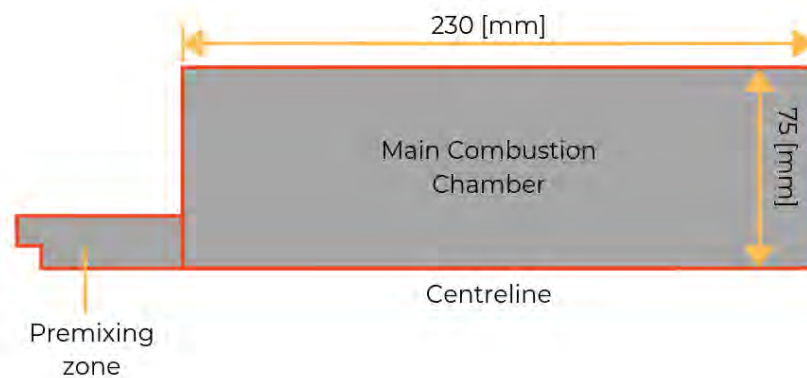

Figure 4.5: Sketch of the premixing zone

The results of the non-reacting simulations on this domain can be seen in figures 4.6 and 4.7. In 4.6, the axial velocity profile in the radial direction is given. This profile is measured 7 mm after the end of the premixing zone. The temperature in the computational domain is 450 K and the inlet velocity, U_0, is 47 m/s.
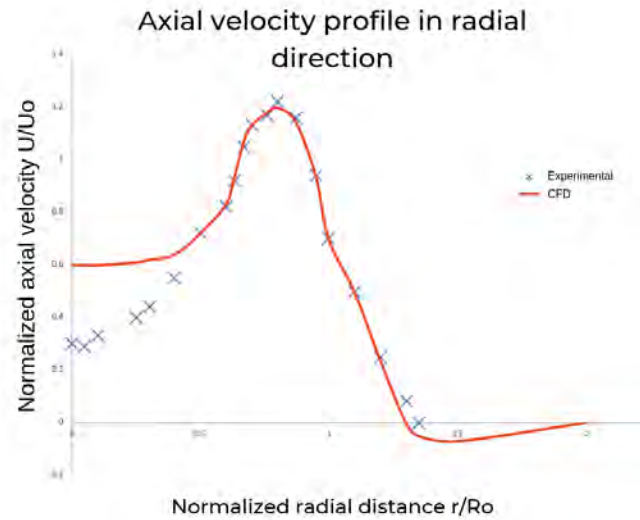
Figure 4.6: Axial velocity profile in the radial direction. $T = 450K, U_0 = 47m/s$.
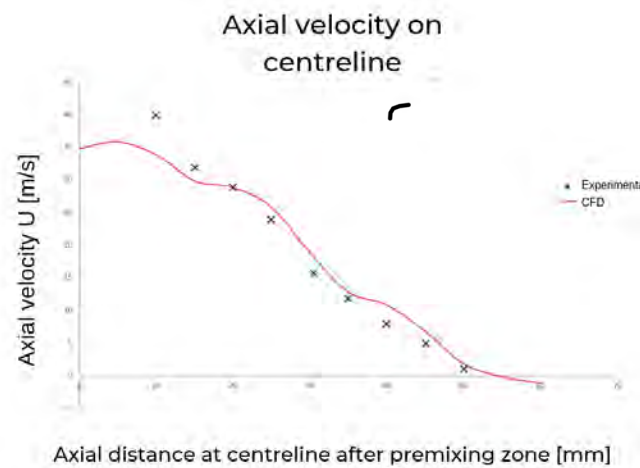
Figure 4.7: Axial velocity on the centreline. $T = 450K, U_0 = 47m/s$.

When studying the axial velocity profiles, the conclusion is drawn that the used parameters and settings are validated. The main difference between the experimental and computational results is the difference between the axial velocity in the inner zone. This is the region between 0 and 0.5 r/R_0 in figure 4.6. A lot of assumptions have been made to transfer the LSI from three into two dimensions, which might explain this difference. The validated setup can now be used to take the next step: model the reacting phase.

4.3 Reacting Simulations

To model the reacting flow, all settings remain the same as for the non-reacting flow. The only difference is that the species transport model (Volumetric Eddy-Dissipation) is switched on. To

validate the model, the results of the simulation will be compared with photos from the experiment [5]. In figure 4.8 a photo is compared with the simulated temperature contours, figure 4.9 the photo is compared to the reaction rate.
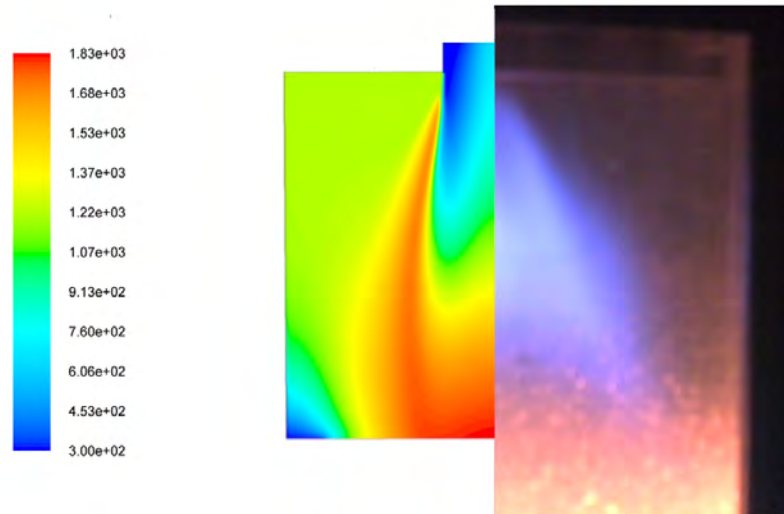
Figure 4.8: Comparison between the simulated temperature contours and a photo from the flame.

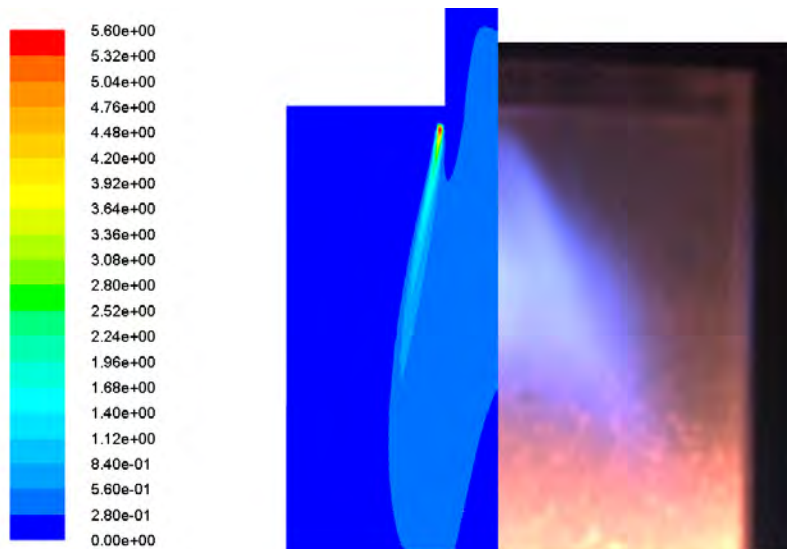

Figure 4.9: Comparison between the simulated reaction rate contours and a photo from the flame.

Because of the similarity between the photo and the reaction rate contours, in combination with the matching velocity profiles, the conclusion is drawn that the computational model for the LSB is validated. This model can now be used to model the LSB used at the Eindhoven University of Technology.

Chapter 5

Low Swirl Burner of Eindhoven University of Technology

In this chapter, simulations will be performed on the experimental low swirl burner setup at the Eindhoven University of Technology. The first step is to model pure methane combustion, after which the iron particle combustion model will be implemented step-wise, creating a hybrid metal-methane-air mixture. The last step is to explore the possibility of pure iron combustion.

5.1   The Burner

A CAD drawing of the experimental burner setup can be seen in figure 5.1. Note that in this figure only the burner is shown, the iron dispersion system is not shown. The burner is built from five different parts: four brass parts and a swirler made out of titanium. The first three parts, labelled 1, 2 and 3, are used to increase the turbulence of the flow carrying the iron-air dispersion to prevent particles sticking to the walls and/or falling back down into the burner. Part four and five are the focus area of this study. Part 4 is a straight guide with a diameter of $D_{guide} = 25$ mm. Part 5 is the swirl element. A schematic drawing of the swirl element can be seen in figure 5.2. The dimensions of the swirl element of the experimental setup are:

- α is 37°, the vane angle,

- R is 50 $[mm]$, the length from the vane until the expansion,

- R_h is 44 $[mm]$the length from the center plate until the

  expansion,

- U_{in} is 7.5 $[mm]$, the radius of the center plate,

- U_o is 5.0 $[mm]$, the width of the swirler.

The translation into a geometry that can be modelled using CFD is done the same as in chapter 4. A summarizing sketch of the computational design can be seen in figure 5.3 and 5.4. More detailed drawings can be found in Appendix E.

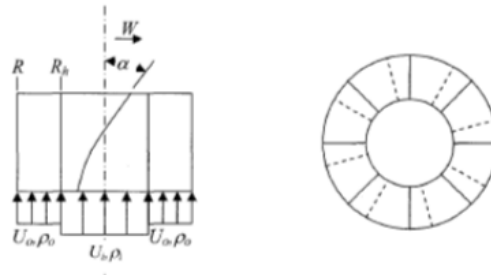Figure 5.1: Graphical description of the Low Swirl Burner

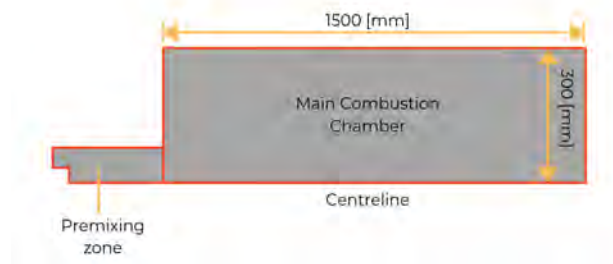Figure 5.2: Schematical drawing of the swirl element

Figure 5.3: Sketch of the computational design for LSB TU/e

Figure 5.4: Sketch of the premixing zone for LSB TU/e

5.2 The Dispenser

To add iron particles to the burner, a dispenser is used which combines particles and air and injects this dispersed flow into the burner. This dispersion system is currently the bottleneck of the experimental setup. There are problems with leakage, maintaining a constant flow and creating uniform dispersion of particles in the airflow. The system will be improved, so the assumption for this study is made that the system function perfectly, and the parameters for the iron-air flow, used for the simulations, are taken from this dispersion system.

A summarizing figure of the dispenser can be seen in figure 5.5, and consists of 3 main components: transporter disks, a hopper and a dispenser. The hopper, which can be seen on the right, stores and feeds the iron powder to the disks. The disks transport the powder via a groove to the dispenser, which can be seen on the left. The dispenser mixes the iron powder with air and injects the dispersed flow into the burner. In the center a spring can be seen, which compresses the two disks. To transport the iron powder, the disks turn, powered by a motor. A cut through of the dispenser can be found in Appendix E.
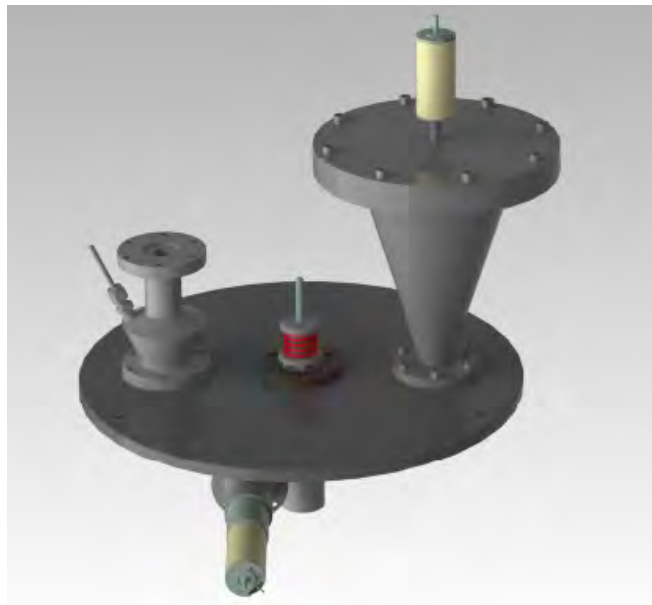

Figure 5.5: Computer aided design of the dispenser.

5.3   Methane Combustion

The first simulations done on the TU/e LSB are the combustion of methane (CH_4). These simulations are compared with the validated burner in chapter 4.The computational parameters used for this simulation are largely the same as for the validated burner and are summarized in table 4.3.

The main differences are the geometry and inlet boundary conditions. These are summarized in table 5.2 below:

Table 5.1: Parameters used for Fluent simulations LSB TU/e

Parameter	Abreviation	Inner Channel	Outer Channel	Units
Mass Flow Split	$-$	24.5	75.5	[%]
Total Mass Flow	$\dot{m}$	1.27	4.38	[g/s]
Equivalence Ratio	ϕ	0.76	0.76	[$-$]
Axial Velocity	U	0.54	1.53	[m/s]
Tangential Velocity	W	0	1.21	[m/s]
Radial Velocity	V	0	0	[m/s]
Turbulent Length Scale	l_t	7	7	[mm]
Turbulent Intensity	u'/U^0	5	3.9	[%]
Vane Angle	α_{vane}	-	37	[°]
Diameter	D	15	25	[mm]

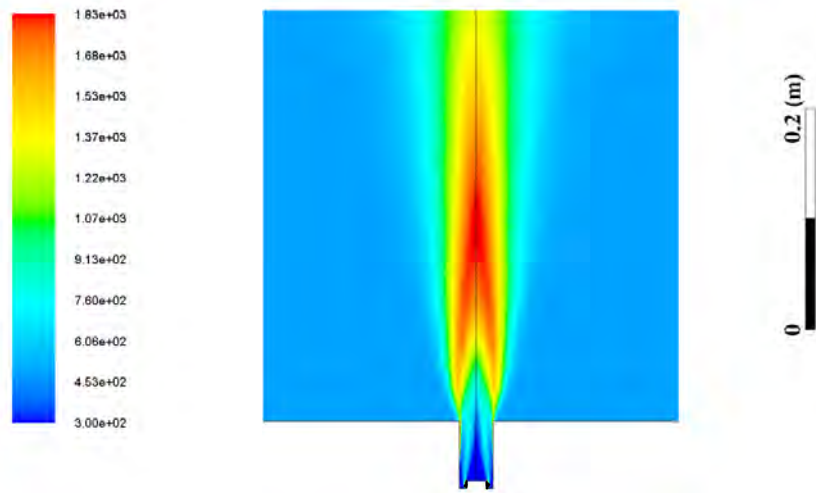This results in the following temperature profile for the LSB:

Figure 5.6: Flame temperature profile for methane flame of the TU/e LSB.

This temperature profile is compared with the profile from the validated burner, figure 4.8. The maximal flame temperature of both LSB's is very similar (1826 vs 1798 K). Also, the velocity profiles and turbulence intensity shows significant similarity. The shape of the flames is different, however. This difference can be explained by the bigger pressure of the validated burner (4 vs 1 atm) and the limited geometry versus the bigger (open) geometry of the TU/e LSB.

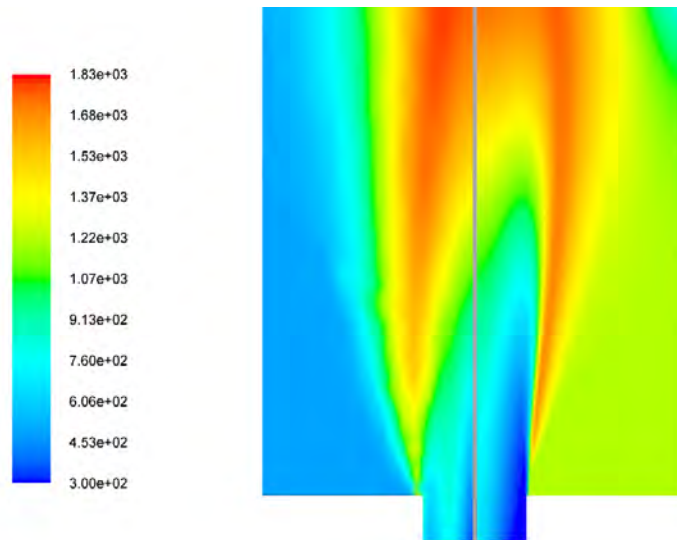Figure 5.7: Flame temperature profile for methane flame of the TU/e LSB (Left) and the validated burner (Right).

5.3.1 Validation

From the first comparison between the TU/e LSB and the validated LSB, many similarities can be seen. However an extra validation is performed to check if the simulation is correct; the static temperature profile at the axial distance from the burner front is compared with another similar

burner (Low Swirl, methane combustion) from literature [20]. In hindsight, this setup shows a lot more similarities with the TU/e LSB and would have been a more suitable choice to perform the initial validation. Due to time limitations and enough confidence in the original validation being correct, the validation is not done again on this burner. However, it is used to validate the LSB TU/e by comparing the temperature profile, which can be seen in figure 5.8. As seen in the figure, the velocity profiles follow the same line, where the main difference is that the distance of the lift is lower for the LSB TU/e.

At this point the conclusion can be drawn that the LSB is validated and simulations with iron combustion can be performed. In Appendix B more figures and data from the simulations of the LSB with methane can be seen.
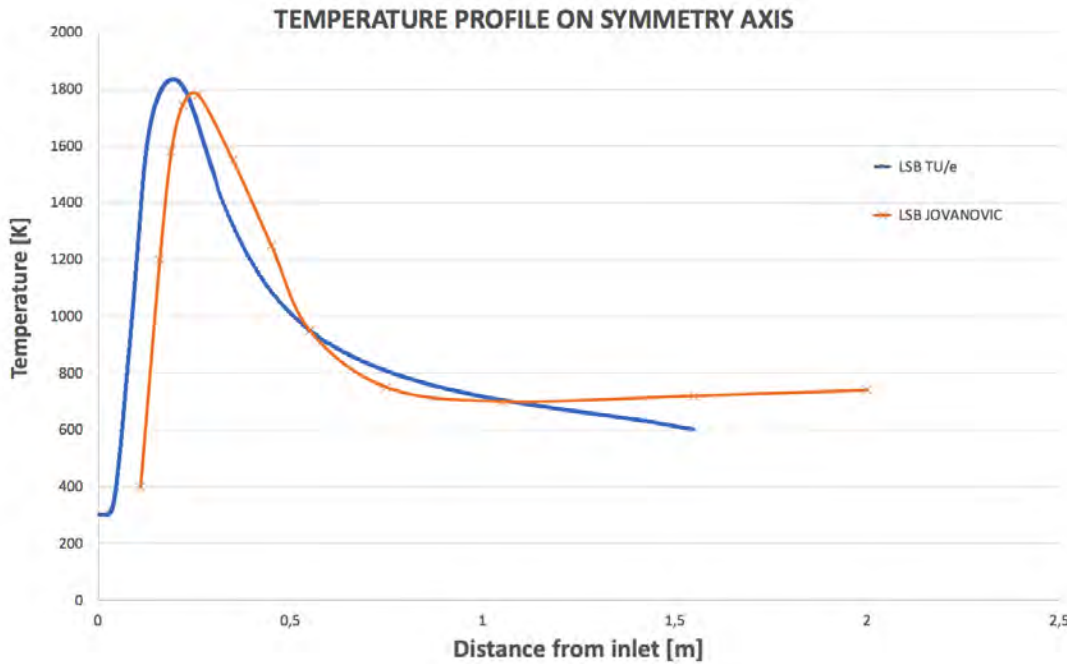

Figure 5.8: Flame temperature profile as function of the axial distance. For the LSB TU/e (blue) and a LSB from literature [20].

5.3.2 Grid independence study

Before continuing the simulations a grid independence study was conducted, to determine if the solution is grid independent. First four different meshes were used in simulations, where the mesh size was determined by using face sizing. Because of the simplicity of the geometry, square elements can be used. The four different face sizes, in m, used are:

- $1.0 * 10^{-3}$
- $1.0 * 10^{-4}$
- $7.5 * 10^{-5}$
- $5.0 * 10^{-5}$

To check for independence, the static temperature at different axial distances is compared. This is similar to the validation done in figure 5.8. The results of the temperature profiles are presented in figure 5.9. There is no clear difference anymore between the profiles of the face sizes $7.5 * 10^{-5}$ and $5.0 * 10^{-5}$ m. Therefore, the mesh with a face size of $7.5 * 10^{-5}$ could be adopted

as a suitable mesh. However, simulations on this mesh are very time-consuming. Therefore, the decision is made to create a new mesh and improving the mesh size locally. Especially around the inlet area and the walls, the cell number of the mesh is increased. This results in a simpler mesh with fewer elements.

The mesh created by only using face sizing of $7.5 * 10^{-5}$ consisted of more than $1.5 * 10^6$ elements. The mesh created by refining locally consists of 74,464 elements. This refined local mesh, however, results in precisely the same temperature profile as the mesh created by using face sizing. Because simulations on this mesh with fewer elements are less straining and therefore quicker, this mesh is adopted for all further calculations.

The reason that the locally refined mesh can achieve similar accuracy with significantly fewer elements, lies in the geometry of the burner. To model the open flame, the domain after the expansion of the swirler is rather large. Most of the reactions, however, happen around this inlet. So the need for a large amount of elements is higher in this region than it is in the rest of the domain.
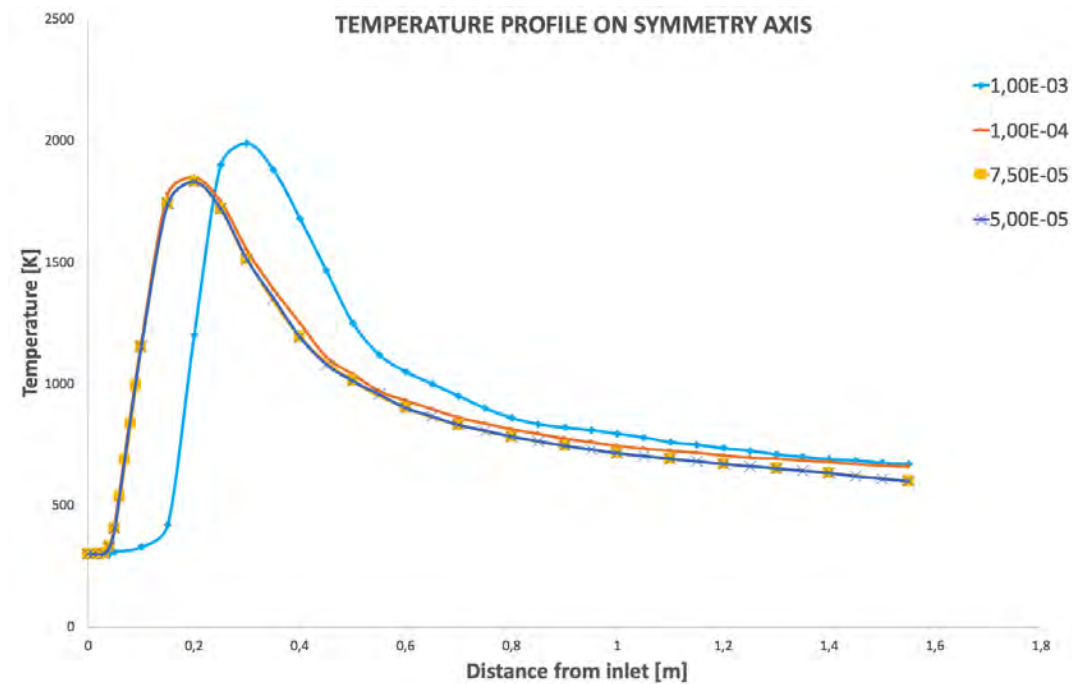

Figure 5.9: Flame temperature profile as function of the axial distance. For different sizes of the generated mesh.

5.4 Iron Combustion Principles

5.4.1 Iron Powder

There are two types of powder that are used during experiments on the LSB, which can be seen in table 5.2:

Table 5.2: Iron powders used for experiments

Name	Company	Type	Size	Purity
FE300	CNPC	Sponge Iron	45 $[\mu m]$	$> 99\%$
44890	Aldrich	Carbonyl Iron	5-9 $[\mu m]$	$> 99.5\%$

Simulations will be performed with both types of powder. To check the behavior of the different powder both diameters are used. The assumption is made that both particles consist of 100% pure iron.

5.4.2   Inert heating

To check the behavior of the different sized iron particles, first, they will be modelled as inert particles. The particles are injected as a single particle into the fully converged solution of methane combustion. The iron particles will be compared with an inert particle from the standard discrete phase model. This inert particle uses the material properties of anthracite: C_p= 1680 J/kgK and $\rho = 1550 \ kg/m^3$

To calculate the temperature of a single particle, a heat balance is used in FLUENT. This heat balance relates the particle temperature, $T_p(t)$, to the convective heat transfer and to the absorption/emission of radiation at the particle surface. This heat balance is:

$$m_p c_p \frac{dT_p}{dt} = hA_p(T_\infty - T_p) + \epsilon_p A_p \sigma(\theta_\infty^4 - T_p^4) \qquad (5.1)$$

Equation 5.1 only holds if the particle temperature is less than the vaporization temperature, T_{vap}, or:

$$T_p < T_{vap} \qquad (5.2)$$

When the particle reaches T_{vap}, mass transfer laws need to be obeyed. This could complicate the simulations, as mass transfer is not (yet) considered in the UDF of the iron particles. For inert simulations, however, this limit is not reached. So, in this case, the stated problem does not exist. In figure 5.10 the inert heating of an iron and an anthracite particle can be seen. Both particles follow the same flame temperature profile as in 5.8, but do not reach the same maximum temperature. This is expected because the time frame in which the particles are heated is small: the particles reach a maximum axial (X-direction) velocity of 21.1 m/s .

The difference between the iron and the anthracite particle is also expected: because of the lower specific heat for iron this particle will heat up and cool down quicker than the anthracite particle. Adding heat to a low specific heat compound will increase its temperature more quickly than adding heat to a high specific heat compound.
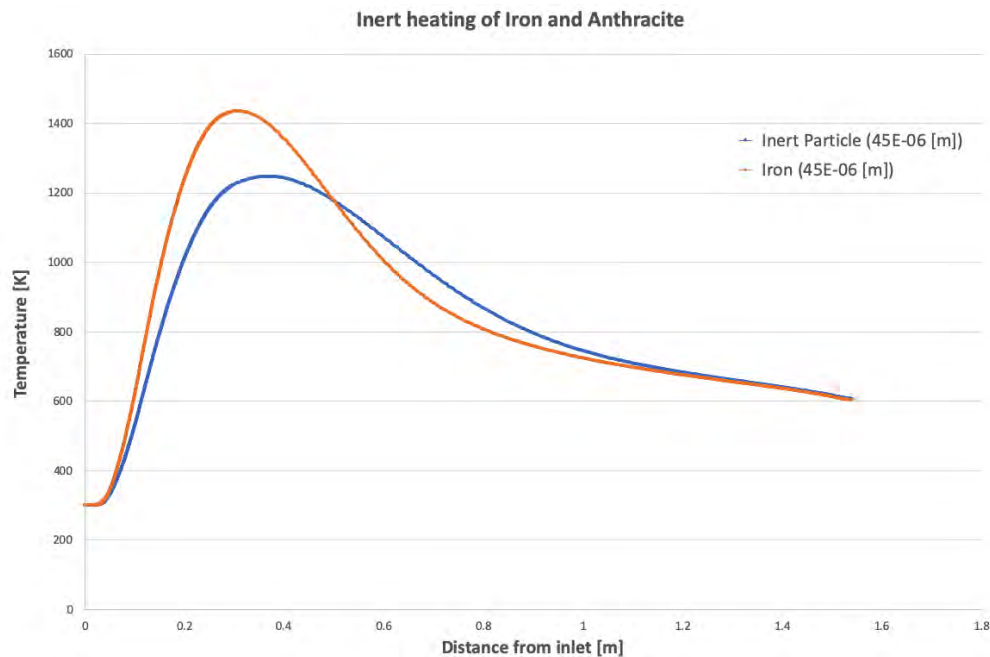
Figure 5.10: Flame temperature profile as function of the axial distance. For a single inert iron and anthracite particle (45 μm).

A simulation is also performed with the two different iron particle sizes (45 and 5 μm). The two different sizes are injected into the burner at two different locations; in the central region and in the swirler region. For the 5 μm particle at the centre this resulted in an error. As stated before, the particle temperature cannot exceed the vaporization temperature. This was the case for this particle.

To overcome the problem, the model is adjusted slightly for only this specific simulation: T_{melt} for Fe and Fe_3O_4 was set to 1900 K. This solved the error, the maximum temperature of the 5 μm particle appeared to be slightly higher than the set decomposition temperature: 1831.44 K. The original decomposition temperature was 1809 K.

The result of the inert heating of the various particles can be seen in figure 5.11. The most important conclusion that can be drawn from this figure is that for both particle sizes, and at both inlet locations, the particle temperature will exceed the ignition temperature (700 K). This means, at least for single particles, that iron combustion will occur when adding particles to the methane flame.
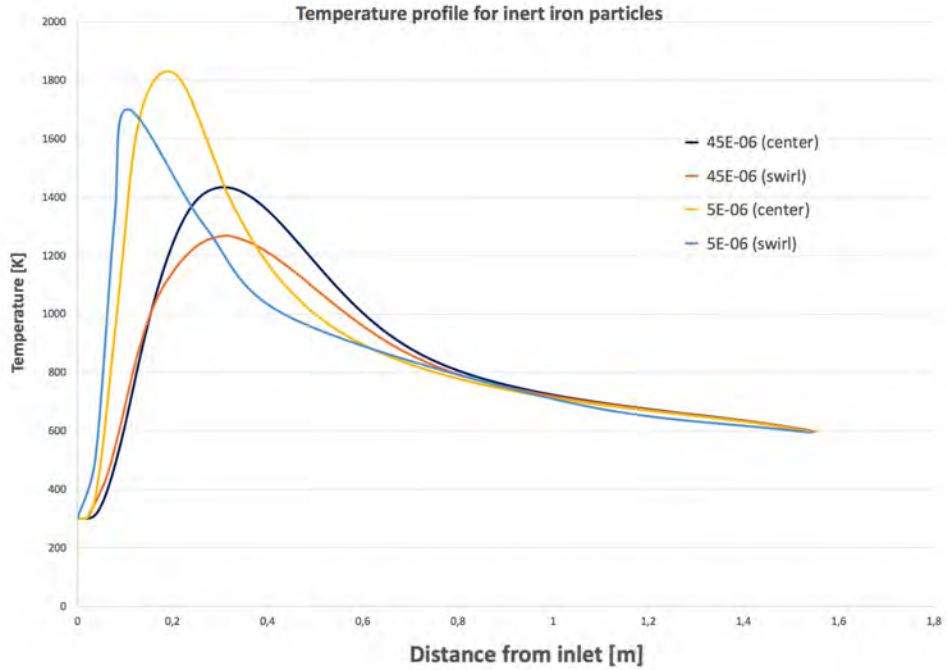
Figure 5.11: Flame temperature profile as function of the axial distance. For different particle sizes and inlet locations.

5.5 Iron and Methane Combined

In this section different amounts and size of iron will be added to the methane flame. The advantage of numerical simulations is that there is virtually no limit on the different (boundary) conditions that can be set. In this case there is no specific limit set by the experimental setup. For example, if the burner performs much better with a wider outlet, this can be determined by using the simulations and given as a recommendation for the experimental setup. As a starting point, however, the conditions of the experimental setup will be used.

5.5.1 Experimental Setup Conditions

The relevant mass flow controllers (MFC) of the experimental setup are summarized in table 5.3. The maximal values that can be obtained for these controllers are measured in L/min.

Table 5.3: Mass Flows controllers of the experimental setup

Controller	Flow	Maximal value
MFC1	Airflow	228 $[L/min]$
MFC3	Methane flow	20 $[L/min]$
MFC4	Dispersion flow	38 $[L/min]$

Before calculating the stoichiometric combustion ratios for iron, methane and air, simulations are performed where different amounts of iron are added to the converged solution of methane combustion (section 5.3). Using the converged solution means that the amount of oxygen and

methane (and all other reaction products) are predefined at the moment the iron is injected: iron will be added to a stable methane flame. For example, in the first simulations, no extra oxygen is added; only pure iron particles are injected.

5.5.2 Simulations with small amounts of iron

For the first simulation, only $1.0 * 10^{-20}$ kg of iron is injected, with a particle size of 45 μm. The particle tracks of the iron particles can be seen in figure 5.12. The particle tracks are colored by the temperature of the particle.
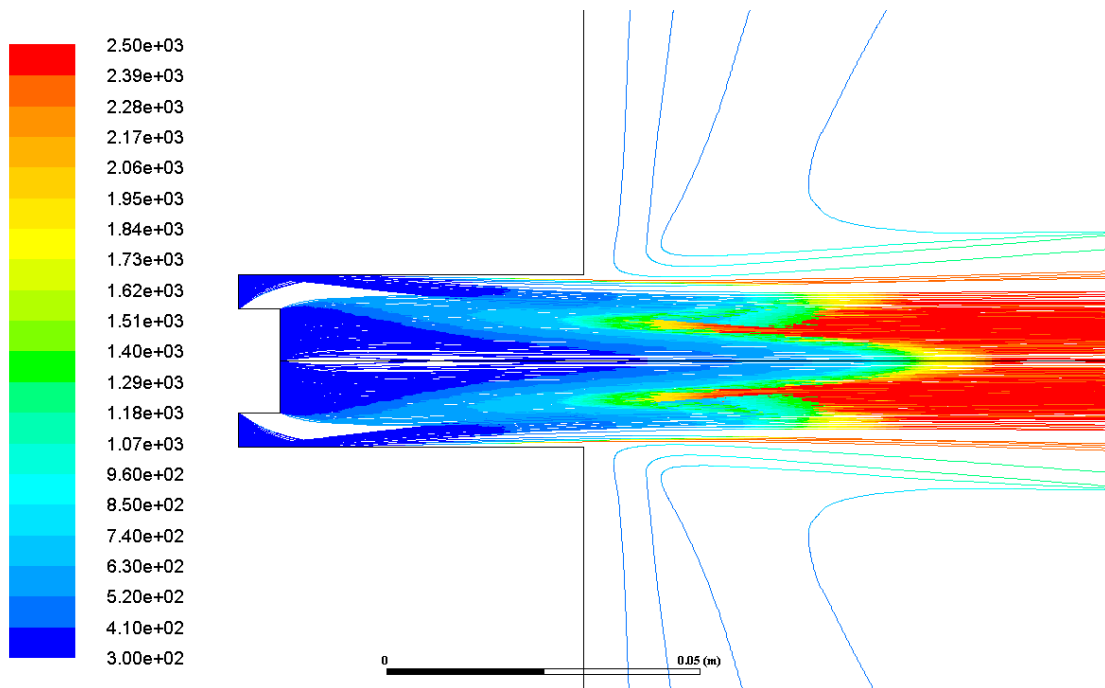

Figure 5.12: Particle tracks of iron particles, colored by particle temperature
.

When looking at the temperature profile of different particles during the combustion, it can be seen that the profile follows the expected temperature profile; the paths are almost identical to the path created by the drop tube simulation (figure 3.6 & 3.7).
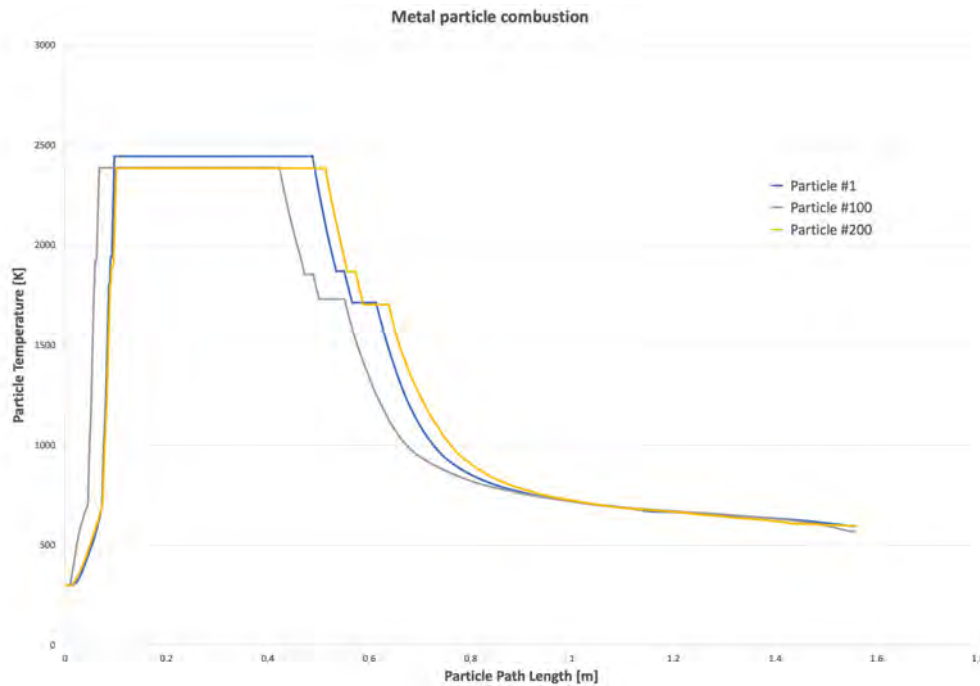
Figure 5.13: Temperature profile for iron particles. ($1 * 10^{-20}$ kg, size: 45 μm).

When performing the same simulation with the smaller, 5 μm particles, the results deviate from the results with the larger particles. It appears that the 5 μm particles combust too quickly in the methane flame: you see them combusting, start cooling down and then heat up again by the methane flame. Additional simulations need to be performed to find if there are boundary conditions that are better suited for the smaller particles. The temperature profile from a single particle track can be seen in figure 5.14.
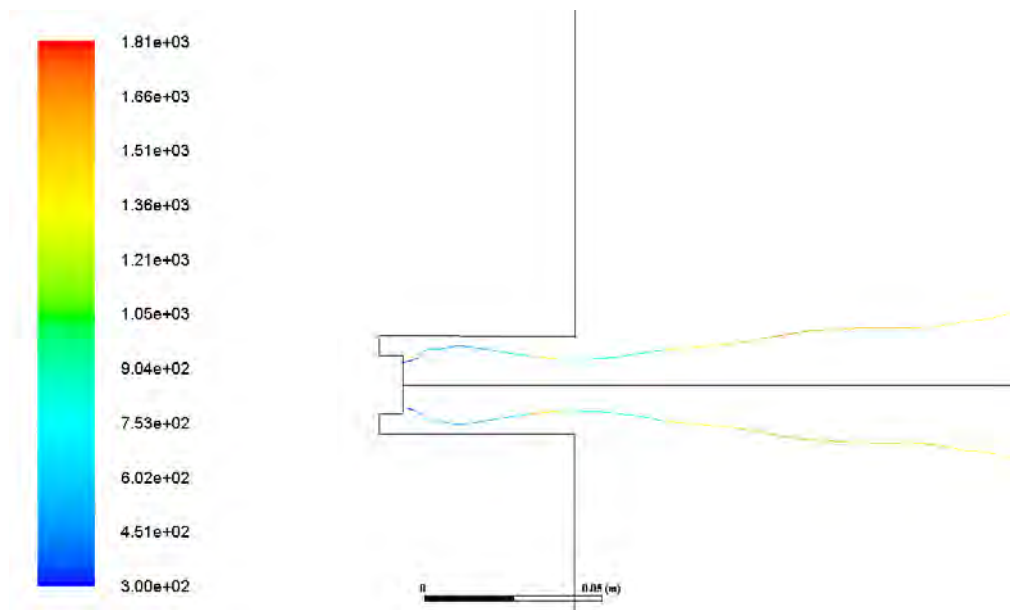

Figure 5.14: Particle track and temperature profile for a 5 μm particle in the methane flame.

Using such small amounts of (iron $1 * 10^{-20}$ kg) does not lead to any significant changes in the temperature of the methane flame. This is expected, the mass is simply too small to make an impact. To make an approximation about the mass needed to make an impact on the temperature of the methane flame, some back-of-the-envelope style calculations are made. First, the generated power by combusting iron is calculated with equation 5.3:

$$P = \dot{m}u \tag{5.3}$$

where:

- P is the generated power in Watts $[W]$,

- $\dot{m}$ is the mass flow in grams per second $[g/s]$,

- u is the energy density, for iron a value of 5.2 $[kJ/g]$ is taken.

Using this equation, a simple linear increase in the amount of generated power is realized when the mass flow is increased. When keeping the amount of methane constant, and increasing the amount of iron, the percentage of the power generated by iron can be calculated. At 0.1 g/s iron, this percentage is 4 %. Therefore, the first simulations will be performed with a mass flow starting at 0.1 g/s. Following the results from these simulations, the mass flow will be increased or decreased. When comparing the amounts of iron and methane, the ratio between iron and methane is 1:2,25 when adding 0.1 g/s of iron. So a significant amount of iron will be a part of the fuel.

5.5.3   Iron 0.1 g/s

Performing the simulations with the smaller 5 μm leads to strange and unrealistic results. The cause lies probably in the combustion rate of the smaller particles, as mentioned in section 5.5.2 and figure 5.14. Also, when performing the real-life experiments on the setup at the TU/e, a mode in which a stable flame was obtained was not found. Combining these two factors leads to the decision to shift the focus on only the 45 μm particles.

Adding the 45 μm particles leads to the graph in figure 5.15, and does not deviate from the expected result; the beginning of the profile does not change, there is no combustion in this region. The maximum temperature rises a little, which can have multiple causes; there is a rise in temperature because of the heat generated by the iron particle combustion and the equivalence ratio becomes closer to 1 because oxygen is consumed.
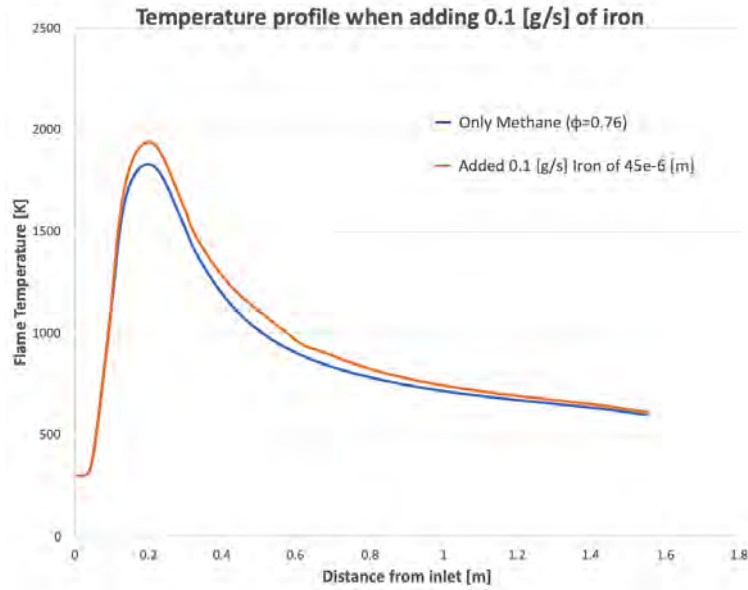
Figure 5.15: Temperature profile when adding 0.1 g/s of iron 45 μm particles in a methane flame.

5.5.4 Increasing the amount of iron

After the successful result of adding a first, small amount of iron, the amount of iron will be increased. The simulations will be performed by incrementally increasing the amount of iron in the fuel; the steps taken are summarized in table 5.4 below. Taking into account the dispenser of the experimental setup, the maximum airflow that can be added to the iron particles is 38 L/min, or 0,633 L/s. This airflow is added to the particles, increasing the total mass flow of air to 6,41 g/s.

Table 5.4: Amount of iron added to the fuel

Amount of iron kg/s	Ratio $Fe : CH_4$	Result
$2.25 * 10^{-4}$	1:1	Stable
$4.00 * 10^{-4}$	1.78:1	Stable
$8.00 * 10^{-4}$	3.56:1	Stable
$1.50 * 10^{-3}$	6.67:1	Stable
$3.00 * 10^{-3}$	13.3:1	Unstable

Again the temperature profile is plotted, now for every different fuel composition. This can be seen in the graph in figure 5.16. In this graph, it is shown that increasing the amount of iron leads to a temperature increase of the flame. There is, however, a point where the flame becomes 'saturated' with fuel (or depleted of oxygen). This can be seen when increasing the amount of iron from 1.5 to 3.0 g/s; at this point, the flame temperature drops significantly. The reason for this

drop is the amount of oxygen present in the flame. At one point, there is no more oxygen left for the combustion reactions (equation 3.2).

The lack of oxygen can also be seen when looking at the temperature profile of a single particle. There are no more jumps or plateaus in the profile, just a gradual increase and decrease of the temperature. The conclusion taken from this profile is that the particle heats up, and thus takes out the heat of the flame. No reactions occur anymore. The profile can be seen in figure 5.17. When performing simulations, the first point at which the quenching of the flame can be seen lays around 2 g/s. At this point almost no CH_4 combusts anymore, and the iron flame is highly saturated: $\phi = 1{,}49$ (if no CH_4 combusts).

The temperature contours for the different iron amounts are pictured in figure 5.18. Here it can be seen that the basic shape of the flame stays the same, only the temperature rises when the amount of iron in the fuel is increased. Note that the colormaps on the different images are scaled to fixed values. The pictures with an unscaled colormap can be found in appendix D. A picture of the quenched flame at 3 g/s can be found here as well.
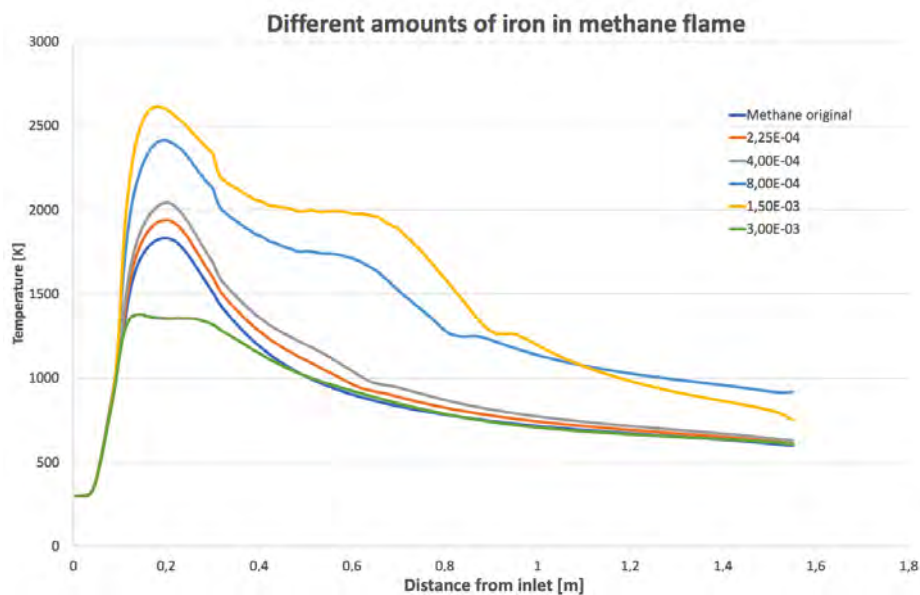

Figure 5.16: Temperature profile when adding different amounts of iron 45 [μm] particles in a methane flame.
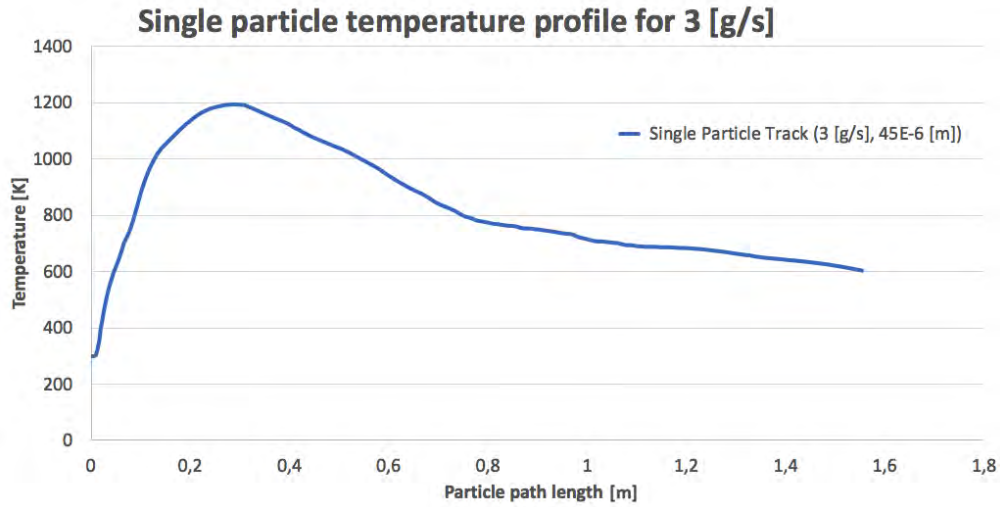
Figure 5.17: Temperature profile for a single iron 45 $[\mu m]$ particles when adding 3 $[g/s]$.
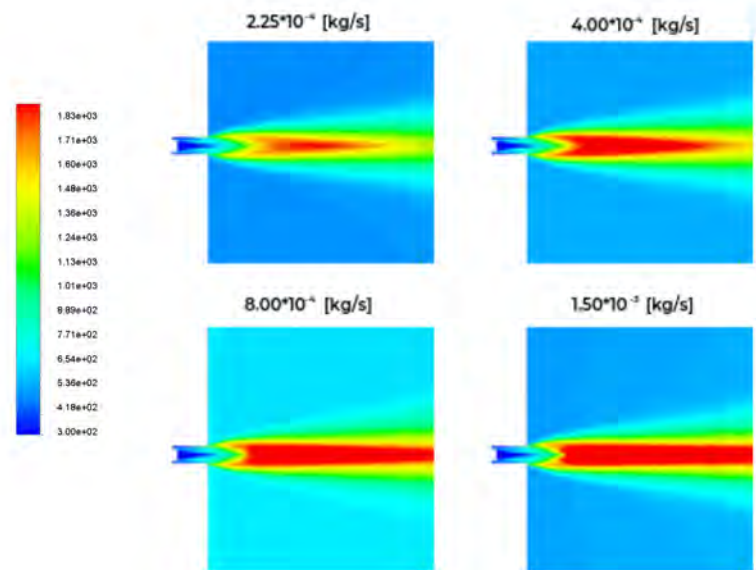

Figure 5.18: Temperature contours for the different amounts of added iron.

The contours of the mass fractions of CH_4 and O_2 can be found in figure 5.19 and 5.20 below. From these contours it can be seen that when increasing the amount of iron, the amount of oxygen decreases. Also, the amount of reacting methane decreases: less and less methane combusts when the mass of iron particles increases. The mass fractions as a function of the axial distance can be seen in figure 5.21. In the graph in figure 5.21 a strange observation can be made: at 0.4 m from the inlet the mass fraction of CH_4 starts decreasing, but a this point all oxygen is already depleted. A explanation is that at this point the methane diffuses, as the mass fraction is measured on a straight line. However, this does not explain the difference between the $8.00 * 10^{-4}$ and the $1.50 * 10^{-3}$ flows.
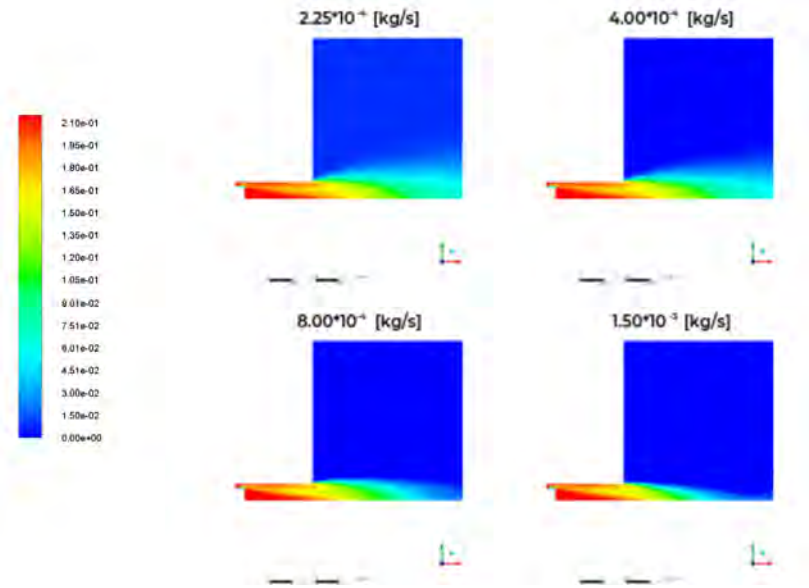
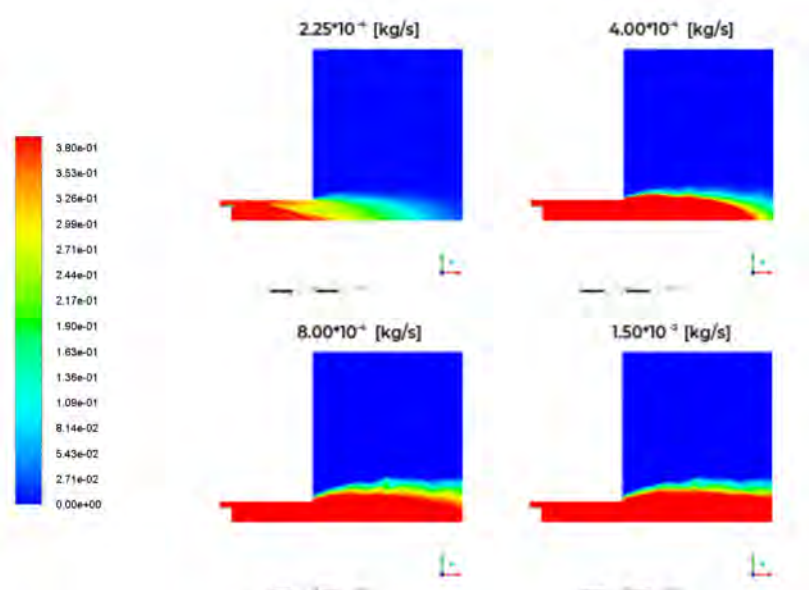Figure 5.19: O_2 mass contours for the different amounts of added iron.

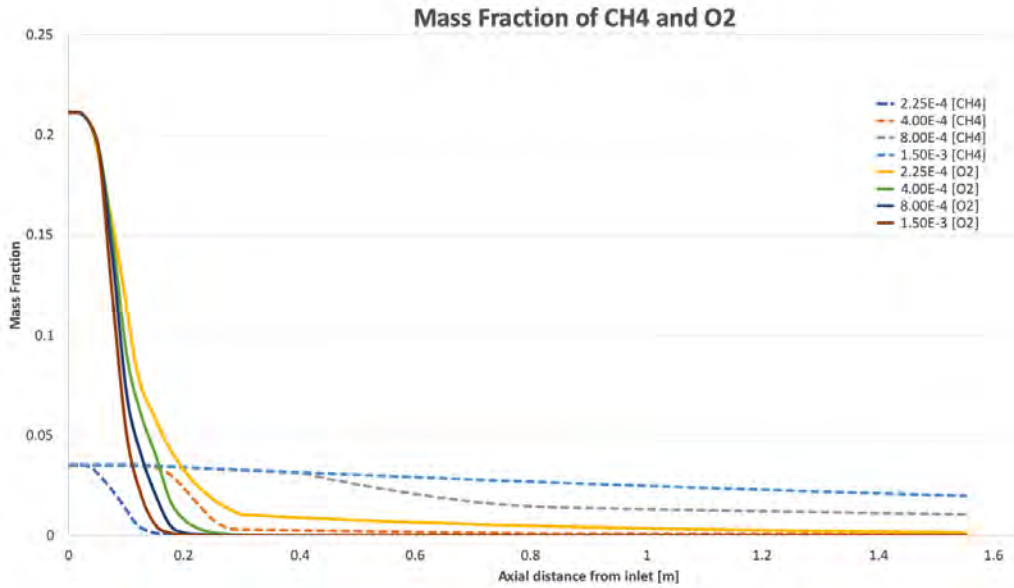Figure 5.20: CH_4 mass contours for the different amounts of added iron.

Figure 5.21: CH_4 and O_2 mass fraction as a function of the axial distance.

5.6   Iron Combustion

5.6.1   Stoichiometric Combustion of Iron

In the previous section, different amounts of iron where added to the methane flame. To take the next step of burning pure metals, stoichiometric conditions have to be calculated. This is done by determining the Fuel-to-Air ratio; the ratio is the mass of iron divided by the mass of air:

$$\left(F/A\right)_{st} = \frac{M_{Fe}}{M_{O_2} + M_{N_2}}$$

(5.4)

Again the equation for creating hematite is used (equation 3.2) along with the following material parameters:

Table 5.5: Material parameters used for stoichiometric calculations

	Fe	O_2	N_2	$\rightarrow$	Fe_2O_3	N_2
M	4	3	11.285		2	11.285
M_w [(g/mol)]	55.85	31.99	28.01		159.69	28.03
$Mass$ [g]	223.38	96.00	316.14		319.38	316.14

Using the parameters from table 5.5, the stoichiometric fuel-to-air ratio is calculated to be 0.542. The equivalence ratio is defined as the fuel-to-air ratio divided by the stoichiometric fuel-to-air ratio:

$$\phi = \frac{\left(F/A\right)}{\left(F/A\right)_{st}}$$

(5.5)

For stoichiometric combustion the equivalence ratio, ϕ, is equal to 1. Introducing the air density, ρ_{air} of 1.30 kg/m^3 and multiplying this with the equivalence ratio leads to the stoichiometric concentration:

$$\phi = \frac{\sigma_p}{\left(F/A\right)_{st} \times \rho_{air}} = 1.419\sigma_p \tag{5.6}$$

This finally leads to the stoichiometric concentration of iron: 705 g/m^3. This stoichiometric concentration has to be converted into a mass flow that can be used in the burner. To achieve this conversion, the design of the dispenser has to be taken into account:

$$\dot{m} = \left(F/A\right)\dot{v} \tag{5.7}$$

Where $\dot{v}$ is the airflow in the nozzle, calculated by using the exit velocity of the flame, v, and the area of the nozzle, A_{nozzle}:

$$\dot{v} = A_{nozzle}v \tag{5.8}$$

In the simulated burner this concentration would translate to an iron mass flow of 0.83 g/s. This calculated stoichiometric concentration functions as a starting point for the simulations of pure iron and air. The parameters for the simulations are kept the same as the ones for the methane combustion, which are summarized in table 4.2. The only exception is that the concentration of methane is set at zero. The mass flow of the iron is set at 0.83 g/s.

5.6.2 Non-combusting flow

Before simulating combustion, cold flow simulations are performed. During these simulations the particle tracks of the 45 μm particles can be inspected: they follow the velocity profile of the cold airflow. The particle tracks are colored by the velocity in the axial direction. These particle tracks can be seen in figure 5.22. Also, these simulations will be used as the base for the hot flow, or combusting, case. The cold flow case is run without any reacting species and consists of an airflow (0.21 % O_2) and an iron dispersion flow, consisting of pure iron particles.
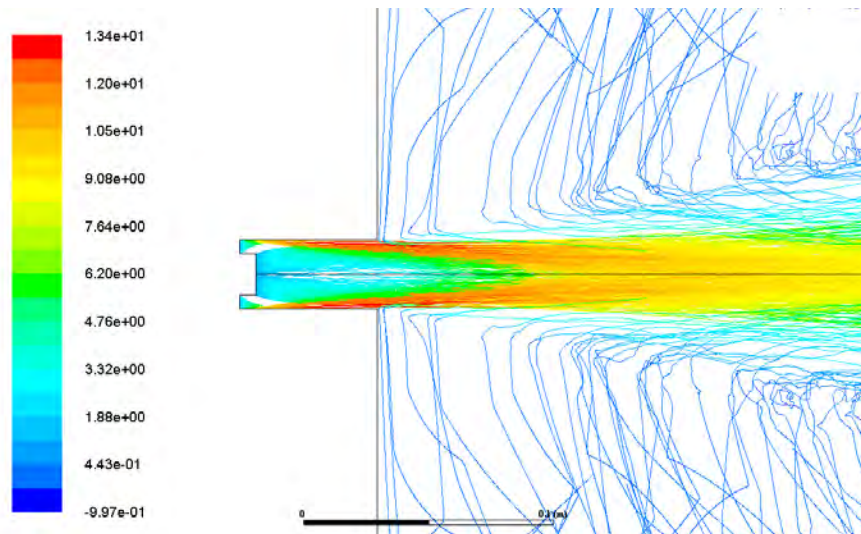

Figure 5.22: Particle tracks, coloured by axial velocity, for non-combusting flow.

5.6.3 Combusting flow

After running the cold-flow simulations, and obtaining a converged solution, the combusting case is investigated. This is done by 'igniting' the cold flow. Normally reactions have to be turned off during cold-flow simulations, but not in this case: because the only species present are oxygen and nitrogen at 300 K. This flow is interacting with the Discrete Phase Model, but these conditions do not cause ignition in the particles.

To do so, the entire region after the expansion of the inlet is patched at 1000 K, a temperature above the ignition temperature (700 K) of the model. This causes the iron dispersion to start combusting, and an iron-oxygen flame is obtained. When looking at the general shape of temperature-, velocity- and other relevant contours, the pure iron flame does not differ much from the methane-iron flame. The maximal temperature in the pure iron flame is even a little higher than the methane-iron flame; 2427 K vs 2385 K. The conclusion is drawn that the effect of the methane is relatively insignificant; the combustion properties of the iron are dominant. When adding a stoichiometric concentration of iron to a stoichiometric methane flame, the mass percentage of methane in the fuel is 21%; which also contributes to the low impact on the combustion dynamics.

There are, however, some differences between the two flames. For example, the total heat generated by the flame is of course greater for the methane-iron flame; more fuel is combusted in this flame. This can be seen, for example, in the temperature profile at the axis, which is pictured in figure 5.23. The maximal temperature point is quite similar, but after this point, the temperature of the iron flame drops quicker. Another big difference between the two flames is the amount of carbon-oxides in the flame. Because of the absence of carbon-based fuel, there is no CO_2 or CO present in the flame.
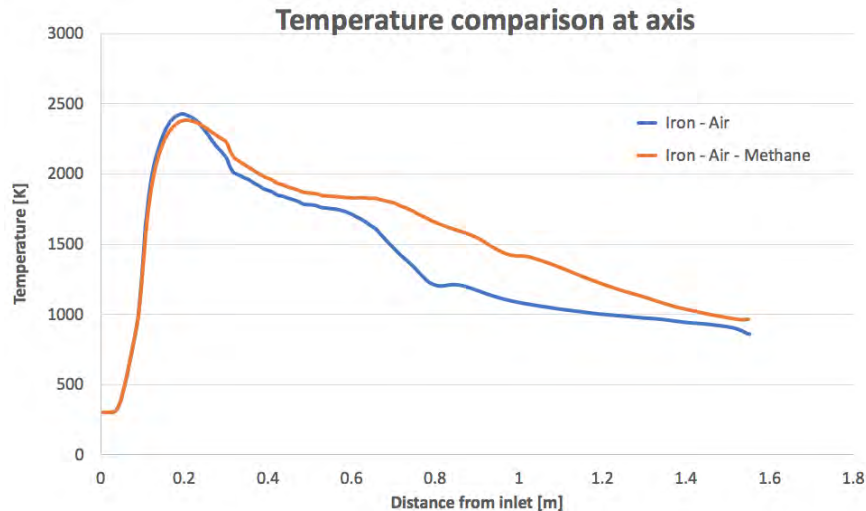

Figure 5.23: Temperature profile for pure iron and methane-iron combined, both with $8.3 * 10^{-4}$ kg/s of iron.

To perform some validation, the flame temperature of the pure iron flame is compared to measurements performed on iron particles: the McGill University in Montreal, Quebec performed experiments in a reduced-gravity environment, and flame temperatures were measured [14]. During these experiments, the flame temperature for different sized particles of stoichiometric iron combustion was determined. One of the measured particles has a size of 44.6 μm (Particle D in [14]). The measured flame temperature of this particle is 2410 K. This is very close to the

simulated flame temperature of 2427 K.

The temperature contours of the flame can be found in figure 5.24. The oxygen mass fraction contours can be found in 5.25.
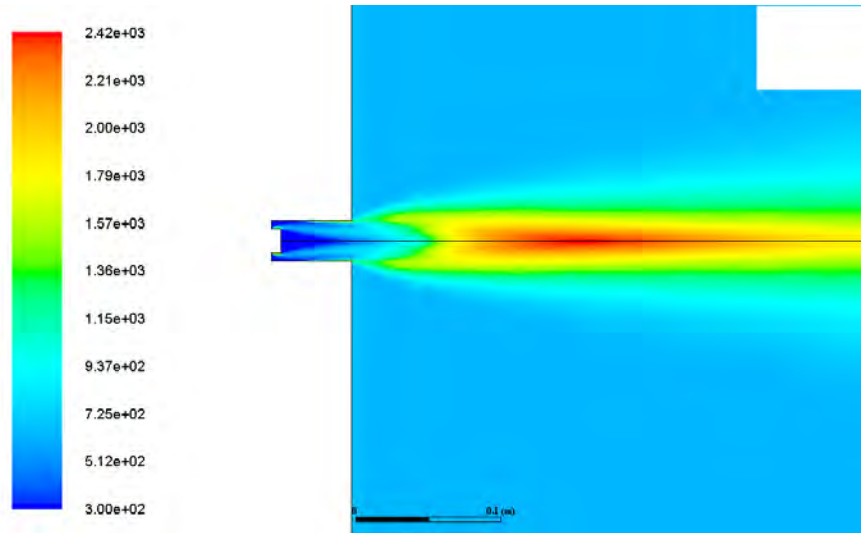

Figure 5.24: Temperature contours for 0.83 g/s iron with 1,35 g/s of air
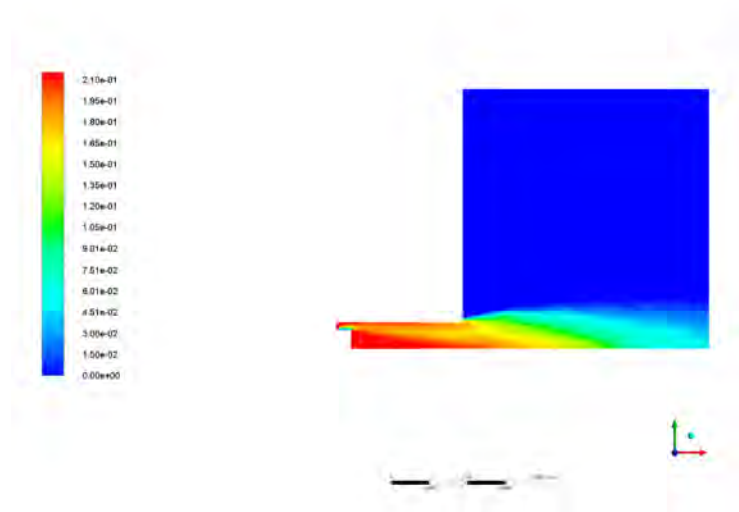
Figure 5.25: Oxygen contours for 0.83 g/s iron with 1,35 g/s of air

Extra figures from these simulations can be found in appendix C.

5.7 Swirler Position

As stated before, an advantage of computational fluid dynamics is that geometries can be adjusted easier than in real life. In the experimental LSB setup at the TU/e, the position of the swirler can be adjusted. Currently, experiments with the different positions have not been performed, but they could be done very well to validate the CFD model. Because the experimental setup

performs a lot better when a small part of the fuel consist of methane to sustain a stable flame, these simulations will be performed with a methane-iron flame. So, the fuel consist of 21% (0,226 g/s) methane, and 79% (0,830 g/s) of iron. The oxidizer consists of 6.41 g/s of air.

The swirler can be set at different positions, which varies the length of the inlet before the sudden expansion. The swirler can be set so the length of the inlet is 50, 100 or 150 mm. When looking at literature, the ideal length after the swirler and before the expansion lays between 1 and 3 times the diameter of the swirler [21]. In the case of the LSB TU/e setup, this would mean a distance between 25 and 75 mm.

This optimal length can be seen when simulating the different positions. It can be seen that the flame temperature drops for the positions at 4 (100 mm) and 6 (150 mm) times the swirler diameter. The flame shape for the 50 and 100 positions stills shows a lot of similarities, for the 150 position, however, the flame shape is different; instead of a lifted flame, the starts burning inside the inlet. This can be seen in figure 5.26, where the temperature contours for different inlet lengths are displayed.
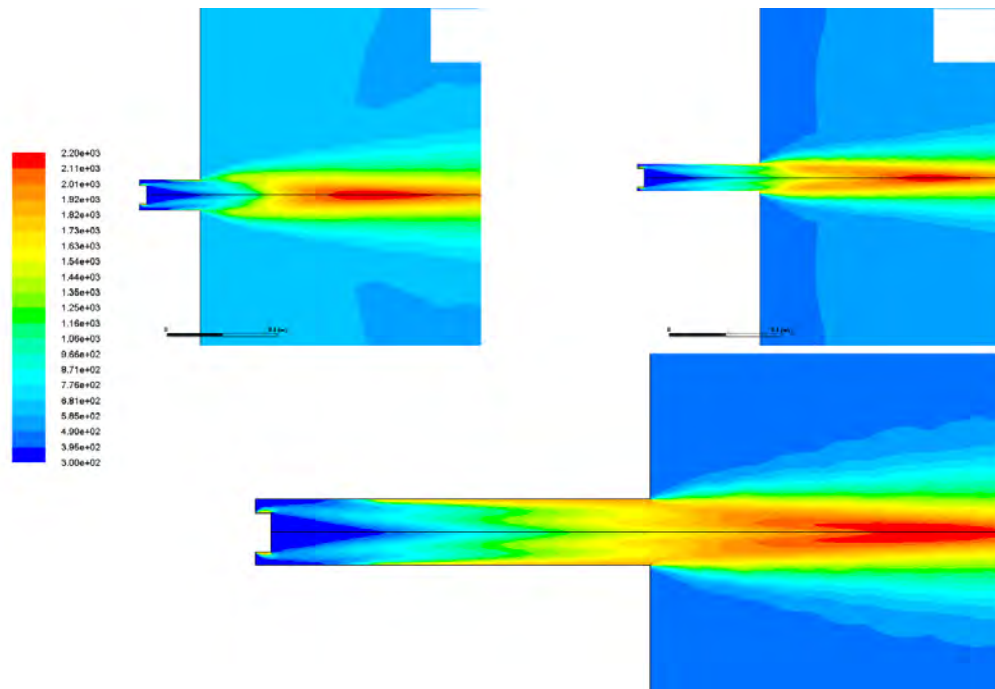

Figure 5.26: Temperature contours for pure iron combustion for different inlet lengths (TL: 50 mm, TR: 100 mm, B: 150 mm)

The temperature profile for these different inlets is displayed in figure 5.27. Another interesting graph is the axial velocity profile, at a set distance after the sudden expansion. The distance is set at 7 mm. This data was used earlier to validate the methane combustion model, in section 4.2 and figure 4.6. These axial velocity profiles can be seen in figure 5.28. In this figure the change of the flame shape for the swirl position of 150 mm can be observed as well.
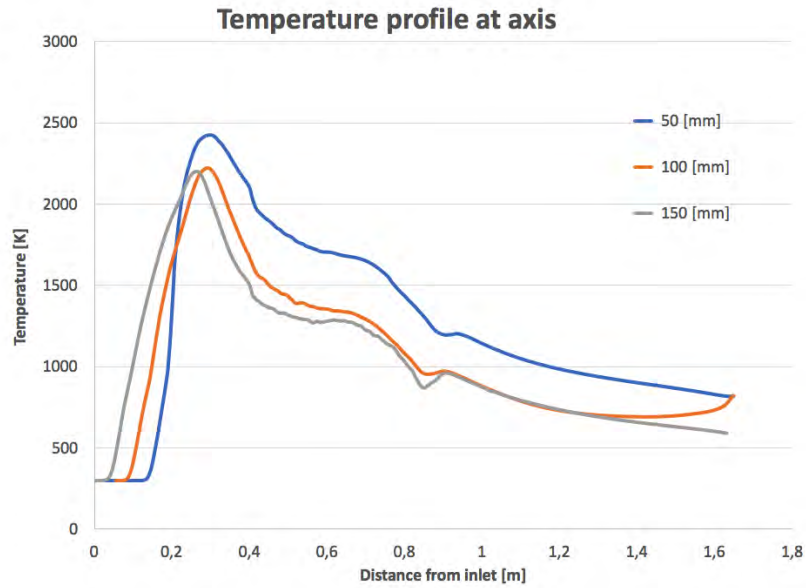
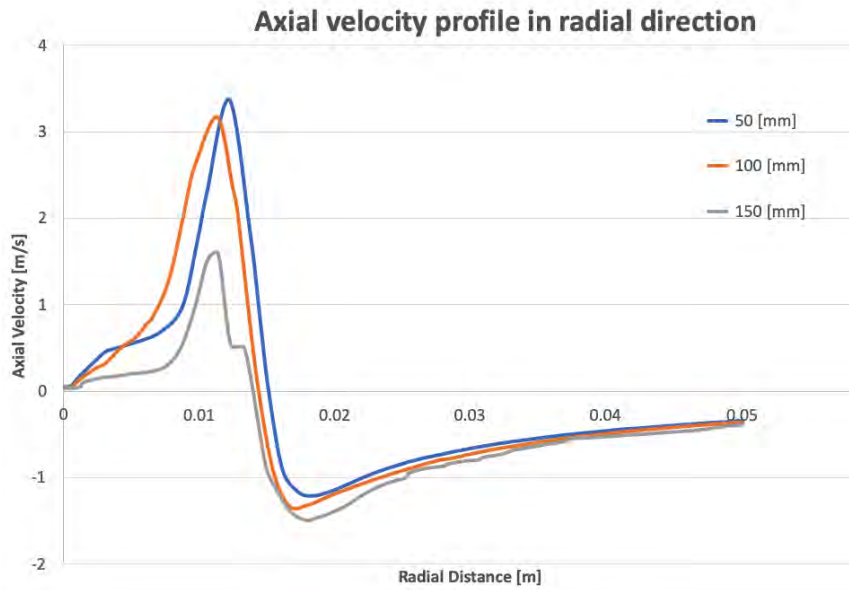Figure 5.27: Temperature profile at the axis for different inlet lengths.

Figure 5.28: Axial velocity profile in radial direction for different inlet lengths.

Chapter 6

Validation of the Iron Combustion Model

In this chapter, advice is given to validate the computational model. First, comparisons with experiments on iron combustion from literature are made, after which methods to validate the model at the experimental setup at the Eindhoven University of Technology are suggested.

6.1 Validation by flame temperature

The first validation is done by comparing the flame temperature of different particle sizes to measurements performed on iron particles: the McGill University in Montreal, Quebec performed experiments in a reduced-gravity environment, and flame temperatures were measured [14]. During these experiments, the flame temperature for the combustion of different sized particles was determined. One of the measured particles has a size of 44.6 [μm (Particle D in [14]), which can be compared to the particle size used in the simulations of chapter 5. The other particles in the experiment had a size of 9.6 [μm (Particle B) and 13.7 [μm (Particle C). Simulations are run with these particle sizes.

The measured flame temperature for the stoichiometric combustion of these particles can be found in table 6.1. When comparing the experimental and computed flame temperature for particle C and D, it can be seen that they match pretty closely. The particle size of 9.7 μm could not be simulated, for the same reasons as for the 5 μm particle in chapter 5. When looking at the experimental flame temperature of this particle, a possible explanation is found for being unable to simulate this particle: the measured temperature is 1820 K. In the model used, and explained in chapter 3, this temperature resides in a crucial part: between the melting temperature of Fe and Fe_3O_4. Further investigation into the model is needed for this region of particle sizes.

Table 6.1: Flame temperature for different particle sizes

Powder	d_p [μm]	T_{flame} measured [K][14]	T_{flame} computed [K]
B	9.6	1820	No Result
C	13.7	2140	2237
D	44.6	2410	2427

6.2 Validation by Combustion Products

Another observation that is made during the reduced-gravity experiments by McGil is that for low oxygen concentrations there is an absence of hematite (Fe_2O_3) [14]. This is also the case for the model: by gradually decrease the amount of oxygen in simulated Low-Swirl Burner, the temperature profile of the particles changes. In the current model it is not possible to see the mass fraction of the different iron species (wüs-, magne- and hematite), but because of the characteristic profile for particle temperature, conclusions can be drawn from here. For low oxygen concentrations, there are no more distinct phase changes or plateaus in the profile after the magnetite profile. This can be seen in figure 6.1. From this figure the conclusion can be drawn that in the simulated flame, for lower oxygen concentrations, there is no hematite produced, which confirms the findings from the experiments. If the oxygen concentration becomes even lower than used in figure 6.1 the profile quenches. This is similar to the findings in section 5.5.4. However, because there are no more distinct features in the temperature profile at these concentrations, it is not possible to determine the composition of generated oxides.
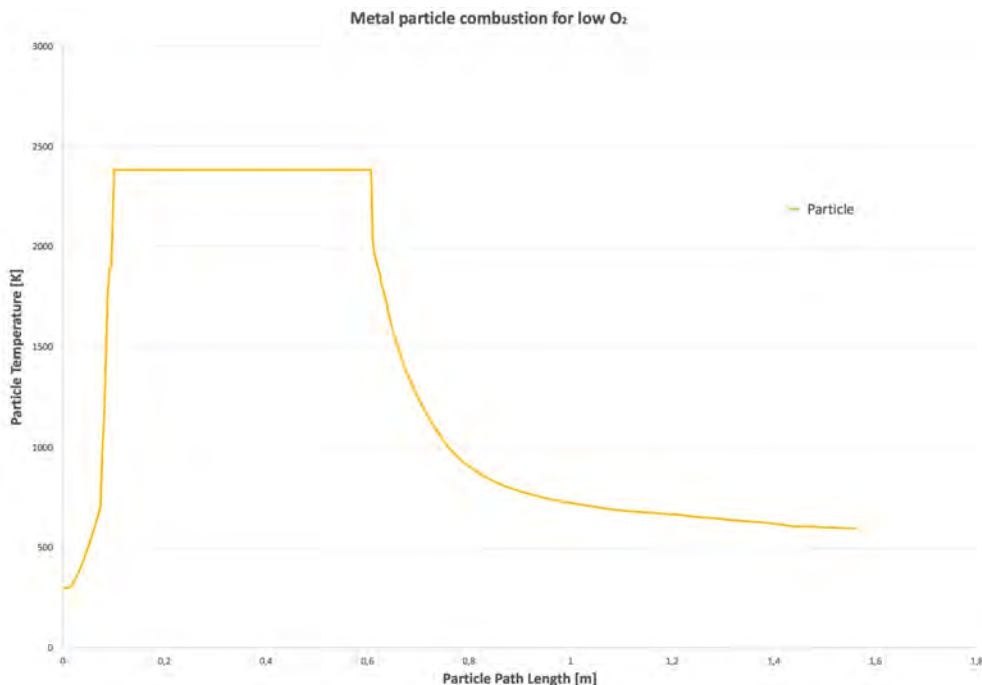

Figure 6.1: Temperature profile for a single particle for low oxygen concentrations.

6.3 Validation by Velocity Profile

In an other experiment, the velocity profiles for a variable swirl number in a low swirl burner are measured.[9] During this experiment, the swirling flame dynamics of a methane flame equipped with an adjustable swirler are measured. The swirler is adjustable by moving the blades, creating a different vane angle. One of the configurations during the experiment was 38^0. This configuration is compared with the LSB TU/e, which has a vane angle of 37^0 (Table 4.2).

The measurements of the axial velocity for this vane angle are compared with the velocity profile obtained from simulations of the stoichiometric combustion of 45 μm iron particles. The shape of the two different velocity profiles can be seen in figure 6.2. The conclusion from this figure that can be drawn is that the general shape of the two profiles is similar. There are, however, to much differences between the two setup to conclude that this validates a part of the model. It does show that it is possible to obtain such a profile from a experimental setup, which can be
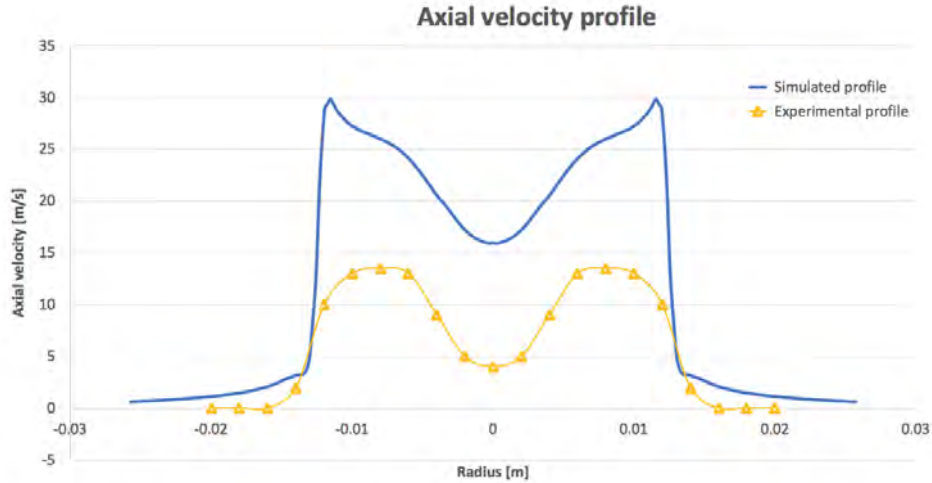
compared with the simulations to validate the model.

Figure 6.2: Axial velocity profile at different radius. (Experimental profile from: figure 3 in [9])

6.4   Advise for Validation

In the previous sections, a few attempts are performed to validate the developed model. Although the results look promising, they are not enough to conclude that the model is validated. A large advantage of this study is that the whole geometry used for the boundary conditions is based upon a real life setup. Therefore, performing a proper validation of the computational model is possible.

To do so, two experiments are proposed: Determining the temperature profile of the flame at the axis, and determining the axial velocity profile at a set distance above the inlet. The temperature profile of the flame could, for example, be measured by using an infrared system [19]. This technique shows good results when comparing the flame temperature profiles with for example a thermo-couple, but is less invasive.

The axial velocity profile at a set distance could be determined with a laser Doppler velocimeter (LDV)[9]. Normally a flow needs to be seeded with, for example, oil droplets. Because there are already particles in the iron flow, this would not be necessary. The exact approach, however, to execute such measurement lies outside the scope of this study.

Chapter 7

Scaling the model

7.1 Scaling

At this point, there is a working model which can be used to create a two-dimensional thermo-dynamic analysis of the combustion of iron powder. The setup modelled, however, generates 4.16 kW for stoichiometric combustion of iron. This is a big difference compared to the 100 kW combustion currently tested in the lighthouse project, and an even bigger difference when compared to for example a coal fired power plant with a capacity of 1000 MW.

One of the advantages of a Low-Swirl Burner is that uniform scaling up of the design is rather easy, when maintaining a constant velocity criterion. The only adjustment that has to be made is scaling the flow number of the burner independently by using a constant residence time criterion [7]. For a premixed burner like the LSB TU/e, the scaling formula for the flow velocity is determined by using the thermal input:

$$U_\infty = \frac{\dot{m}_{air}/\rho_{air} + \dot{m}_{fuel}/\rho_{fuel}}{A} \qquad (7.1)$$

With this formula, the reference flow velocity can be determined by using the mass flows of the fuel and the air combined with the cross sectional area of the burner. All these parameters are known for the LSB TU/e. Once this reference velocity is determined, the burner can be scaled by using the constant velocity criterion: U_∞ has to remain constant. Following this approach the radius of the burner can be scaled to the desired size, by increasing the thermal inputs.

Following this approach, the geometry of the LSB can be scaled up: to generate 100 kW of power, the diameter of the burner has to be 10 cm. This means the geometry of burner has to be scaled up with a factor 4. This can be done easily in Ansys Fluent, by using the scale up function. The design is scaled non-uniform, by defining a scale factor in both the $x-$ and $y-$direction. After scaling the design, a new mesh is generated, on which the same calculations are performed as on the original mesh. To get a feeling what the effect of scaling on the model is, a stepwise approach is taken towards the size of the 100 kW burner: the first scaling factor simulated is 1.5, after which 2.0 and 4.0 are used.

When taking a first look at the different sizes of the domain, the conclusion can be drawn that scaling up the model does not result in a different shaped flame. There are only minor differences when looking at different contours for the four domain sizes. To give a visual representation of these similarities, the familiar temperature profile at the axis is given in figure 7.1, where the length of the axis is normalized (R/R_0).
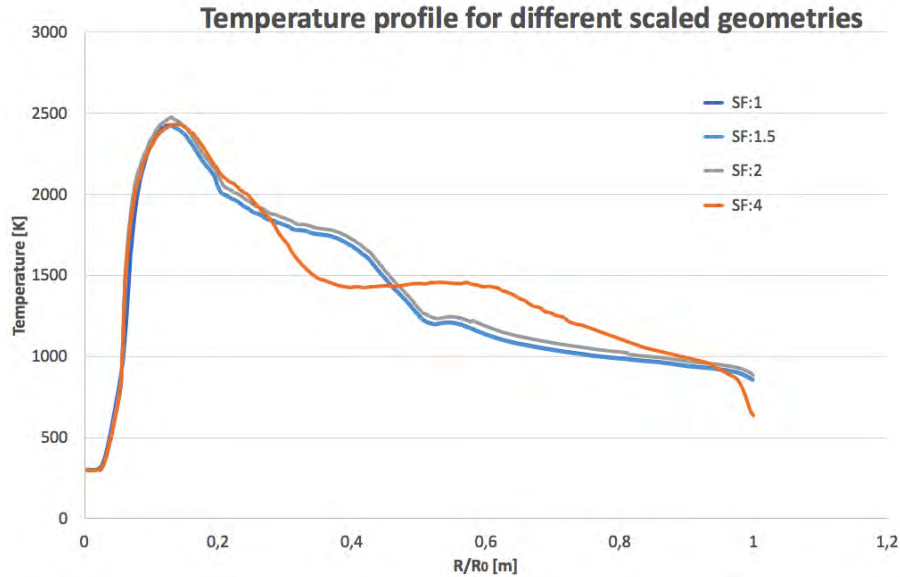
Figure 7.1: Temperature profile for different sizes (scaled) of the geometry.

Scaling towards a diameter of 10 cm posed the first problem during the scaling process: the generated mesh of the setup consisted of 524,480 elements. The limit, however, for the student license of Ansys Fluent, which is used for this study, is 500,000 elements. To be able to perform the simulation, mesh sizing is performed to generate a mesh below the mesh limit. There are some adjustments that can be made to the mesh to stretch this limit: the mesh could be coarser than the current setup, and probably still produce correct results. Also, the outlet area or combustion area is relatively large and could be made smaller. In this way a larger setup could be achieved, but the size is obviously limited. Also, the question is if it is desirable to go even bigger. At these mesh sizes not only the student license is a limiting factor, the available computational power is not sufficient to perform these kind of simulations.

7.2   Towards 1 GW

Potentially, with more computational power, a two-dimensional analysis could be made for, for example, a coal fired power plant with a capacity of 1100 MW. Of course there are a lot of steps that have to be taken before this is realistic. When modeling a combustion system from this size, a lot more parameters have to be taken in account then the ones that can be determined with the current model. For example, particle size is constant in the model. In real life, particles will grow in size when they oxidize. Another function missing in the model is determining the exact composition of the reaction product. In a power plant, the shape, weight and composition of the reaction products are essential parameters, as the combustion chamber is only a small part of the complete installation.

However, when focussing on the combustion chamber only, the model already ticks a lot of the necessary boxes. Especially when looking at the way combustors of this size are modelled currently. These, so-called, furnace models do not model individual particles in the entire combustion chamber. Calculations would become too complex and requires immens amount of computational power. Instead, a segmental approach is suggested, which is already described in figure 3.1

To use such a furnace model, the behavior of the particles under different combustion conditions should be known. Performing experiments for all different conditions is a near impossible task, but becomes a credible option with a validated particle model. If the iron particle combus-

tion is properly validated by performing experiments, and extended to incorporate more material parameters, it could function as a base for simulations on the *GW*-scale.

7.2.1 Towards 100 *kW*

As described, the steps towards *GW*-sized models are still big ones. On a shorter timescale however, and with less adjustment needed, the model could be used to model for example the 100 *kW* installation TEAM SOLID is building and testing at the time of writing [23]. When the model is properly validated on the experimental setup of the Low-Swirl Burner, a next step could be to model the burner in the installation of TEAM SOLID, which should be fully functional by then. This would be a next step in the validation of the model, and the next step towards simulating iron combustion on the scale where it can amount for a significant amount of the global energy demand.

Chapter 8

Three-Dimensional

To further investigate the possibilities of the model, some first attempts are made to use the model in a three-dimensional geometry. The first results look promising, but the computational limits of the hardware used in this study were reached quickly. Also, it is worth considering if it necessary to model the combustion of iron in three instead of two dimensions, and what the added value of the extra dimension would be. Currently, there is a lot of research in the field of iron combustion that still needs to be done, which could very well be performed in two-dimensional analysis. Nevertheless, some results are summarized shortly in the sections below.

8.1   Three-Dimensional Drop-Tube

The first three dimensional analysis of the model is performed by Martin Schiemann et al., in which a drop tube simulation is performed. The geometry of this drop tube is relatively simple, and similar to the geometry of the 2 dimensional drop tube in section 3.6: a diameter of 25 cm and a length of 1,5 m. The temperature in the drop tube is uniform at 900 K, and the particle size is 50 μm. The result of this simulation is a particle temperature profile identical to the simulation performed on the two dimensional drop tube. Therefore, a first conclusion is drawn that the model works on both two- and three-dimensional geometries.

8.2   Three-Dimensional Low-Swirl Burner

Next, an attempt is made on simulating the LSB from this study in a three-dimensional analysis. Similar problems as in previous chapters where encountered: due to the fact that the design of the swirler is quite complex, it is difficult to create a mesh that does not exceed the element limit of the Ansys Fluent Student License. In order to achieve a mesh below this limit, which still has an acceptable accuracy, the design is simplified: instead of an expansion, the swirler is modelled inside an enclosed tube. This immediately eliminates the option to compare the two- and three-dimensional models. However, it is still valuable to see if the model works in such an environment.

Cold flow simulations on this geometry can be performed without problems, as well as a reacting flow without the iron particle model enabled. When enabling the iron model, and letting it interact with the continuous phase of the flow, again a hardware limit is encountered: after a few iterations the computer runs out of memory. Again a concession is made and the interaction with the continuous flow is disabled. This means the particles can react and combust, but the heat generated during this combustion is not transferred to the fluid domain. In this case this means that the temperature of the fluid domain remains constant at 900 K.

The result is a rudimental simplified model, but the particles model does function: the iron particles heat up, undergo phase changes and cool down again. The particles tracks colored by velocity and by temperature can be found in the figures 8.1 and 8.2 below. From these first steps the conclusion is drawn that in theory the model lends itself for three dimensional simulations. To transfer from theory to practice, however, a lot of steps still need to be taken. As mentioned earlier, the question remains if it is currently useful to invest a lot of time and resources in a three-dimensional model, when there are still a lot of steps that can be taken with two-dimensional analysis.
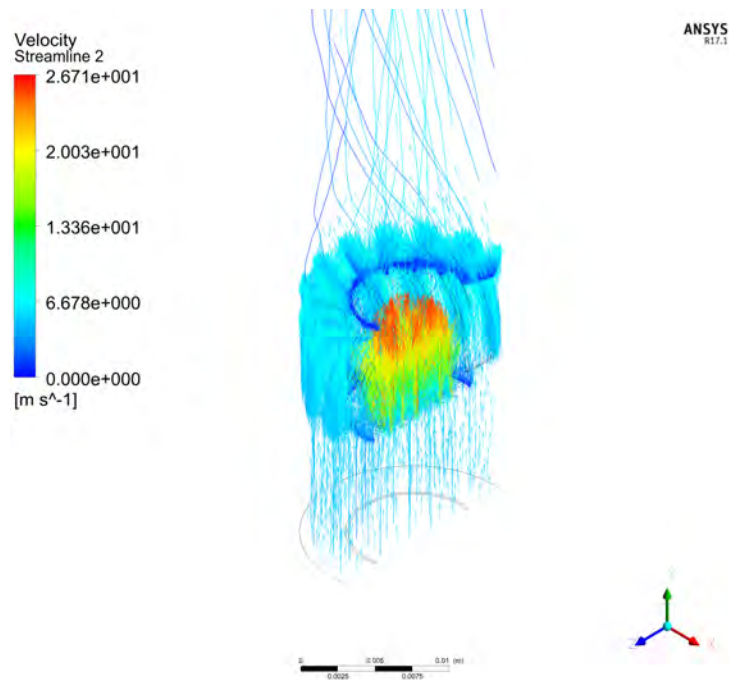
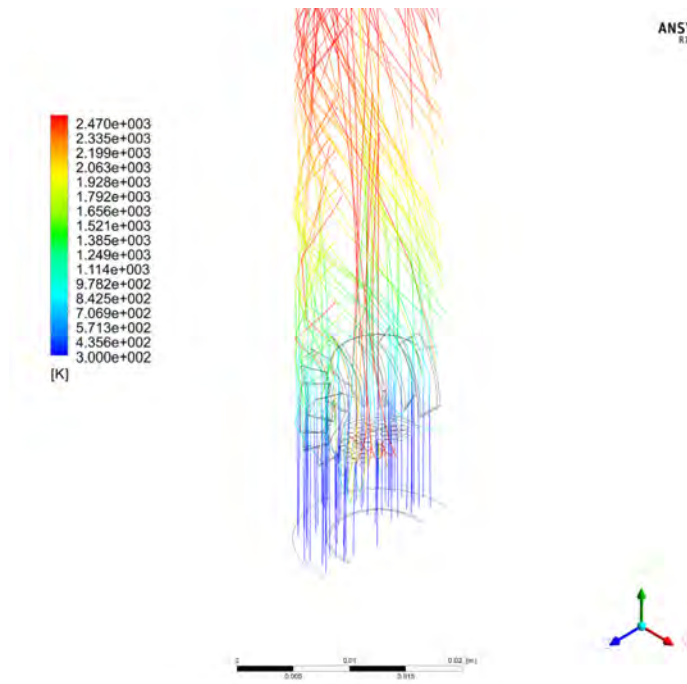Figure 8.1: Velocity tracks for the three-dimensional simulations.

Figure 8.2: Temperature tracks for the three-dimensional simulations.

Chapter 9

Conclusions

In this chapter, recommendations are given on how to proceed with the development of the iron particle combustion model. Afterwards, the conclusions that are drawn from this study are given.

9.1 Recommendations

The recommendations can be divided into three main topics: recommendations on improvements on the model, recommendations for the validation of the model and proposed steps forward.

9.1.1 Improvements of the model

One of the steps which are currently being undertaken for improving the model is introducing an Arrhenius-reaction instead of an ignition point, which is currently the first step in the model. Using an ignition point is a simplification: iron oxidizes at every temperature, but the reaction rate is different.

Another useful addition to the model is plotting or printing the mass fractions of the different iron oxides. All mass fractions are calculated, but currently, it is not possible to see how the reaction products are built up.

The last addition is changing or adding different materials than iron to the model. A version with lithium has already been investigated. Of course the combustion modes of the different metal fuels are different, but if the particle model for iron is fully developed, it can serve as an excellent framework to create models for other materials.

9.1.2 Validation of the model

The iron combustion model is validated partly by comparing the results of the simulations with experiments from literature. The similarities between these two components lead to the tentative conclusion that the model is a correct representation of actual iron combustion. Iron combustion remains, however, an extremely complex process, and the complete understanding of the process is still a long way away.

However, after this study, an opportunity presents itself to take a big step forward in the field of numerical simulation of iron particle combustion. The computational domain of this study is based upon an active, real-life experimental setup, which means the results that are obtained by simulation can be validated by performing experiments on said setup. From this validation there are two approaches that can, or need, to be followed: the model is either validated and can be scaled up towards bigger and more powerful combustion systems, or the model can not be validated correctly, and improvements must be made on the model. Either way, the next step should

be performing experiments that are in line with the performed simulations.

Two different experiments are proposed: determining the temperature profile in the flame, for example at the axis, or determining the velocity profile at a set distance from the inlet. Techniques proposed are LDV or infrared measurements, but the topic has not been investigated thoroughly enough to state that these are the best techniques or even the optimal parameters to determine during experiments.

9.1.3 Proposed steps forward

The proposed steps forward after this study have already been touched upon briefly in the previous section but can be summarized by a timeline, which is pictured in figure 9.1 below. A few small adjustments are suggested for the model, after which the model needs to be validated by experiments. This will either lead to proceeding to the next step or taking a step back and improve the model again.

The step after correctly validating the model is scaling up the simulations: take the step from a Low-Swirl Burner to a more significant, more powerful combustion installation. After successfully modelling such an installation, the process returns to validating the results by experiments. Again the same procedure applies: validation or back to improving the model. By following this approach, step-by-step the ultimate goal is reached: being able to model a GW combustion chamber, (partly) fueled by metal fuels.
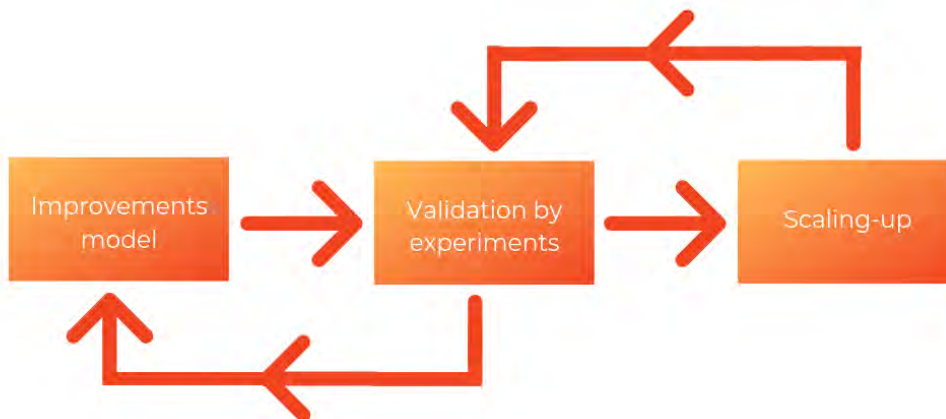

Figure 9.1: Proposed approach for future study.

9.2 Conclusions

The title of this graduation report is: 'Creating a numerical model for burning metal fuels in industrial size burners'. This main question, or task, cannot be answered with a simple yes or no, and the first conclusion is that the main question is only answered partly: after finishing this study, there is no simple, easy-to-use, numerical simulation which can be used to simulate the combustion of metal powered fuels in an industrial-sized combustion system. However, the first steps are taken successfully towards this goal, and a roadmap to achieve such a numerical

simulation is proposed.

When looking at the sub-questions of this study, the first two questions can be answered relatively easy. The options for existing models to simulate the combustion of metal fuels are limited, and the models that do exist are all rudimental. This leads to the answer to the second question: is it better to alter existing models or to build one from scratch? In the opinion of the author altering an existing model is preferred. Because most models are rudimental, improving these models will lead to quicker steps forward compared to starting from scratch. Combining this with the current timeline of the development of the combustion of metal fuels makes having a model that can correctly predict combustion behaviour, even if it is rudimental, extremely valuable.

The last two subquestions are answered partly. Although the boundary conditions are not given for an industrial-sized burner, boundary conditions are defined for a smaller burner. When scaling up the model, some boundary conditions may change, but the vast majority of the conditions will remain the same. The similarities between a 100 kW and an 1 GW burner have not been investigated. The reasoning behind this is that there are still many steps between 10^2 and 10^9 W, and the model currently is not suited for the larger scale. A way to achieve such a model, however, is proposed: using a segmental, one-dimensional approach. If the particle model can provide an accurate list of combustion parameters for different conditions, a database can be built which can be used to create a simplified, segmented version of an 1100 MW combustor. All reactions would be calculated in such a segment, and only combustion product would move on into the next segment, after which the process repeats itself.

In this study, after investigating different options for modelling iron combustion, the decision is to focus on an existing User-Defined Function (UDF), improve this UDF, use it to perform simulations and take the next step in numerically simulating metal combustion. The software used to execute the UDF is ANSYS Fluent. The combustion of iron particles is discussed briefly, after which the different steps and assumptions that make up the model are explained and exemplified. The UDF is based upon a diffusion-limited approach, where different temperatures for heating, ignition and phase changes are defined.

Because of the availability of an experimental Low Swirl, or Weak Swirl, Burner (LSB), the decision is made to focus on this type of burners. First, to get acquainted with modelling such a burner, a methane low swirl burner that is experimented on extensively, and has similar geometry and boundary conditions as the available burner, is recreated in a two-dimensional numerical simulation.

After validation of this burner, the available low swirl burner is recreated following the same approach, using methane as a fuel. After successfully creating this setup, the transition is made from methane combustion towards iron combustion. Following a step-wise approach, first the amount of iron in the fuel is increased, and finally, the amount of methane is decreased.

Different conclusions can be drawn from the simulations. The first conclusion is that it is possible to simulate an iron fueled flame on an LSB, which shows many similarities with other experiments and therefore can be partly validated. When adding iron particles to the fully converged methane flame and letting them react inertly, they follow the flow profile inside the burner and heat up as expected. Different heating times can be seen when compared to, for example, coal particles, and when comparing different iron particle sizes.

When looking at particle sizes, the model starts to behave inappropriately when the particle size drops below 5 μm. Further investigation is needed to conclude if this is due to an error, or lacking function in the model, or due to the difficulty combusting anything this size at these conditions: at the time of writing a stable flame with these particles is not obtained on the experimental setup. Combusting 45 μm particles does lead to a stable solution, and because of the availability

of these particles at the experimental setup, most calculations are performed with these particles

When adding these particles to the lean methane flame, an increase in the flame temperature is observed. The increase in temperature matches the expected increase, compared to the heating values and energy density of iron particles. Also, an upper limit is encountered for the amount of iron that can be added to the methane flame: at some point, oxygen depletion quenches the flame and stops the combustion of iron.

To investigated scaling, adjustments to the geometry are made in the computational domain that can also be made on the experimental setup: the length of the expansion tube of the LSB can be varied. In the literature it is found that the optimal length for the expansion tube lies between one and three times the diameter of the tube. The simulations performed confirm this theory. This means that from the different positions on the experimental setup, two, four and six times the diameter, only the first position is suitable.

To conclude this graduation report, there is still a long way to go, and there are many problems that still need to be tackled before a validated, simple model for the combustion of metal combustion becomes a reality. Hopefully, the research done in this study will contribute towards this model and will make the steps that need to be taken more clear and easy.

Bibliography

[1] Ice Index dutch power baseload futures. `https://www.theice.com/products/27993085/Dutch-Power-Baseload-Futures/data?marketId=2920196`. Accessed: 07-06-2018. 2

[2] Tennet actual information of the load (demand of electricity) in the netherlands. `https://www.tennet.eu/nl/elektriciteitsmarkt/data-dashboard/belasting/`. Accessed: 07-06-2018. 3

[3] Fernando Maria. Amman and Richard. Wilson. Ettore majorana international science series, physical sciences ; 9; ettore majorana international science series. 9. physical sciences ;. 1981. 2

[4] DB Beach, BG Sumpter SD Labinov, and AJ Rondinone RK Richards. Solid-statecombustion of metallic nanoparticles: new possibilities for an alternativeenergy carrier. *J Energy Resour Technol*, 192:29–32, 2007. 1

[5] David Beerer. Flashback and turbulent flame speed measurements in a hydrogen and methane fired low-swirl injector at elevated pressures and temperatures. Master's thesis, University of California, Irvine, 5 2013. ix, xi, 21, 22, 23, 29

[6] J.M. Bergthorson, S. Goroshin, M.J. Soo, P. Julien, J. Palecka, D.L. Frost, and D.J. Jarvis. Direct combustion of recyclable metal fuels for zero-carbon heat and power. *Applied Energy*, 160:368 – 382, 2015. 1, 2

[7] R. K. Cheng, D. T. Yegian, M. M. Miyasato, G. S. Samuelsen, C. E. Benson, R. Pellizzari, and P. Loftus. Scaling and development of low-swirl burners for low-emission furnaces and boilers. 28(1):1305–1313, 2000. 59

[8] L.A.C. Dirven. Shipping solar energy with metal fuels. Master's thesis, Eindhoven University of Technology, Amsterdam, 8 2017. 2

[9] Daniel Durox, Jonas P. Moeck, Jean-François Bourgouin, Pascal Morenton, Marc Viallon, Thierry Schuller, and Sébastien Candel. Flame dynamics of a variable swirl number system and instability control. 160(9):1729–1742, 2013. 56, 57

[10] S.H. Fischer and M.C. Grubelich. Theoretical energy release of thermites, intermetallics, and combustible metals. 6 1998. 1

[11] Irvin Glassman. Solid propellant rocket research. 10

[12] Irvin Glassman, Richard A. Yetter, and Nick Glumac. Combustion, chapter 9. 2014. 10, 11

[13] Jeanette Gorewoda, Martin Schiemann, Viktor Scherer, and Markus Neuroth. An examination on the influence of the oxidation state of iron on the spectral radiative emittance of synthetic ash layers. 06 2015. 14

[14] Samuel Goroshin, Francois-David Tang, Andrew J. Higgins, and John H.S Lee. Laminar dust flames in a reduced-gravity environment. *Acta Astronautica*, 68(7):656 – 666, 2011. 50, 55, 56

[15] Thijs Hazenberg. An eulerian-lagrangian approach for simulating heterogeneous combustion of metal fuels. Master's thesis, Eindhoven University of Technology, Eindhoven, 9 2019. 7

[16] Ansys Inc. *ANSYS FLUENT 16.0/16.1 Documentation.* Ansys Inc. software. 8

[17] Mark Z. Jacobson. Review of solutions to global warming, air pollution, and energy security. *Energy Environ. Sci.*, 2:148–173, 2009. 1

[18] Mark Z. Jacobson and Mark A. Delucchi. Providing all global energy with wind, water, and solar power, part i: Technologies, energy resources, quantities and areas of infrastructure, and materials. *Energy Policy*, 39(3):1154 – 1169, 2011. 1

[19] Jir-Ming and Char Jun-Hsien. The measurement of open propane flame temperature using infrared technique. 56(1):133–144, 1996. 57

[20] Rastko Jovanović, Bartosz Swiatkowski, Slawomir Kakietek, Predrag Škobalj, Ivan Lazović, and Dejan Cvetinović. Mathematical modelling of swirl oxy-fuel burner flame characteristics. 191:193–207, 2019. 36

[21] Cheng R. K. Velocity and scalar characteristics of premixed turbulent flames stabilized by weak swirl. 101, 1995. 52

[22] Cheng R. K., Littlejohn D., Nazeer W. A., and Smith K. O. Laboratory studies of the flow field characteristics of low-swirl injectors for adaptation to fuel-flexible turbines. 130(2), 2008. 22

[23] Jelle Krekels. Swinkels family brewery gaat metaalpoeder gebruiken als duurzame brandstof, samenwerking met studententeam solid van tu/e. `http://...`, 2019. 3, 61

[24] J.J.J. Krens. Internship report. August 2018. 3

[25] Soo M, Goroshin S, Bergthorson JM, and Frost DL. Reaction of a particle suspension in a rapidly-heated oxidizing gas. *Propellants, Explos Pyrotech 2015*, 40:604 – 612, 2015. 13

[26] G. Maggio and G. Cacciola. When will oil, natural gas, and coal peak? *Fuel*, 98:111 – 123, 2012. 1

[27] Jeffrey M. Bergthorson Martin Schiemann and V. Scherer. Iron particles as carbon-neutral fuel in spray roasting reactors. *The 43rd international technical conference on clean energy*, 2018. 8, 11, 12, 13

[28] Dimitri Mignard and Colin Pritchard. A review of the sponge iron process for the storage and transmission of remotely generated marine energy. *International Journal of Hydrogen Energy*, 32(18):5039 – 5049, 2007. 1

[29] Toshihiko Nakata, Diego Silva, and Mikhail Rodionov. Application of energy system models for designing a low-carbon society. *Progress in Energy and Combustion Science*, 37(4):462 – 502, 2011. 1

[30] NIST. Janaf thermochemical tables. *Phys, Chem. Ref. Data*, 1995. 11, 14, 15

[31] Rolf D. Reitz. Directions in internal combustion engine research. *Combustion and Flame*, 160(1):1 – 8, 2013. 1

[32] Cornell RM and Schwertmann U. The iron oxides. *Weinheim: VCH*, 1996. 13

[33] E.I. Shkolnikov, A.Z. Zhuk, and M.S. Vlaskin. Aluminum as energy carrier: Feasibility analysis and current technologies overview. *Renewable and Sustainable Energy Reviews*, 15(9):4611 – 4623, 2011. 1

[34] L. Somers. The simulation of flat flames with detailed and reduced chemical models. *Reliability Engineering and System Safety*, january 1994. 7

[35] Conway J.B Von Grosse H. *Ind, Eng. Chem.*, 1958. 11

[36] Dongsheng Wen. Nanofuel as a potential secondary energy carrier. *Energy Environ. Sci.*, 3:591–600, 2010. 1

[37] T. Yabe, S. Uchida, K. Ikuta, K. Yoshida, C. Baasandash, M. S. Mohamed, Y. Sakurai, Y. Ogata, M. Tuji, Y. Mori, Y. Satoh, T. Ohkubo, M. Murahara, A. Ikesue, M. Nakatsuka, T. Saiki, S. Motokoshi, and C. Yamanaka. Demonstrated fossil-fuel-free energy cycle using magnesium and laser. *Applied Physics Letters*, 89(26):261107, 2006. 1

Appendix A

Appendix

TU/e Technische Universiteit
Eindhoven
University of Technology

**Declaration concerning the TU/e Code of Scientific Conduct
for the Master's thesis**

I have read the TU/e Code of Scientific Conduct[1]

I hereby declare that my Master's thesis has been carried out in accordance with the rules of the TU/e Code of Scientific Conduct

Date
10-08-2019

Name
Jip Jan Jacob Keurs

ID-number
0677239

Signature

Submit the signed declaration to the student administration of your department

Appendix B

Low Swirl Burner Eindhoven University of Technology Methane Combustion

The modeling conditions for pure methane combustion in the LSB at the Eindhoven University of Technology are summarized in tabel B.1. The mesh that is used can be seen in the figure below. After the table a variety of figures with different results can be found.
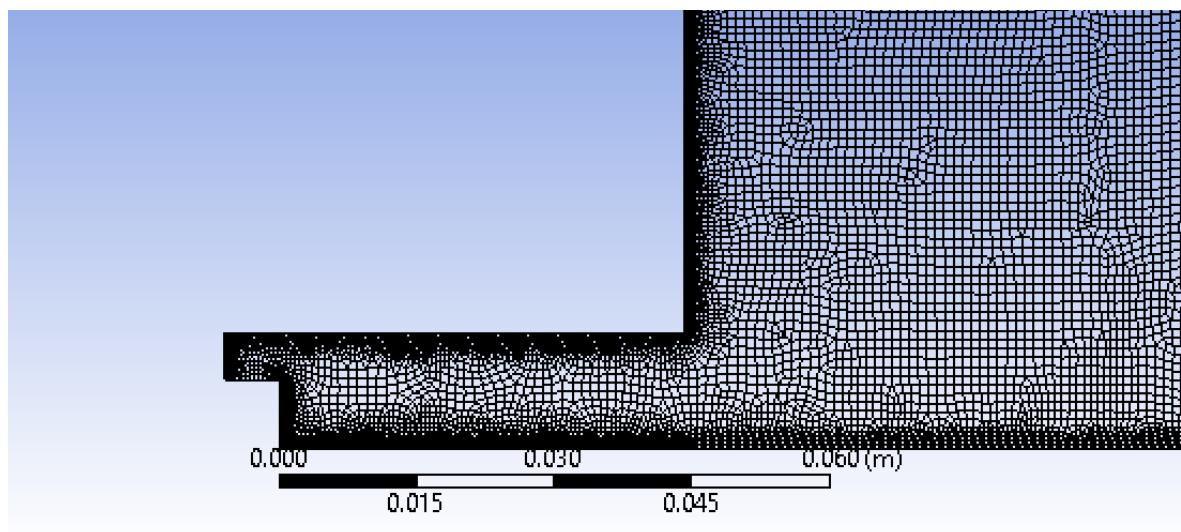
Figure B.1: Mesh used in simulations

Table B.1: Modelling conditions.

| General	
Time	Steady
Dimension	2D
Symmetry	Axisymmetry
Materials	
Mixture	Methane Air 2-Step
Fluid	Air
Density	Ideal Gas
Solution methods	
Scheme	SIMPLE
Discretisation	Second Order Upwind
Solver	Pressure-Velocity Coupling
Models	
Energy	On
Turbulence	$\kappa - \epsilon$ model, Enhanced Wall Treatment
Species Transport	Volumetric Eddy-Dissipation
Boundary Conditions	
Inlet	Mass-flow-Inlet
Outlet	Pressure-outlet
Walls	Constant Heat Flux / Adiabatic
Flow domain	No b.c. prescribed (Free flow)
Geometry	
Width of domain	1550 [mm]
Height of domain	300 [mm]
Minimum element size	$1e^{-5}$[m]
Maximum element size	$5e^{-4}$[m]
Number of mesh elements	74,464
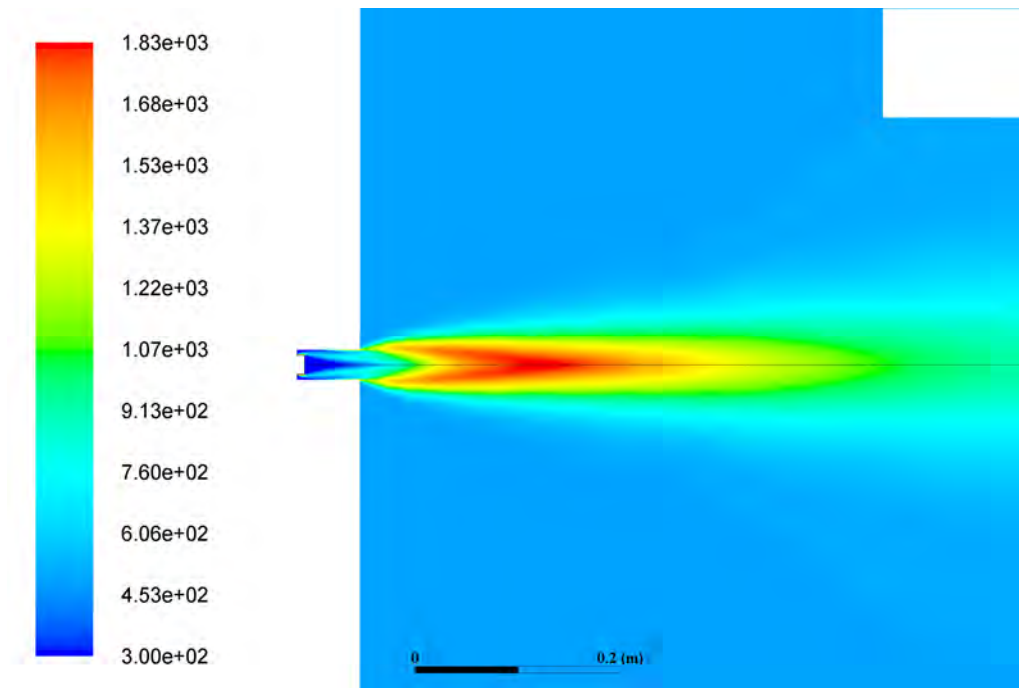
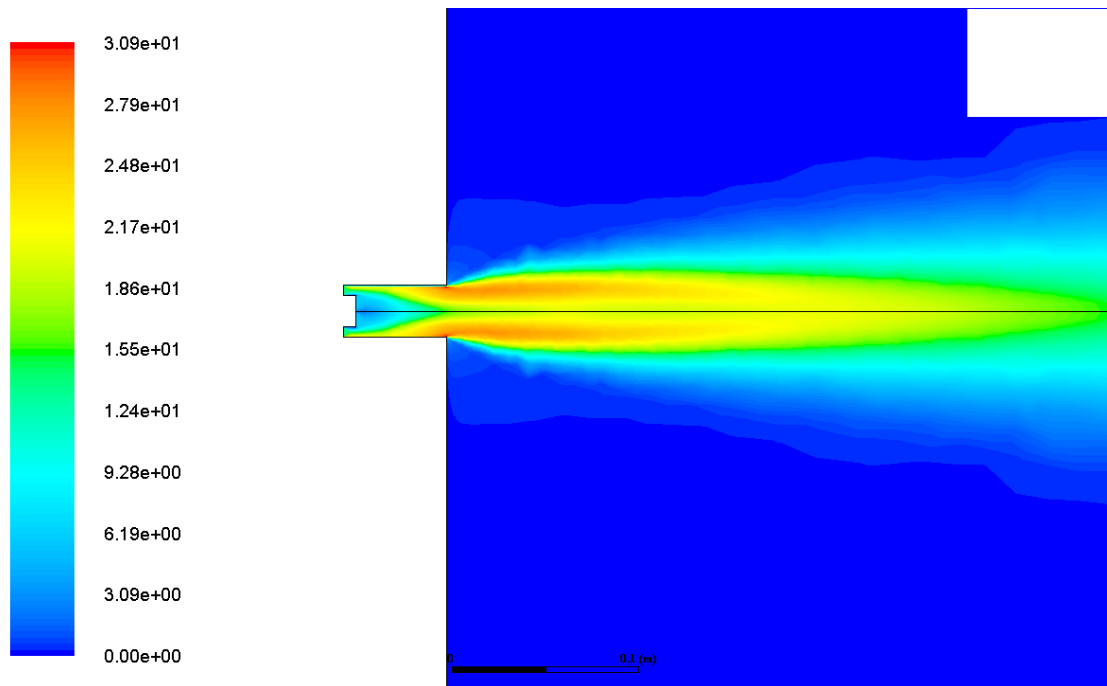Figure B.2: Temperature contours in Kelvin K.
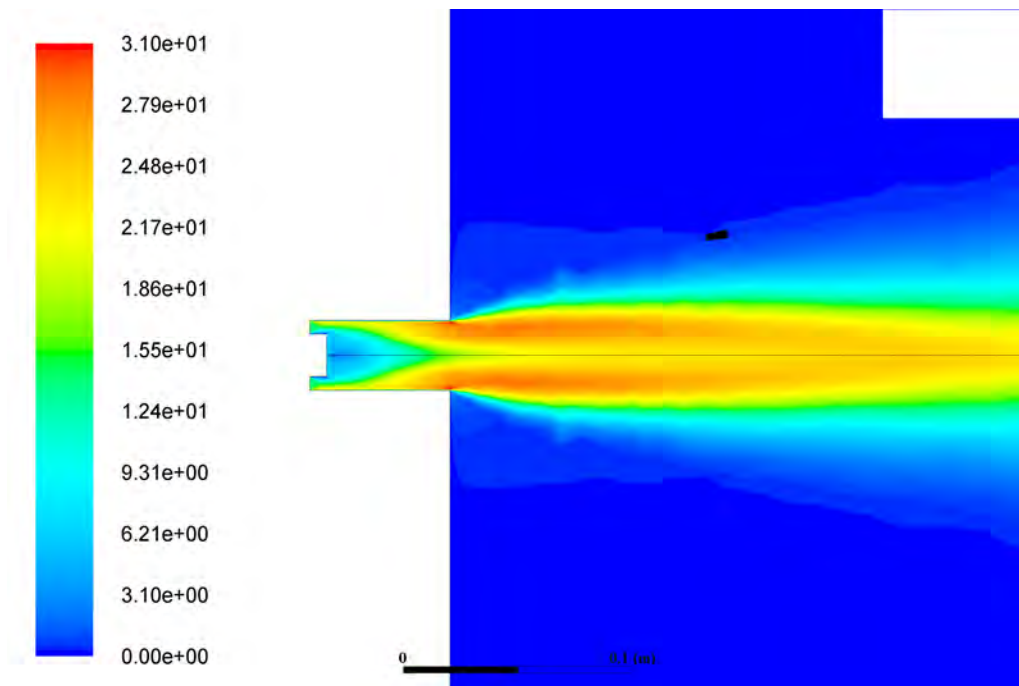
Figure B.3: Velocity contours in meters per second m/s.
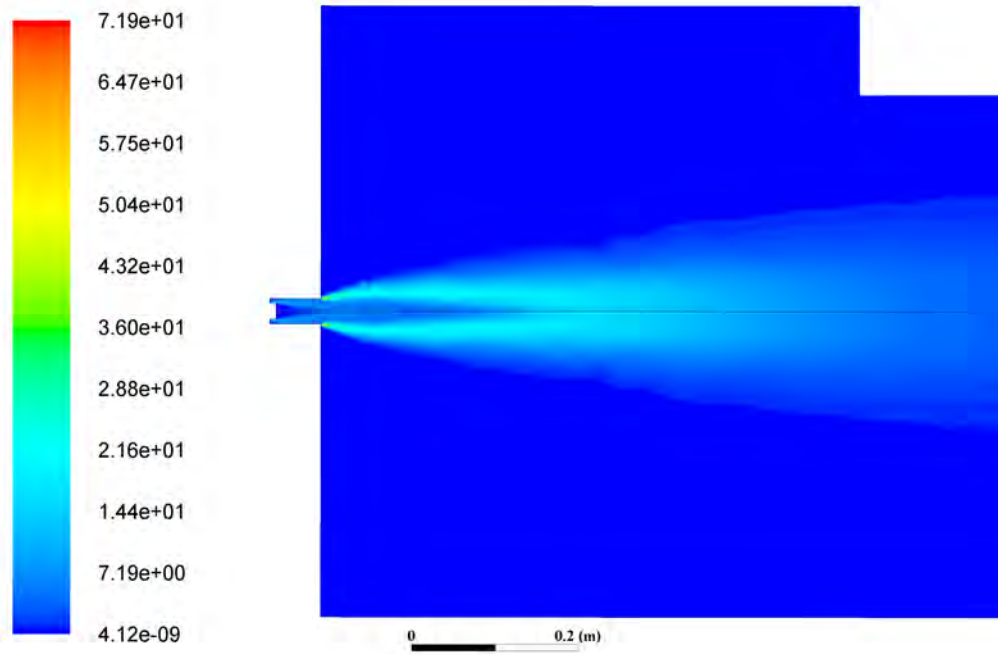
Figure B.4: Turbulent kinetic energy contours m^2/s^2.
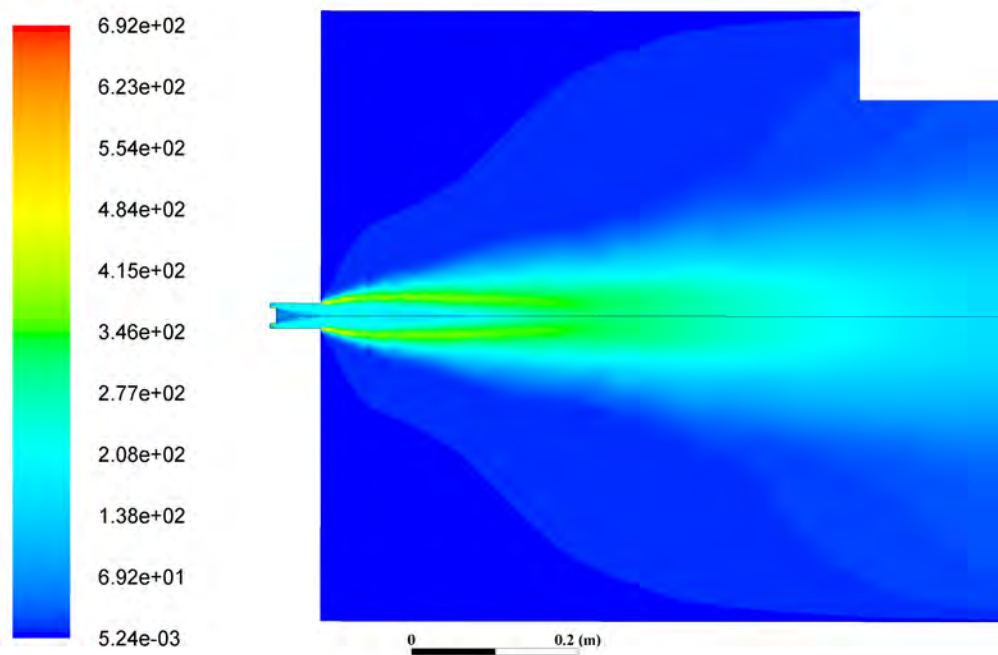
Figure B.5: Turbulent intensity contours %.
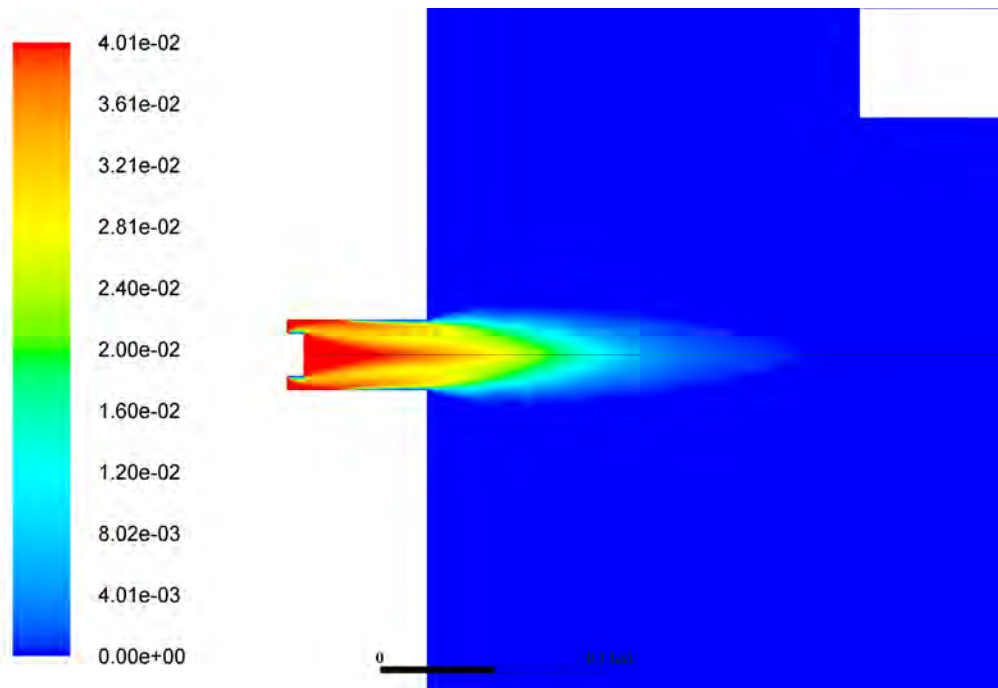
Figure B.6: Mass fraction CH_4 contours.
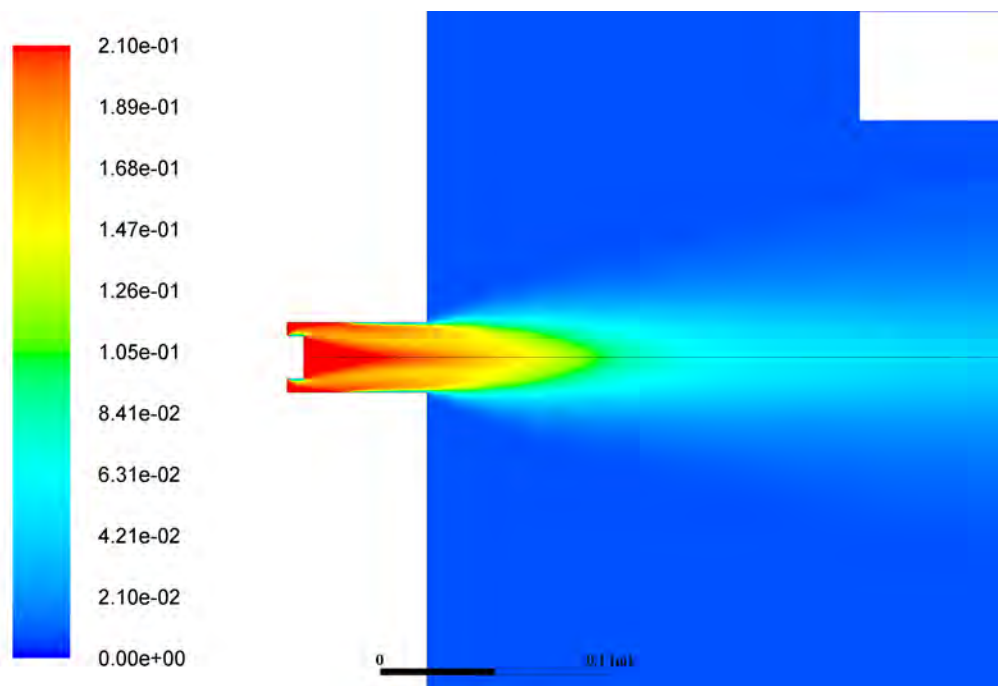
Figure B.7: Mass fraction O_2 contours.
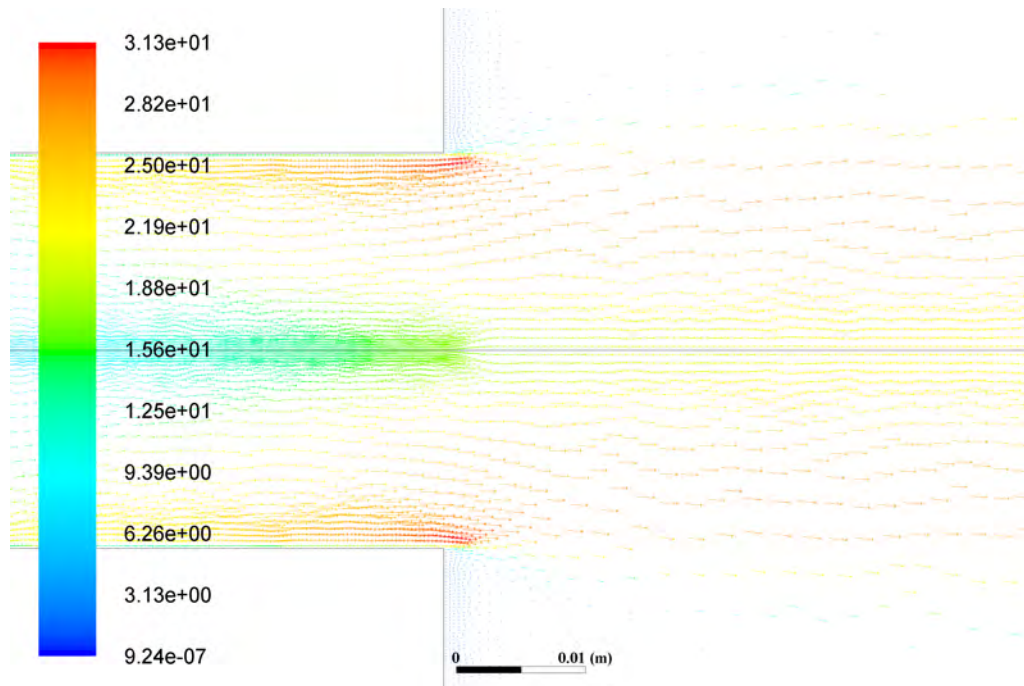
Figure B.8: Velocity vectors in meters per second m/s.
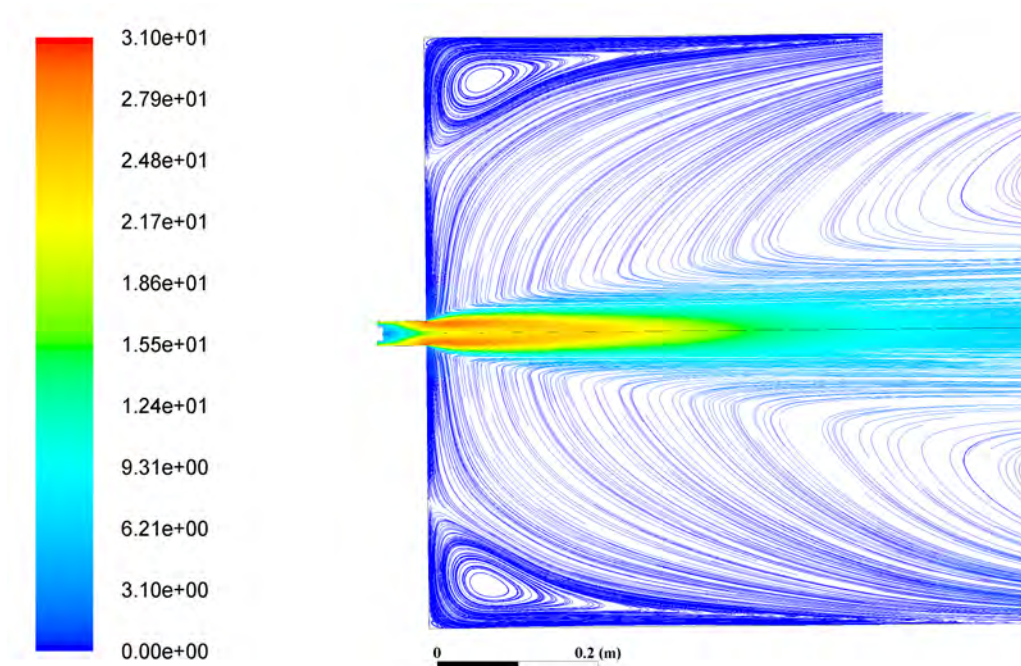
Figure B.9: Velocity pathlines in meters per second m/s.

Appendix C

Low Swirl Burner Eindhoven University of Technology Iron Combustion

In this appendix, a variety of figures can be found that are obtained by modeling the stoichiometric combustion of iron with air.
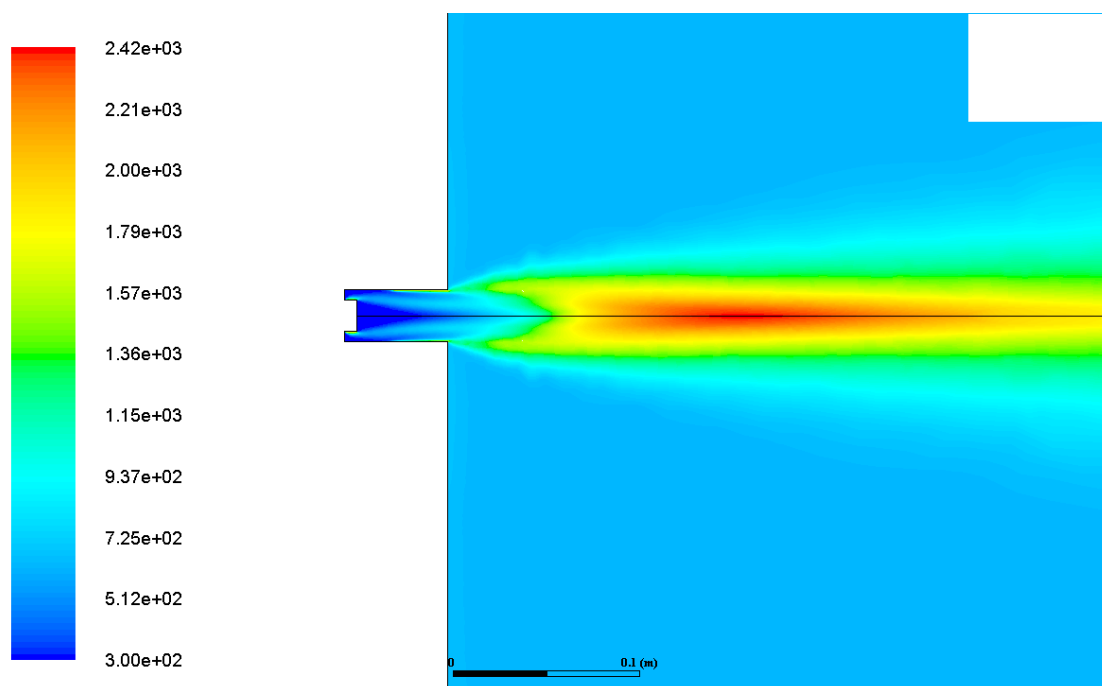
Figure C.1: Temperature contours in Kelvin K.

Figure C.2: Velocity contours in meters per second m/s.
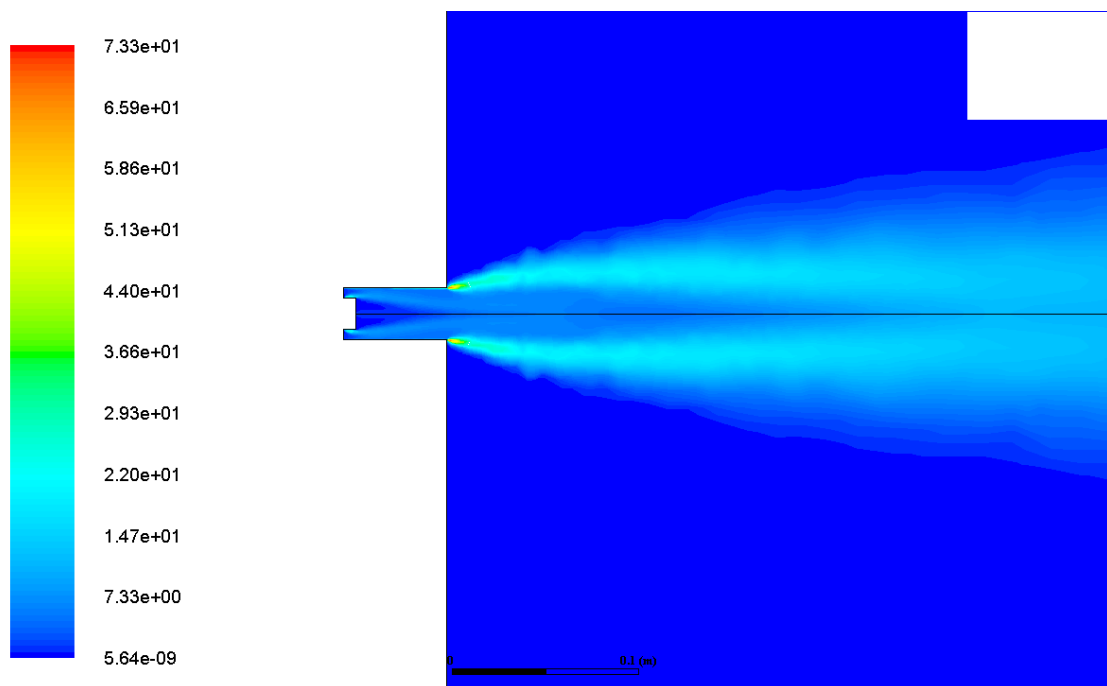
Figure C.3: Turbulent kinetic energy contours m^2/s^2.
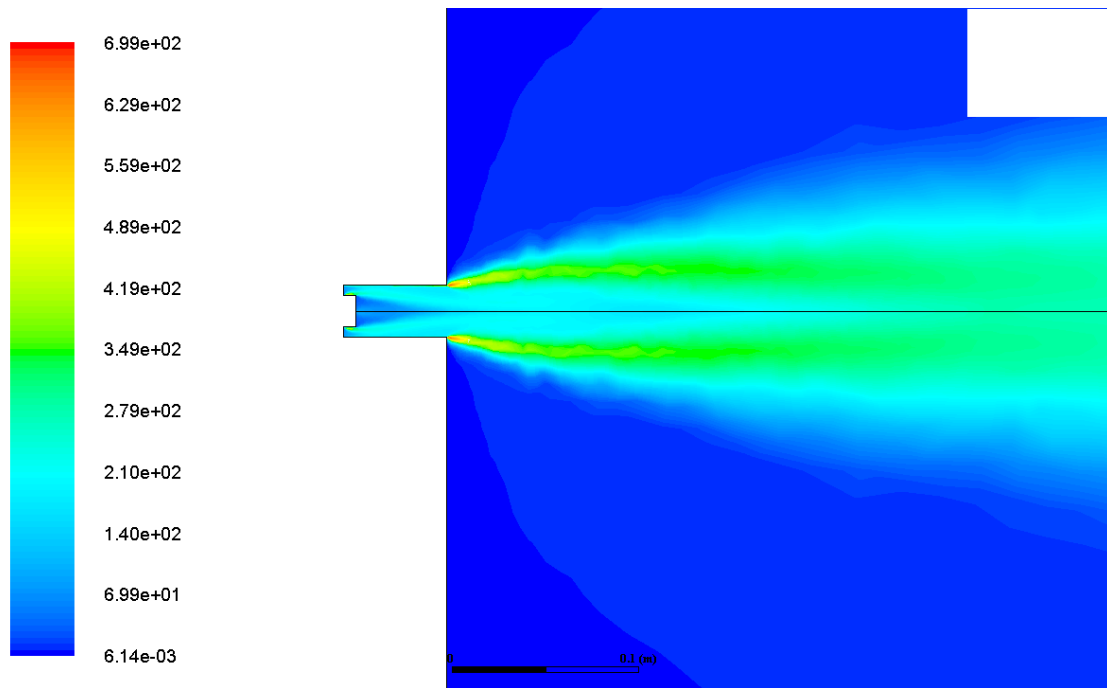
Figure C.4: Turbulent intensity contours %.

Appendix D

Unscaled figures of methane and iron combustion
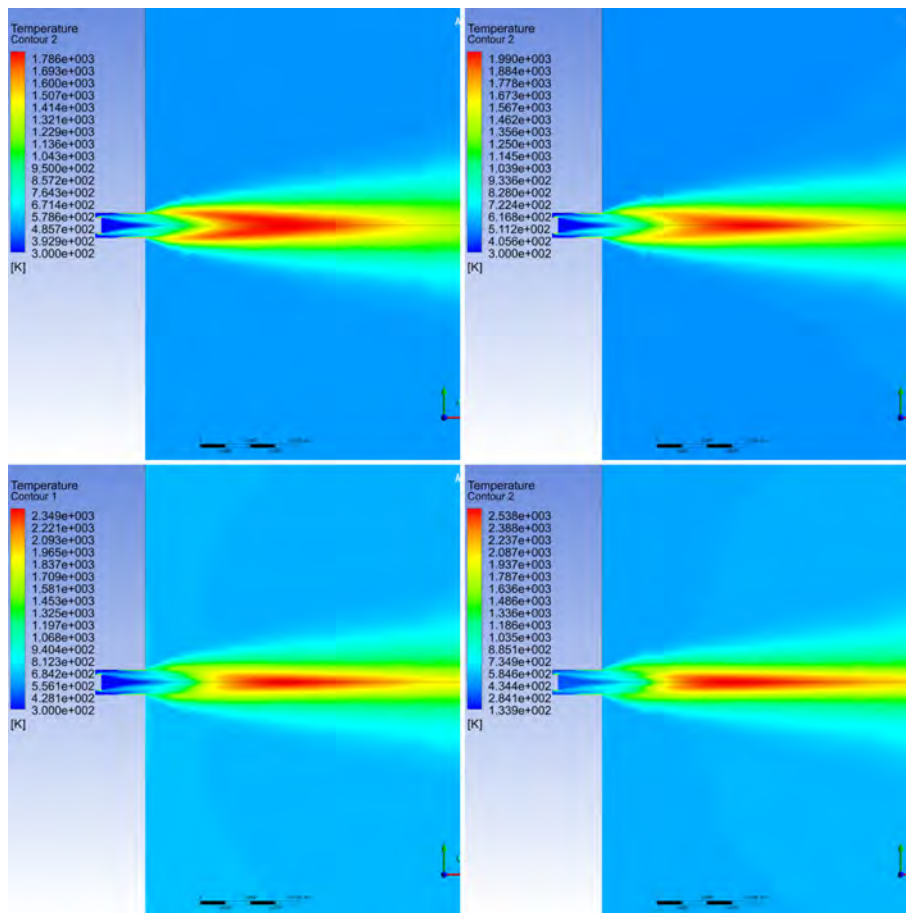
Figure D.1: Unscaled temperature contours for methane and different amounts of iron (TL: $1e^{-4}$, TR: $2e^{-4}$, BL: $8e^{-4}$, BR: $15e^{-4}$
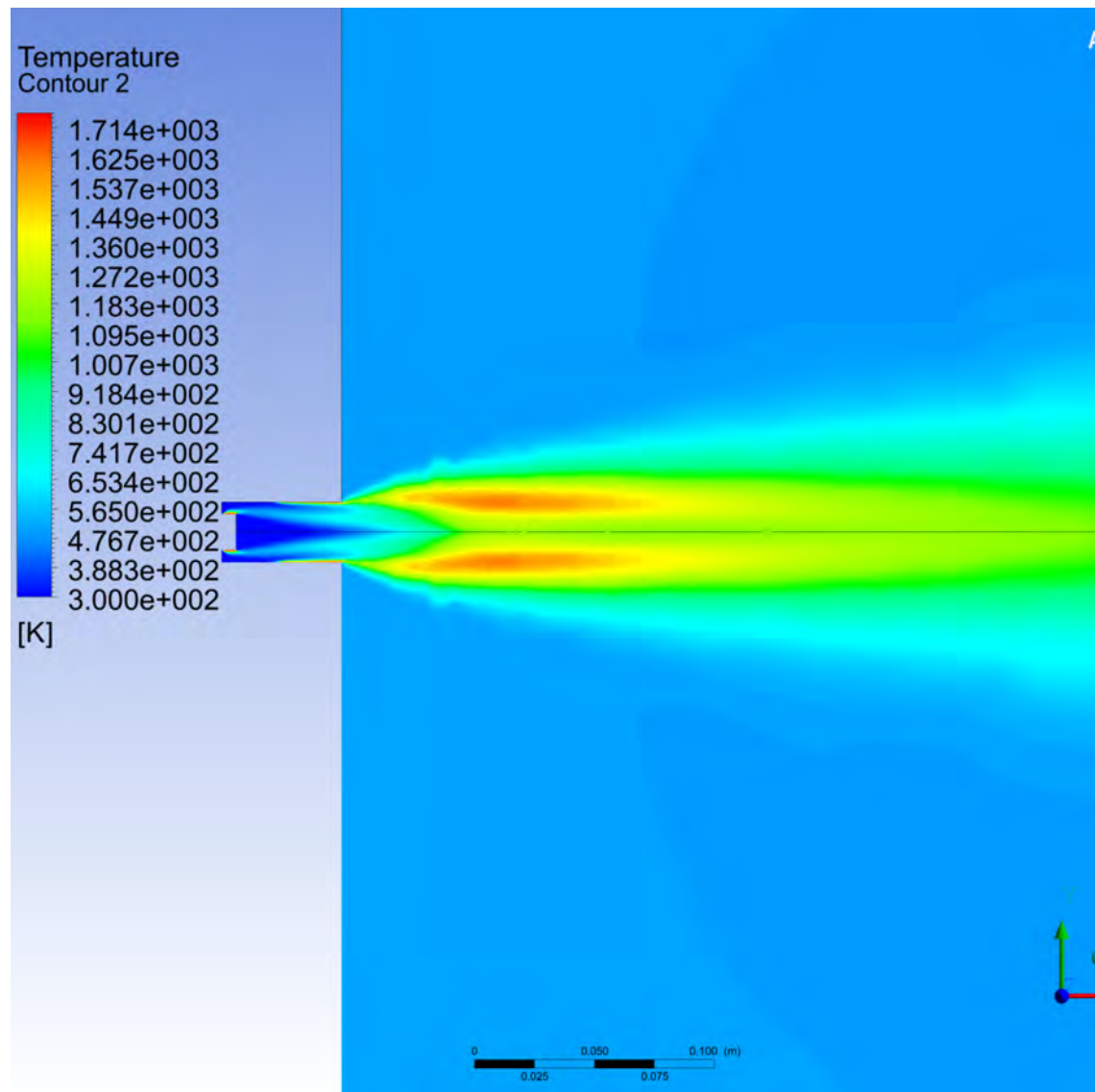
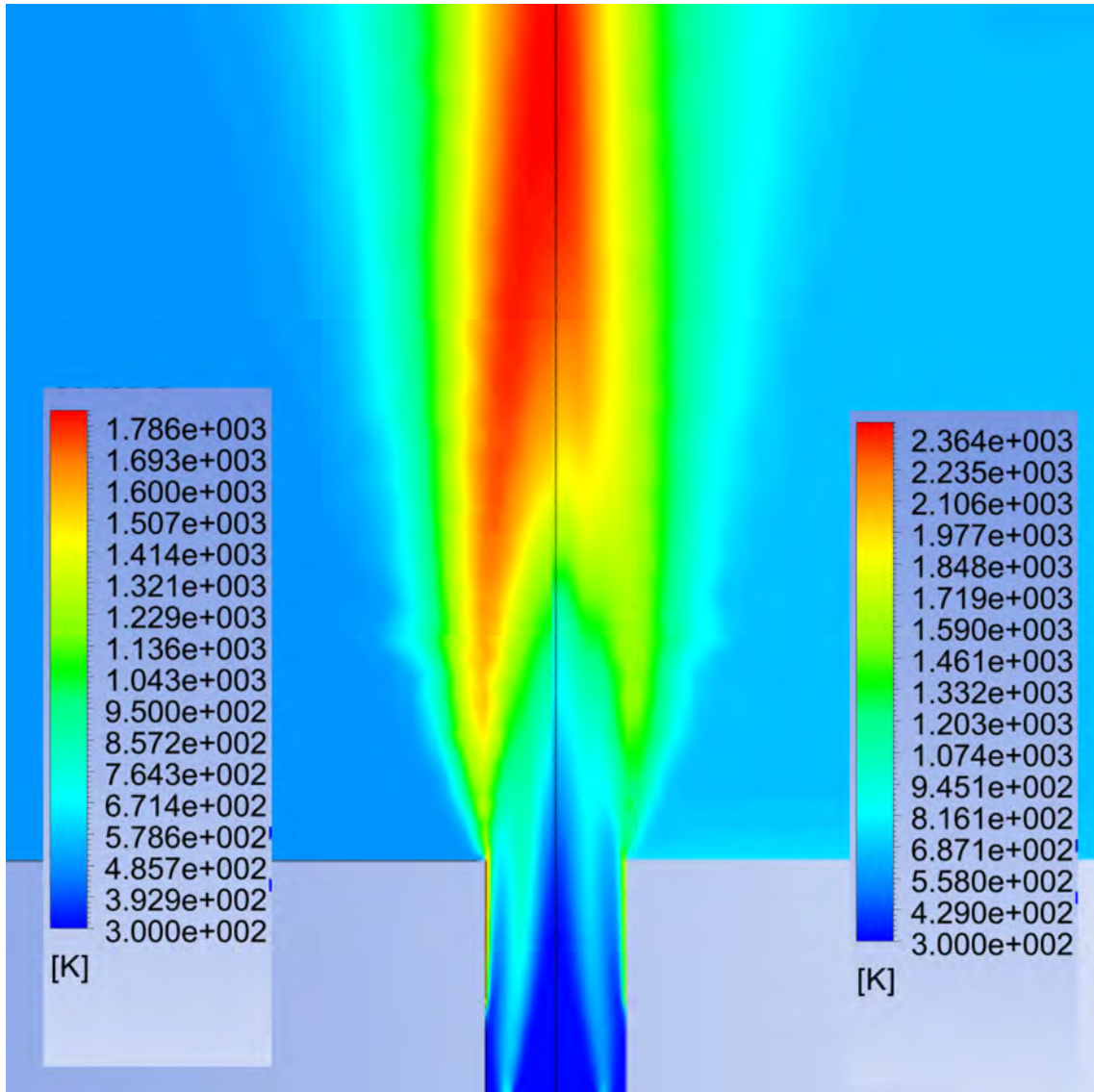Figure D.2: Unscaled temperature contours for methane and 3 $[g/s]$ of iron.

Figure D.3: Unscaled comparison of pure methane and methane and $8e^{-4}$ $[g/s]$ iron.

Appendix E

Low Swirl Burner of Eindhoven University of Technology Design

Figure E.1: Intersection of the computer aided design of the burner.

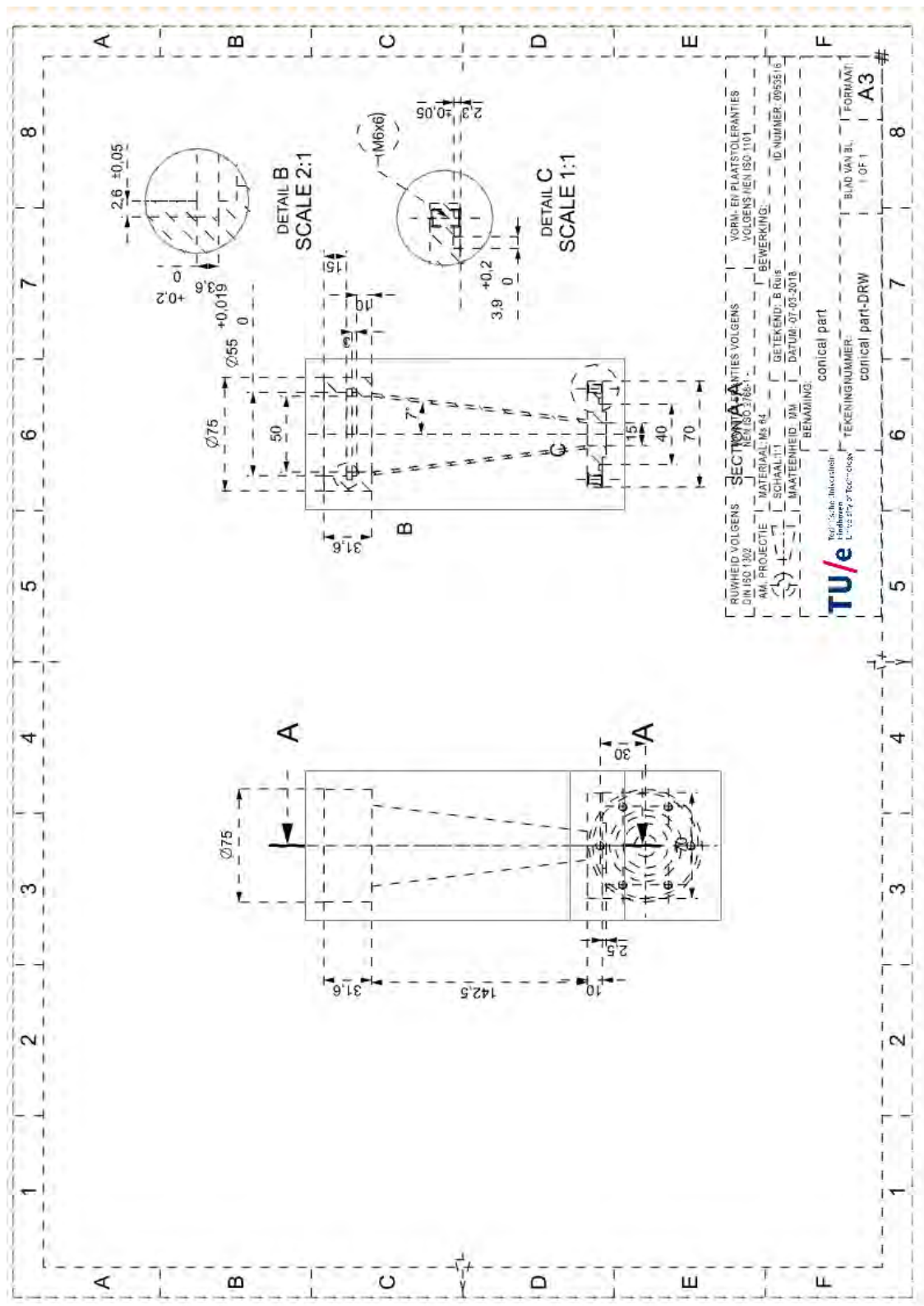Figure E.2: Close up of the swirler inside the burner.

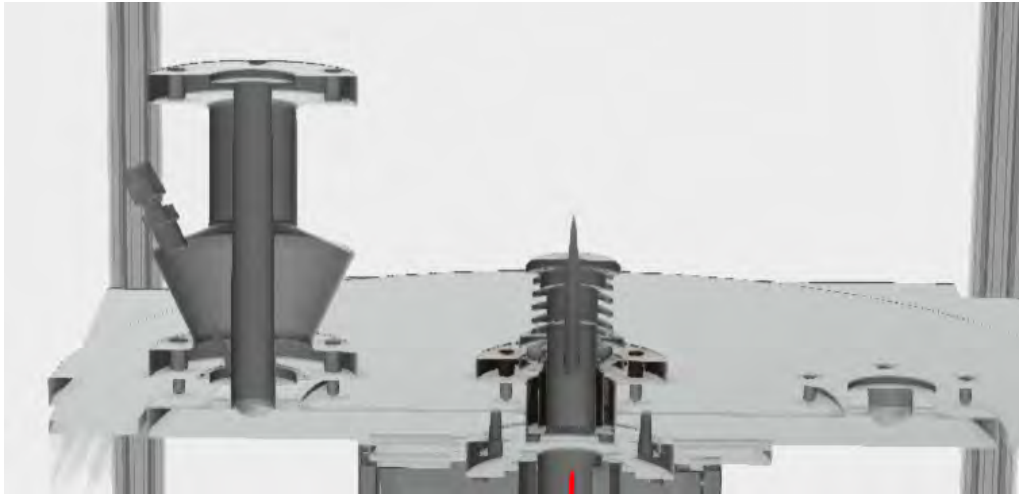Figure E.3: Technical drawing of the upper part of the burner.

Figure E.4: Intersection of the computer aided design of the dispenser.